Photophysical properties of a distyrylbenzene-related color-change fluorophore

by

Hui Wang

A thesis submitted in partial fulfillment of the requirements for the degree of

Doctor of Philosophy

Department of Physics

University of Alberta

Abstract

This thesis mainly focuses on the photophysical properties and potential sensing applications of a designed fluorescent distyrylbenzene-related fluorophore. This fluorophore, which we refer to as "P4VB" in this work shows a large fluorescence spectral shift upon exposure to certain local environments. In this work, the response to protonation is shown to result in a blue-to-orange shift in the visible emitted color. The main research in this thesis then focuses on how one might develop this color-shifting fluorophore for several possible applications, mainly relating to sensing. We start by examining how the fluorescence polarization can be controlled by incorporation of P4VB into a zinc-based metal-organic framework. Next, we show how P4VB can be used for paper-based carbon dioxide sensing, which is based on the formation and detection of carbonic acid in a humid carrier gas. Finally, we show how the sensing capacity can be dramatically enhanced by taking advantage of analyte partitioning into P4VB-loaded oil droplets. All of these methods capitalize on the ratiometric sensing approach afforded by a color-change fluorophore. We finally discuss the limitations of fluorescence color-shift sensing and potential further developments.

Preface

This thesis is an original work by Hui Wang, under the supervision of Dr. Alkiviathes Meldrum at Department of physics, University of Alberta.

Chapter 3 was published as H. Wang et al. "Metal-Organic Framework with Color-Switching and Strongly Polarized Emission." Chem. Mater. 2019, 31, 5816–5823. DOI: 10.1021/acs.chemmater.9b01897. I did the experiments, data analysis, and worked on the manuscript. Dr. Sergei I. Vagin, Dr. Bernhard Rieger, and Mr. Werner Reinhold Heinz synthesized the organic fluorophore and metal-organic frameworks; Dr. Stephen Lane and Mr. Lin Wei, and Ms. Vira Shyta did some preliminary investigations; Dr. Kirsty Gardner operated the Helium Ion Microscope (HIM); Dr. Colin Van Dyck and Dr. Adam John Bergren did Density Functional Theory (DFT) calculations; Dr. Meldrum was the corresponding author and conceived the project.

Chapter 4 was originally published as H. Wang et al. "An Ultrasensitive Fluorescent Paper-based CO_2 Sensor" ACS Appl. Mater. Interfaces 2020, 12, 20507–20513. DOI: 10.1021/acsami. 0c03405. I performed the experiments, data analysis, and worked on the manuscript. Dr. Sergei I. Vagin and Dr. Bernhard Rieger synthesized the organic fluorophores. Dr. Meldrum was the corresponding author and conceived the project.

Chapter 5 was originally published as H. Wang et al. "Ultrasensitive Picomolar Detection of Aqueous Acids in Microscale Fluorescent Droplets" ACS Sens. 2022, 7, 245–252. DOI: 10.1021/acssensors.1c02076. I performed the experiments, data analysis, and drafting of the manuscript. Dr. Zixiang Wei

and Dr. Xuehua Zhang developed a solvent exchange method and experimental setup and taught me how to do it; Dr. Sergei I. Vagin and Dr. Bernhard Rieger synthesized the organic fluorophore; and Dr. Meldrum was the corresponding author and conceived the project.

Acknowledgements

I am very grateful to all people who provide me with support in my research, the thesis, and life.

The Department of physics, Faculty of Graduate Studies and Research (FGSR) of University of Alberta, Alberta Technical University of Munich Graduate School for Hybrid Functional Materials (ATUMS) gave a lot of help in my research.

Thanks to Dr. Sergei I. Vagin, Dr. Bernhard Rieger, Mr. Werner Reinhold Heinz, Mr. Lin Wei, Ms. Vira Shyta, Dr. Colin Van Dyck, Dr. Adam John Bergren, Dr. Zixiang Wei, and Dr. Xuehua Zhang for their great contribution to my research work.

Thanks to Dr. Stephen Lane, Dr. Kirsty Gardner, Dr. William Morrish, Ms. Phurpa Thungon, Mrs. Tanisha Mehreen, Ms. Xiaoyuan Liu, Ms. Razieh Fiouzihaji for accompanying with me. We really have a good time in the lab. I appreciate your companies and friendship.

Thanks to my supervisory committee members, Dr. Alkiviathes Meldrum, Dr. Marek Malac, and Dr. Richard Sydora for the contribution in the selection of courses, guiding in the research, and much useful advice in committee meetings.

My supervisor, Dr. Alkiviathes Meldrum, was the most important people in this thesis and my research work during these five years. I really thank him

for the help in my everything and the patience to guide me in the work. He made me feel that being a PhD student in our lab is the most correct choice in my life so far.

I am also thankful for my boyfriend, Dr. Lingju Meng. He gave me a lot of accompanies and help in my daily life and made me grow up to become a better person.

Contents

List of Tables

List of Figures

Chapter 1

Introduction

1.1 Overview of organic fluorophores

The term "chromophore" is often used to describe a molecular structure that gives color to a material or solution. Many materials are chromophores; for example, chlorophyll is the organic molecule responsible for photosynthesis, which also gives leaves their characteristic green color [1]. In this thesis, we will classify organic fluorophores as carbon-based chromophores that, in addition to potentially being a colorant, are also emissive or fluorescent [2].

Organic fluorophores can emit in any region of the visible spectrum, and they can be classified into several general types. They often contain π-conjugated aromatic rings that develop an energy gap between the bonding and antibonding orbitals. Some fluorescent organic fluorophores even occur in living organisms; for example, green fluorescent protein is found in the jellyfish Aequorea Victoria, which emits green fluorescence under UV excitation [3]. Nicotinamide adenine dinucleotide (NAD) is a coenzyme, which shows a blue fluorescence under a UV light source [4]. Owing to the wide variety of organic fluorophores, we will start by briefly defining some of their major classes in order to place the research work presented in this thesis into a more general context.

Fluorescent organic dyes are synthetic compounds, generally with π conjugated aromatic structures. There is an enormous number of fluorescent organic dyes [5], [6], so, to aid in our task of describing these compounds, we will clas-

sify them into several broad groups (see Fig. 1.1). For example, the well-known family of rhodamine dyes consists of a group of orange-red-fluorescent compounds that are characterised by the presence of a fused, triple-ring aromatic core and a secondary benzene ring linked through a single bond to the central core (Fig. 1.1h) [7], [8]. Various organic groups can be attached to this basic structure, leading to a range of fluorescence typically in the orange or red part of the spectrum and with quantum efficiencies up to 98% [7].

Another example of a common dye family is the pyrenes, which these compounds feature a backbone consisting of four fused benzene rings (Fig. **??**). Pyrenes are colorless in the solid form and typically have a blue or violet fluorescence in solution [7]. Examples include 1-methylpyrene and 3-methylpyrene (Fig. 1.1k) [9], which differ only in the position of one of the methyl groups. The benzopyrenes have one more aromatic ring linked to the pyrene backbone and have a similar blue emission [10]. Other common families of organic dyes, include the azo dyes (yellow or red) [5], cyanine dyes (orange or red) [11], xanthene dyes (red) [12], nitro dyes (green or yellow) [13], quinones dyes (yellow or orange) [14], acridine dyes (green) [15], oxazine dyes (yellow or orange) [16], triarylmethane dyes (green) [17], coumarin dyes (blue or green) [18], and anthracene dyes (blue or green) [19] (Fig. 1.1). Each of these families presents a group of closely related molecular structures with various solubilities and emission characteristics that can be selected for specific applications.

Of direct relevance to this work, we mention another class of organic dyes: the distyrylbenzenes (DSBs). The base structure of the DSB family consists of three benzene rings connected linearly via a single and a double bond (Fig. 1.1m). DSB has a strong blue or teal fluorescence in solution, ranging into the green with the addition of sodium hydroxide [20]. As with the other dye families, changing the molecular sidegroups by the addition of electron donating or withdrawing substituents modifies the absorption and fluorescence. Importantly for this work, replacing the terminal benzene rings with pyridines shifts the wavelength from blue to teal and, as we will see later, can potentially lead

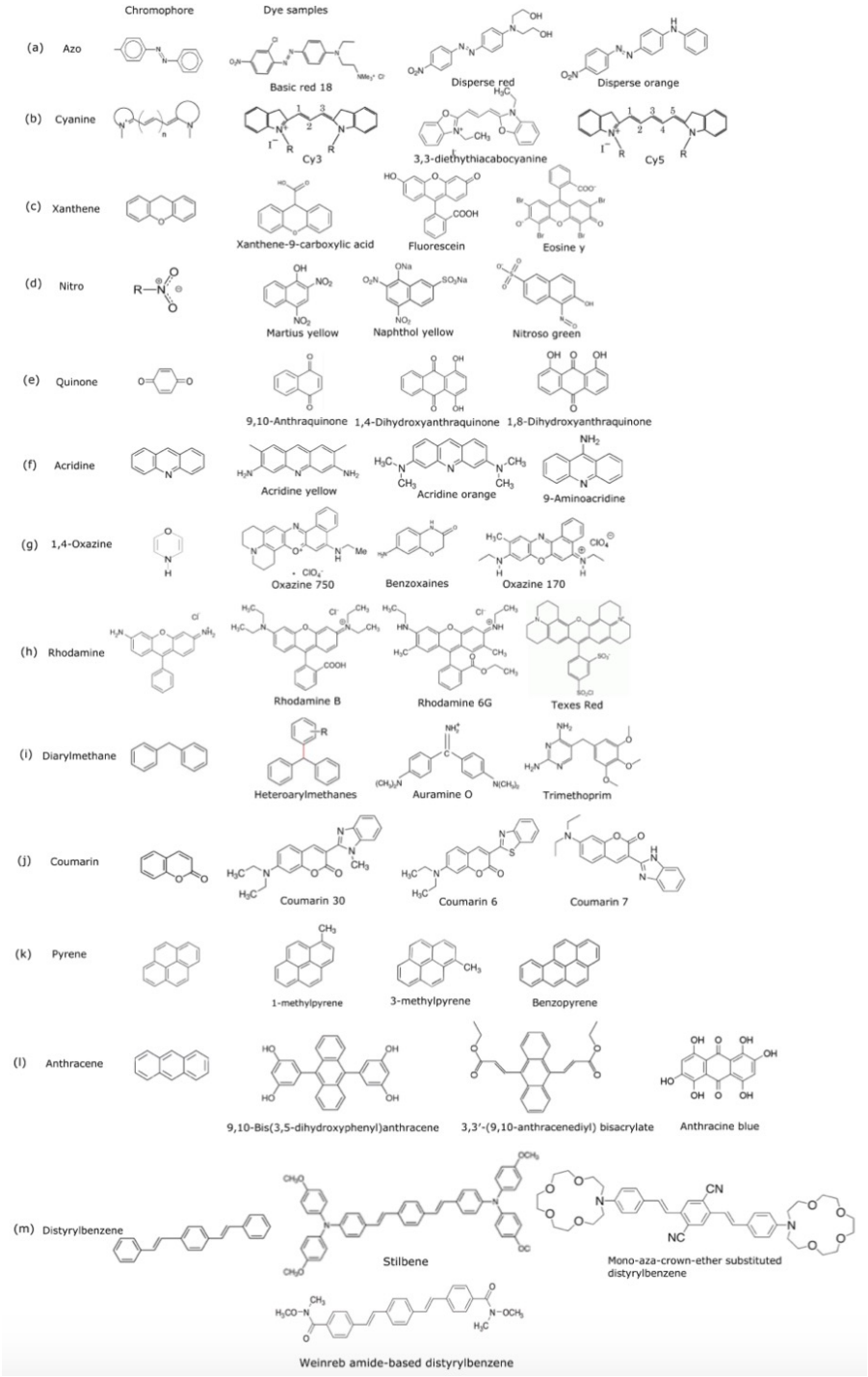

Figure 1.1: Diagrams showing the chemical structures of several families of organic dyes. The basic structure characterizing each family is shown in the first diagram of each line. Several specific examples of dyes belonging to each family are shown.

to several other interesting photophysical effects.

Metal-organic complexes can be considered a sub-class of organic fluorophores, in which a transition metal links several organic ligands [21]. Tris(2-phenylpyridine)iridium(III) ($Ir(ppy)_3$) is an excellent example that is used as a green phosphor in organic light emitting diode (OLED) displays. In $Ir(ppy)_3$, the central iridium ion links three 2-phenylpyridine groups forming a trigonal planar structure. The main functions of metal ion include directing molecular coordination, increasing the molecular rigidity, enhancing the radiative transitions, and improving the charge transport characteristics [22]. Heavy metal ions such as platinum and iridium also increase the rate of the singlet-triplet intersystem crossing, which can result in highly efficient spin-forbidden phosphorescence. The coordinating metal ions contain delocalized electrons which can also improve the charge carrier mobility [22]. Charge transport is important in the performance of the light emitting devices (LEDs) because a high charge mobility can enhance the electron-hole recombination efficiency.

Conjugated organic polymers (CPs) can be viewed as another class of organic light emitters. They are similar to organic dyes except that they form long molecular chains from a basic conjugated repeat unit. This bestows to CPs a blend of fluorophore-like opto-electronic characteristics combined with polymer-like physical properties. An advantage of CPs is that their bulky side groups can prevent or minimize interchain interactions, aggregation, and excimer formation, which can otherwise lead to concentration quenching effects in many organic dyes (see Section 1.4). CPs have tunable molecular structures, which can be adjusted for specific applications such as lasing [23]. Unlike conventional organic fluorophores, CPs remain highly emissive in neat films and can even achieve stimulated emission and lasing in this form [24]. CPs are often based on certain specific repeat units in the chain backbone; common examples include polyacetylene (PA), poly(para-phenylene) (PPP), poly(phenylene-vinylene) (PPV), polyfuran (PF), and polypyrrole (PPy) (Fig. 1.2) [25], [26]. For example, poly[2-methoxy-5-(2'-ethylhexyloxy)-1,4-phenylene vinylene](MEH-

PPV) is a common and widely-studied PPV polymer derivative that features a strong red-orange fluorescence [27].

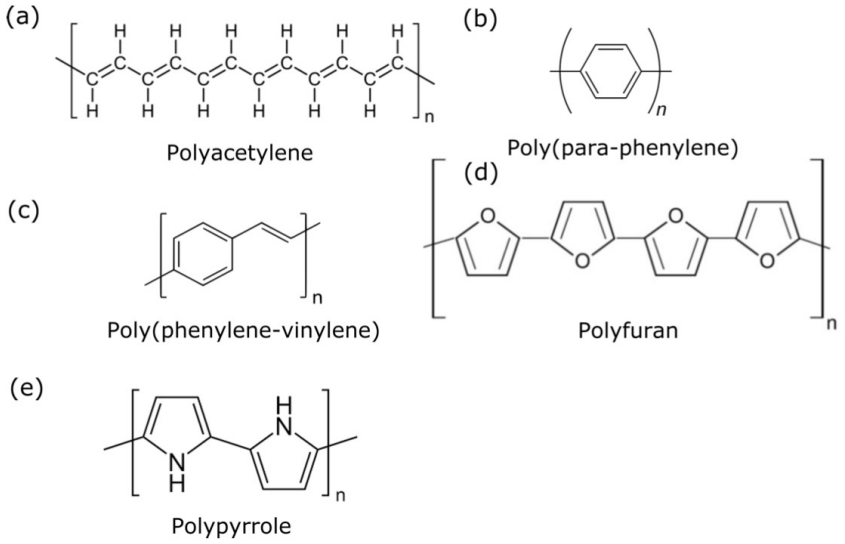

Figure 1.2: Diagrams illustrating example CP structures, specifically (a) polyacetylene (PA), (b) poly(para-phenylene) (PPP), (c) poly(phenylene-vinylene) (PPV), (d) polyfuran (PF), and (e) polypyrrole (PPy).

Organic fluorophores have widespread applications in numerous areas – almost too many to list in detail. These include organic light-emitting diode (OLED) displays [28], lighting [29], biological imaging [30], fluorescence-based sensing [31], biological tagging [32], and lasing [33]. Organic fluorophores are used as active emitting layers in OLEDs and display screens [34]. In biological imaging, quinone-based fluorophores are applied as fluorescent molecular probes in vivo due to their low cytotoxicity and small molecular size, which yields a high cell permeability [34]. Fluorescence-based sensing is another especially common application. Sensing schemes are usually classified according to whether the analyte quenches the fluorescence ("turn-off sensing"), activates it ("turn-on"), or leads to a fluorescence color shift. The latter is attractive because it enables a ratiometric response which can eliminate many problems associated with turn-off or turn-on sensors [35]. Organic fluorophores have been used in highly tunable dye lasers for at least 5 decades [36], and more recently, fluorescent proteins have enabled the development of the first bio-

lasers due to their good biocompatibility, high quantum efficiency and high photostability. Bio-lasers integrate microcavities and dye-infused biological structures including living cells [37].

1.2 Basic optical and electronic properties of organic fluorophores

Before starting on the main research in this thesis, this chapter will give a review of the basic photophysics and the origin of the light emission in organic fluorophores. Organic fluorophores have an electronic energy gap between the π and π^* orbitals which causes the light-emission ability. According to molecular orbital theory, these orbitals arise from the "combination" of the individual atomic orbitals in the associated molecular structure [38]. This orbital blending is described by the linear combination of atomic orbitals (LCAO) theory [39]. The mathematical description of the LCAO is a simple sum given by $\Phi_i = c_{1i}\chi_1 + c_{2i}\chi_2 + c_{3i}\chi_3 + \cdots + c_{1n}\chi_n$, where Φ_i is the molecular orbital obtained by combining n atomic orbitals denoted χ_i [40]. The coefficients, c_{ni}, can be determined by the Hartree-Fock (HF) method used to find the energy and wave functions of N-body systems in a stationary state [41].

Atomic orbitals are combined in covalent bonds so that their wavefunctions overlap [42], [43]. Constructive overlap creates molecular "bonding orbitals", for reasons now explained. In bonding molecular orbitals, the associated electrons are located in the region between two nuclei of the adjacent atoms. For example, in an H_2 molecule, if the hydrogen 1s atomic orbitals with the same wave functions combine to form a bonding "molecular" orbital, then the electrons are located between two nuclei and attract them toward each other, thus making the molecule more stable [42]. This is an exothermic process. The atomic orbitals can also combine via destructive interference, forming the antibonding molecular orbitals [42]. As opposed to the bonding molecular orbitals, the electrons in antibonding orbitals will be found outside the space

between two nuclei. The electrons thus pull the positive nuclei away from one other, so this type of molecular orbital makes the bond between the two nuclei less stable [42].

Hybridization is the process of mixing atomic orbitals when covalent bonds are formed [44]. The sp orbital hybridizations are the mixture of s orbitals and p orbitals, denoted by sp, sp^2, or sp^3 hybridization. For example, in carbon atoms, the 2s orbital and all three 2p orbitals (p_x, p_y, and p_z) hybridize to form four equivalent sp^3 hybridized orbitals pointing toward the corners of a tetrahedron (see Fig. 1.3 for methane). Each hydrogen 1s orbital overlaps with one of the four carbon sp^3 orbitals to from one single sigma bond [45]. Sigma bonds are symmetrical upon a rotation around the bond axis and are on a line joining the two nuclei (Fig. 1.3).

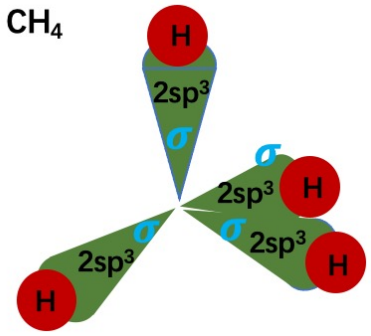

Figure 1.3: A diagram illustrating the CH_4 molecular orbitals. The four hydrogen s orbitals can overlap the carbon sp^3 orbitals to form four sigma bonds. The angle between each hybridized sp^3 orbital is 109.5° [45], [46].

Similarly, sp^2 hybridization presents a mixture of a 2s orbital and only two of the three 2p orbitals in carbon [47], [48]. Here, C_2H_4 is a good example. Each hydrogen 1s orbital overlaps with the two of the three carbon sp^2 orbitals to form sigma bonds (Fig. 1.4). The third sp^2 orbital overlaps with the sp^2 orbital from another carbon atom to form a C–C sigma bond. Compared with sp^3 hybridization, sp^2 hybridization has only three hybridized orbitals, leaving an unhybridized p orbital. The unhybridized p orbitals from two carbon atoms

can then overlap to form a π bond [48]. The resulting σ and π bonds between two carbon atoms form a double bond (Fig. 1.4). The π bond thus consists of two p orbitals perpendicular to the axis of the sigma bonds (Fig. 1.4).

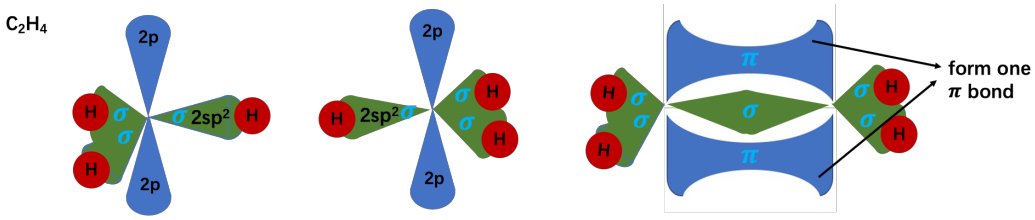

Figure 1.4: A diagram for the C_2H_4 molecular orbital. The angle between each sp^2 orbital is 120° and all three sp^2 orbitals are in the same plane. The double bond consists of the π and σ orbitals. The blue color represents p orbitals; green color represents sigma bonds; red color represents hydrogen s orbitals.

Finally, sp orbital hybridization results in triple bond formation [48]. For example, C_2H_2 has two carbon atoms and two hydrogen atoms. Each hydrogen can overlap with one of the carbon sp hybridized orbitals to form a C-H sigma bond (Fig. 1.5), while the remaining sp orbital can overlap with the sp orbital from another carbon to form a C–C sigma bond. The two remaining unhybridized p orbitals overlap with the p orbitals from another carbon to form two π bonds [49]. The two π bonds and one sigma bond complete a triple bond (Fig. 1.5).

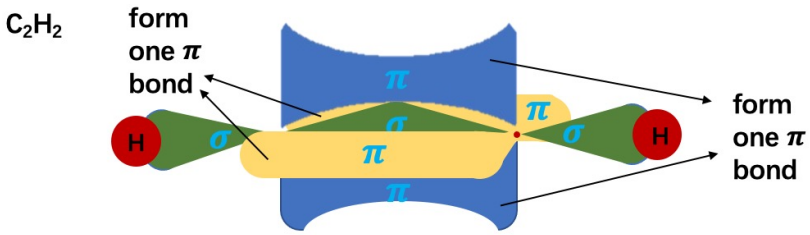

Figure 1.5: A simple sketch illustrating the C_2H_2 molecular orbitals. The triple bond consists of one σ and two π bonds [49]. Blue represents π orbitals in the y direction; yellow represents p orbitals in the x direction; green represents sigma bonds; red represents hydrogen s orbitals.

Staying with the previous example of molecular hydrogen, there are only

two electrons in the molecule. So, these two electrons can fill one bonding molecular orbital according to the Pauli principle [50]. The total number of molecular orbitals is the same as the number of atomic orbitals used to form them, so, for other more complex molecules, there can be multiple molecular orbitals. The electrons fill the lowest bonding molecular orbital first (Hund's rules are used to predict the how the orbitals are ordered in terms of their energy) [51]. Once all the electrons have filled the lowest-energy molecular orbitals in order, the energy gap between the highest occupied molecular orbital (HOMO) and the lowest unoccupied molecular orbital (LUMO) represents the lowest-energy optical transition. The energies associated with these levels is important for fluorescence and energy or charge transfer between different compounds [52].

There are several methods that can be used to measure or calculate the HOMO and LUMO energies, such as ultraviolet photoelectron spectroscopy (UPS) [53], inverse photoelectron spectroscopy (IPES) [54], absorption measurements [55], cyclic voltammetry (CV) [56], and density functional theory (DFT) calculations [57]. While only DFT was performed in this research, it is nevertheless important to recognize the methods available.

UPS measures the kinetic energy of the photoelectrons emitted from occupied electronic states upon excitation by ultraviolet radiation (Fig. 1.6a) [58]. The sum of the electron kinetic energy and the potential energy of the highest occupied electronic state (E_{HOMO}) is equal to the incident photon energy (hv_1), given by E_k=hv_1-E_{HOMO} [59]. In a related method, inverse photoelectron spectroscopy (IPES) uses an electron beam to measure the energies of the lowest unoccupied electronic state in solid analyte films. The measured photon energy (hv_2) is the sum of the kinetic energy (E_i) of the incident beam electrons and the binding energy associated with the LUMO (i.e., Fig. 1.6b) [60]. CV is a three-electrode electrochemical technique for measuring the current response of an oxidation-active solution to a linearly cycled potential sweep between two or more voltages [61]. While the CV experiment and analysis can

be complicated, the basic idea is that a measurement of the redox potentials of the analyte can yield the HOMO and LUMO energies with respect to a reference material (e.g., ferrocene) [61].

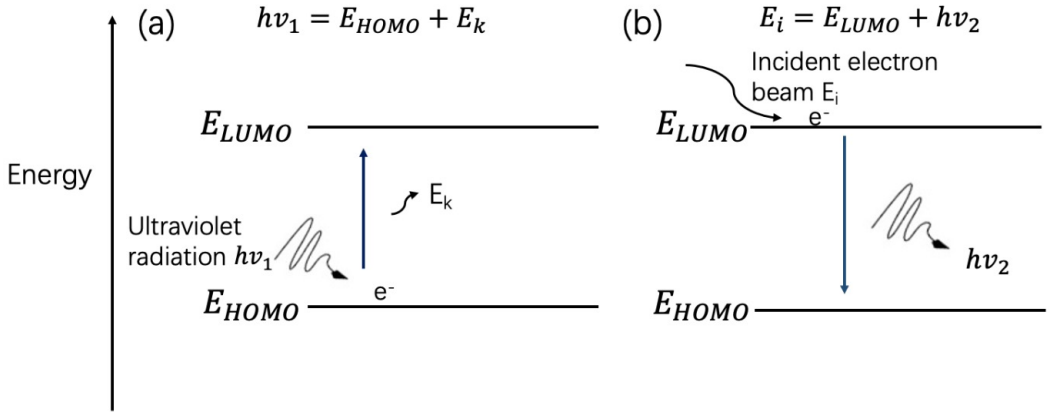

Figure 1.6: A diagram illustrating the energy relationship for UPS (a) and IPES (b) measurements, as described in the text.

The LUMO and HOMO energies also can also be calculated using density functional theory (DFT). DFT is a computational quantum modelling method used to study the electronic structures of many-body systems, such as atoms, molecules, and condensed matter phases [57]. In DFT, the electronic properties of the many-body systems can be calculated via the so-called "functionals" associated with the electron density, such as the electron-electron interaction energies [62]. DFT can provide a good way to obtain the HOMO and LUMO energies in organic fluorophores without requiring complex experimentation, and the method has been so well refined since the 1990s that it is now considered as generally reliable [63]. However, significant computational power may be necessary to achieve reasonably accurate modeling, and several assumptions built into the model may need to be carefully evaluated [64].

As previously stated, electrons fill the energy levels that are ordered according to Hund's rules. This leads to the concept of singlets, doublets, and triplets [65]. These states are named according to their multiplicity, which is defined by the number of independent spin sublevels and is given by 2S+1,

where S is the total spin [66]. Essentially, the multiplicity represents the number of ways that the electron spins can be aligned. The term "singlet" implies a single sub-level from the set of particles with a net spin quantum number of zero (electrons are paired) [67]. An example is shown in Fig. 1.7 (left side) where there are two electrons filling an energy level representing a ground state singlet S_0. Because the spins are in the opposite sense, the multiplicity is $2 \times (1/2 - 1/2) + 1 = 1$, meaning that the singlet state has only one possible orientation of the spin angular momentum [67]. The doublet state has one unpaired electron (Fig. 1.7, center) so its multiplicity is $2\times(1/2)+1=2$. The doublet can thus have two possible spin sublevels, one associated with spin up and the other with spin down [67]. Finally, the triplet state has two unpaired electrons with the same spin orientation so the net angular quantum number is 1 (Fig. 1.7, right side) and the multiplicity is $2\times(1/2+1/2)+1=3$ [67]. The triplet state thus has three possible sublevels or spectral lines (Fig. 1.8). Moreover, the triplet state has a lower energy compared to the unpaired singlet state (S_1), because the spin-related exchange interaction requires the triplet electrons (with the same spin) to remain spatially well separated. Importantly, in molecular oxygen (O_2) the triplet with its two unpaired electrons is the ground state of the molecule; whereas in the vast majority of molecules the paired singlet state S_0 has the lowest energy.

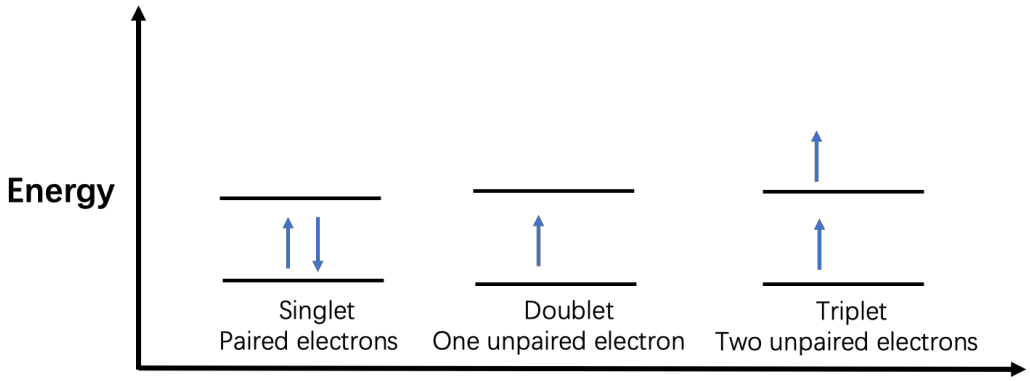

Figure 1.7: A diagram illustrating a singlet (showing the ground state), doublet (ground state), and triplet (excited state).

The singlet, doublet, and triplet states can perhaps most easily be visualized using a "cone diagram" (Fig. 1.8). The electrons spin vector is illustrated by the arrows. Assuming we know the spin in the z-direction, then the uncertainty principle prevents us from knowing the spin component in the xy plane. Thus, the spin vector can exist anywhere on the surface of a cone centered on the z axis. In the singlet state, the total spin is zero, so the two electron spin vectors must always point in opposite directions in their respective cones. For the triplet state, however, the total spin is 1 and there are actually three ways to make this work out. The spins can either point along opposite sides if the same cone, leading to a spin of 1 in the +z (T_1) or –z (T_2) directions. On the other hand, the so-called T_0 state has the two spins pointing in the same xy direction but in opposite z directions. The addition of these two spin vectors will lead to a net spin vector of 1, but it is purely within the xy plane.

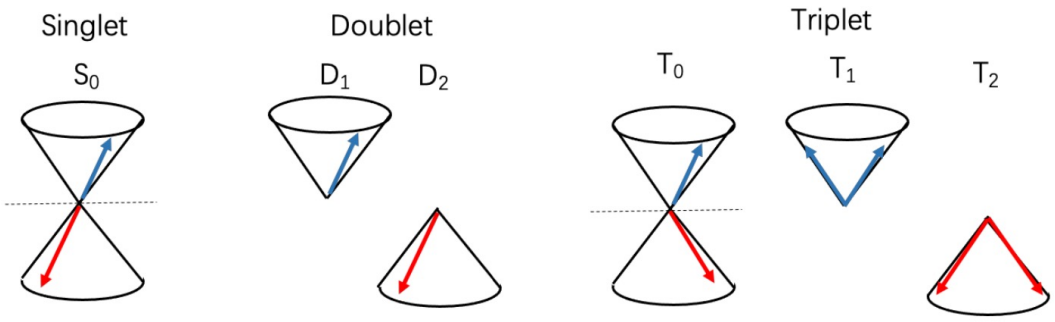

Figure 1.8: A diagram demonstrating the possible orientations of singlet, doublet, and triplet states. With the spin vector known in the vertical z-direction, it becomes completely unknown in the x-y plane (thus the total spin vector can point anywhere on the surface of the cone). In the single state, the spin vectors point in opposite directions. In the triplet state, there are three ways to obtain a total spin S = 1. The electrons can have a total spin vector of one unit along ±z, or, as shown in the T_0 case, the two spins are coplanar leading to a total spin vector of one unit in the xy plane. The doublet state is trivial since there is only one unpaired electron which can be oriented along the +z or –z cone; hence two possible spin states.

Before we discuss the fluorescent properties, we briefly recall the Jablonski diagram – a commonly used method to visualize the molecular energy levels [68]. This diagram is named after the late Polish physicist Aleksander

Jablonski (died Sept. 1980), a famous molecular spectroscopist who developed many of the key ideas in the field. In the Jablonski diagram, the spin energy levels and vibrational energies are illustrated as horizontal lines on a vertical energy scale (Fig. 1.9), allowing various transitions to be illustrated visually with arrows. Several singlet and triplet states and their associated vibrational overtones are illustrated in the figure for a prototypical fluorophore. As an aside, the narrowing energy spacing as one goes up the vibrational "ladder" is a result of anharmonicity. Essentially, the confining potential becomes non-parabolic, causing the vibrational overtones to space more closely with increasing energy [68].

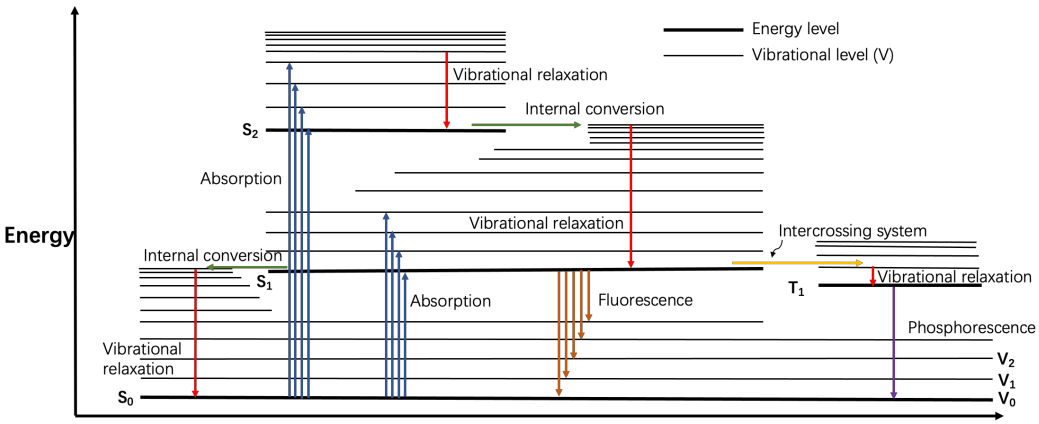

Figure 1.9: A representative Jablonski diagram showing the singlet ground state (S_0), single excited state (S_1), triplet state (T_1), vibrational states (V_0, V_1, and V_2), the absorption process (blue arrows), fluorescence (orange arrows), vibrational relaxation (red arrows), internal conversion (green arrows), intercrossing system (yellow arrows), and phosphorescence (purple arrows).

The Jablonski diagram can help visualize certain common electronic transitions and naming conventions. For example, the ground singlet state is referred to as S_0, as usual. The electrons can be optically excited to vibrational energy levels in the excited singlet states S_1 or S_2. These electrons may decay non-radiatively to lower vibrational energy levels before reverting back to the S_0 state with the emission of a photon. The latter process occurs on the nanosecond timescale and is referred to as fluorescence. The vibrational decay occurs mainly though non-radiative picosecond-timescale vibrational re-

laxation, in which the energy is, for example, transferred to the vibrational or kinetic motion of the nearby solvent molecules. The vibrational levels shown in Fig. 1.9 thus lead to a long-wavelength shift of the PL relative to the absorption maximum. As discussed previously, this is referred to as the Stokes shift, named after the Irish physicist George Gabriel Stokes [69]. Curiously, both Stokes and Jablonski, names so commonly used in chemistry, were actually physicists.

Some electrons also can "cross over" from the singlet state (S_1) to the excited triplet state (T_1) via a spin flip when a change in orbital occupancy (i.e, P_x to P_y) occurs to conserve net angular momentum (as illustrated graphically in Fig. 1.10) [70], [71]. The change in the orbital occupancy is represented as a change in the magnetic quantum number (m_l) and is associated with spin-orbit coupling. This process is more favorable when the vibrational levels of the two states overlap or are close in energy. The rate of spin-orbit coupling turns out to be proportional to the fourth power of the nuclear charge [72], [73]. This is the reason why the spin-orbit coupling interaction (and, thus, the singlet-to-triplet intersystem crossing) is much more significant in fluorophores that contain heavy atoms. Eventually the excited state T_1 can decay to the ground state S_0 via another spin flip, which again requires spin-orbit coupling to conserve angular momentum (Fig. 1.10). This latter requirement makes the process "electronically slow" (up to milliseconds or even longer) and it is referred to as phosphorescence [74]. As another aside, the term phosphorescence does not come from the chemical element phosphorus – rather, it owes its etymology to the Greek words $\phi\omega\sigma$ (light) and $\phi o\rho\varepsilon\iota\sigma$ (to bear) – that is, "light bearing". In contrast, the term "fluorescence" was coined by George Stokes, the above-mentioned Irish physicist, referring to the light-emissive properties of certain impurities in the mineral fluorite (CaF_2) [75].

We finally give a brief description of the selection rules associated with these various electronic transitions. These rules describe whether an transition is quantum mechanically "allowed" [76]. Different energy states are

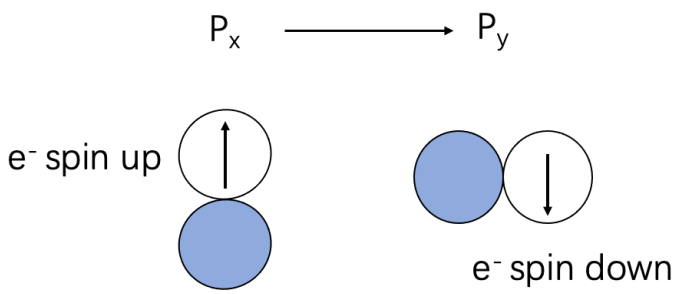

Figure 1.10: A rough illustration of the P_x-P_y transition and the corresponding electron spin flip. The white and blue circle represent individual p orbitals. The momentum (m_l) of P_x is -1, and the spin momentum of the "up" electron is 1/2 so the total angular momentum is -1/2. When the electron spin flips from "up" to "down" there is a corresponding orbital change from P_x (-1) to P_y (0), which thus changes the orbital angular momentum exactly to conserve the total angular momentum of the system.

associated with the orbital angular momentum (l) and spin quantum number (s). The angular momentum (l) describes the rotation of the system along a given axis and the spin quantum number describes the spin angular momentum of an electron, as before [77]. The selection rules for the allowed transitions are:

- $\Delta l = 0, \pm 1$. This rule states that the electrons can only jump between energy levels differing by one angular quantum number ($\Delta l = \pm 1$) or transit non-radiatively within the vibrational levels of the same energy state ($\Delta l = 0$) [76]. The selecton rules are based on the conservation of the angular momentum. A photon has one unit of quantized anguler momentum, so after absorbing or emitting a photon the angular quantum number must correspondingly change by 1 ($\Delta l = \pm 1$) [78]. If $\Delta l = 0$, then angular momentum is conserved in the absence of an optical transition.

- $\Delta S = 0$. This shows that the electrons only can transit between energy states with the same spin. Only in the case of spin-orbit coupling does this rule become "slightly relaxed", since it provides a mechanism to otherwise conserve the total angular momentum.

1.3 Radiationless processes

This sub-section examines in brief a few of the processes that lead to radiationless decay or energy loss from the fluorophore of interest. Some of these are entirely unwanted from a light-emission point of view, while others can actually be desirable (e.g., the transfer of energy from one fluorophore to another one). Several of these processes can also be used for fluorescence-based sensing applications.

1.3.1 Internal conversion

Internal conversion is the non-radiative transition between the vibrational states with the same spin multiplicity (Fig. 1.8). During this process, the excited-state fluorophore molecules transit between vibrational levels, releasing the energy as heat.

1.3.2 Vibrational decay

Vibrational decay is typically thought of as distinct from internal conversion insofar as it often implies the transfer of energy to the vibrational states of another particle (i.e., a solvent molecule). The efficiency of vibrational decay mainly depends on the molecular configurations. For example, molecules with non-rigid molecular configurations, such as biphenyl, can have a high degree of vibrational freedom, which leads to a strong interaction with surrounding solvent molecules and a high vibrational decay rate [79], [80]. In contrast to biphenyl, molecules with rigid chemical structures, such as fluorene, can have a low frequency vibrations and low decay rate [81] (Fig. 1.11) .

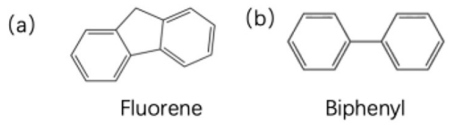

Figure 1.11: The chemical structures of (a) fluorene and (b) biphenyl.

1.3.3 Intersystem crossing

As discussed previously, this process represents spin transitions between electronic energy states with different multiplicity - for example, from single state (S_1) to triplet state (T_1) (Fig. 1.7). This process removes $S_1 \rightarrow S_0$ fluorescence and the single-to-triplet conversion results in either phosphorescence or non-radiative triplet decay via vibrational transfer from T_1 to the surrounding molecules.

1.3.4 Intermolecular interactions (quenching)

These processes represent interactions between excited fluorophore molecules and another type of molecule in the immediate vicinity. The excited fluorophore can either transfer its entire excitation energy to the second molecule (for example, in F*ö*rster resonance energy transfer). Alternatively, charge can be transferred to electron-accepting or electron-donating molecules. These processes are referred to as "quenching" of the fluorophore, because they represent impermanent or reversible electronic transitions. Since these quenching processes are important in many situations, they are briefly described in more detail below.

F*ö*rster (or "fluorescence") resonance energy transfer (FRET)

FRET is a radiationless energy transfer between a fluorescent donor (D) and an acceptor (A) molecule (Fig. 1.12). This evanescent-like process depends on the degree of spectral overlap between the donor emission and acceptor absorption and the distance between the donor and acceptor molecules (the FRET rate depends on $(R_0/R)^6$ where R_0 is on the scale of 1-10 nm and R is the donor-acceptor distance [82], [83]). The alignment or angle between the dipole moments of the donor and acceptor is also important but is typically averaged over all possible angles. The full FRET formula is derived in Ref. [84]. FRET is a huge topic and is widely used in many applications; for the purpose of this thesis, we simply include it as one of the key non-radiative

processes for a donor fluorophore (although the acceptor itself may also be fluorescent [85]).

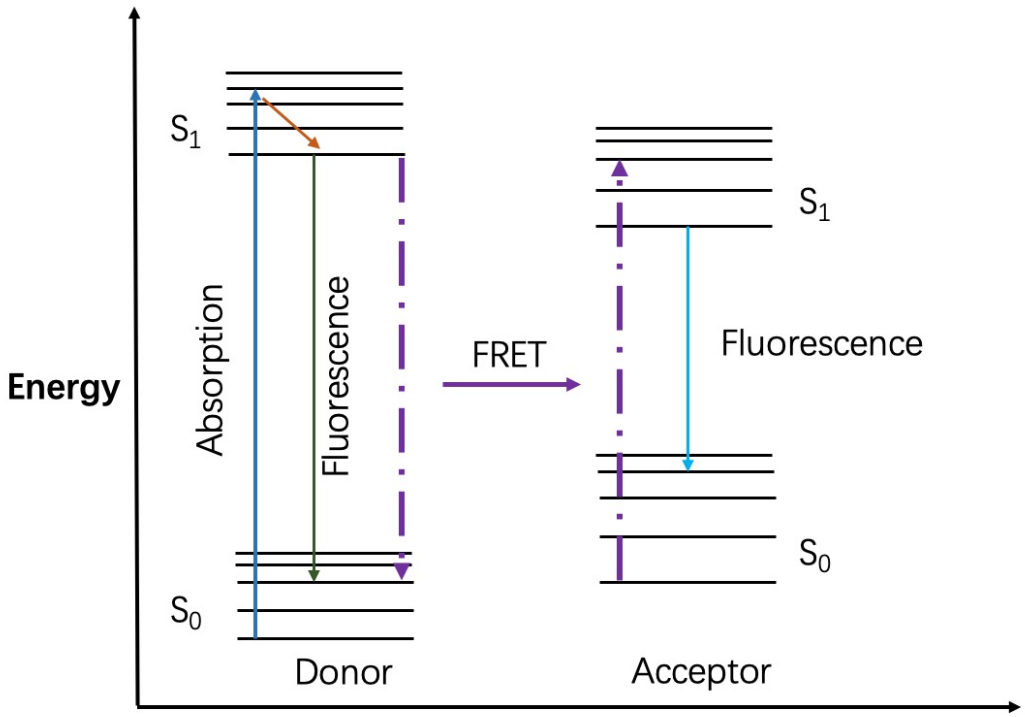

Figure 1.12: A basic diagram illustrating the FRET process [86]. The incident light excites the donor fluorophore molecule to the excited state (dark blue arrows). The energy from the excited donor molecule can be transferred to the acceptor molecule non-radiatively (purple dashed arrows), which can itself be fluorescent (light blue arrow).

Dexter electron transfer

Dexter electron transfer is another fluorescence quenching mechanism, first proposed by D. L. Dexter in 1953 [87]. Dexter transfer is a quantum effect that relies on wavefunction overlap between the donor and acceptor states. In this case, an electron in an excited state of a donor molecule can transfer to an acceptor molecule, causing fluorescence quenching of the donor. An electron on the ground state of the acceptor can also transfer to the donor to accomplish non-radiative electron exchange (Fig. 1.13). In contrast to FRET, the Dexter process implies charge transfer and, due to the requirement for overlapping wavefunctions, the characteristic distance is only about 1 nm [87]. The Dexter

rate is proportional to the inverse square of the distance (as opposed to the inverse sixth power for FRET) and depends on the square of the transition dipole moments of the donor and acceptor molecules [88].

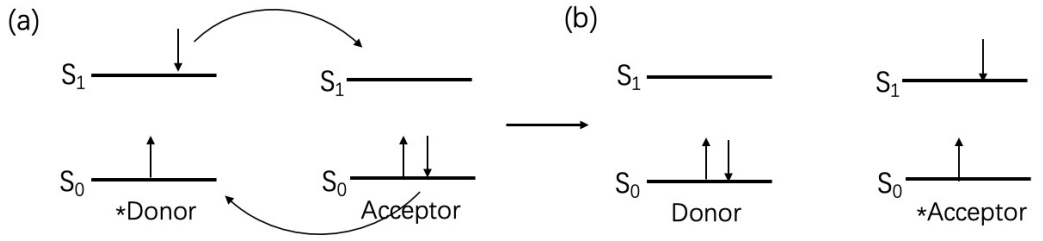

Figure 1.13: A scheme of Dexter charge transfer process. (a) An electron on the excited state of a donor molecule (*donor) can transfer to an acceptor molecule. An electron on the ground state of the acceptor molecule can also transfer to the donor molecule to achieve electron exchange. (b) Final state after the two electron exchanges.

1.3.5 Photobleaching reactions

Photobleaching represents an irreversible decrease in the quantum yield (QY) (or intensity) of the PL as a result of photochemical processes involving the absorption of incident radiation. The term actually originates from the color-fading that occurs when sodium hypochlorate (commercial "bleach") reacts with fibers in clothing fabrics, fading the color staining [89]. In fluorescence studies, bleaching refers to an irreversible decrease in the PL intensity as a sample is exposed to the excitation light source. The photobleaching mechanisms can be separated into an oxygen-dependent pathway and an oxygen-independent pathway.

Oxygen-related photobleaching

In fluorophores with a high rate of intersystem crossing, the excited triplet state can react with the O_2 triplet ground state by energy or charge transfer, resulting in the decay of the fluorophore to the ground state and the production of singlet oxygen [90]. Singlet oxygen can be highly reactive to organic molecules, leading to oxidation and the breaking of existing covalent bonds. For example, singlet oxygen readily oxidizes phenols and sulfides of organic

fluorophores to form hydroperoxides and sulfoxides [91]. This means that oxygen can be an important photobleaching agent for many fluorophores and care may need to be taken to avoid combined exposure to oxygen and light.

Oxygen-independent bleaching

The second mechanism involves the formation of radicals which cause the photodegradation or bond breaking in the fluorophore. In other words, an incident photon may directly sever a chemical bond. This process depends on the energy of the incident photons and the bond energies of the fluorophore. For example, azobenzene is a kind of yellow fluorescent fluorophore. Ultraviolet light can break an azo bond, separating the original molecule into two phenyl rings (Fig. 1.14) [92].

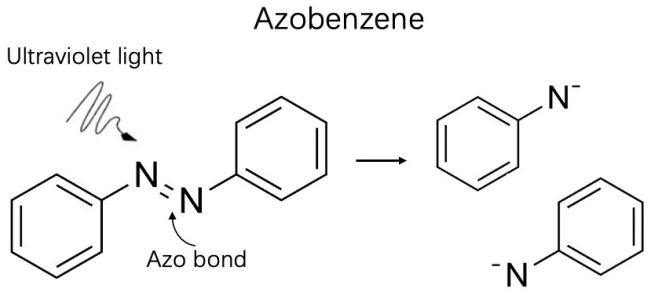

Figure 1.14: A scheme of photobleaching process of azobenzene. The azo bond can be broken by ultraviolet light, and then the azobenzene is separated into two phenyl rings.

1.4 Color change fluorophores

Color-change fluorophores are fluorescent materials whose emission spectrum is modified as a result of changes in the surrounding environment [33]. One such color-change fluorescent compound will be the main subject of this thesis. Conjugated organic fluorophores can be especially sensitive to fluorescence spectral shifts because of their delocalized electrons [33]. The ability of a fluorescent material to change its fluorescence spectrum in response to external stimuli suggests many possible applications. For example, one group recently reported a novel color-change green-emitting fluorophore that turns orange

when scratched – in fact, fluorescent orange wording could be written on a green background [93]. While quenching phenomena have been used probably thousands of times for sensing demonstrations in the literature (i.e., the analyte is the quencher), color-change fluorophores may enable a more robust ratiometric approach to sensing [94].

A common mechanism by which a fluorophore may change its emission spectrum is known as solvatochromism [95]. Solvatochromism is the solvent-induced modification in the electronic energy levels of the fluorophore [95]. Effectively, the electron clouds associated with the HOMO-LUMO gap are influenced by the dielectric constant or polarizability of the surrounding solvent [96]. This solvatochromic shift is typically on the order of tens of nanometers in the fluorescence spectrum. A good example of a solvatochromic fluorophore is Nile Red (Fig. 1.15), which shows a redshift by 25 nm upon changing the solution from pyridine to ethylene glycol [97]. "Positive" solvatochromism refers to a fluorescence redshift when dissolved in higher-polarizability solvents; whereas negative solvatochromism represents, naturally, a spectral blueshift. An example of the negative solvatochromism is "Brooker's merocyanine", which changes from yellow fluorescence when dissolved in methanol to blue-violet in acetone [98].

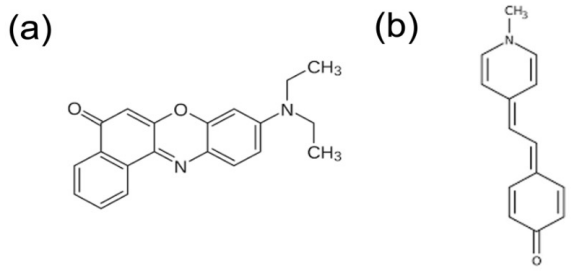

Figure 1.15: Chemical structure of (a) Nile Red and (b) Brooker's merocyanine.

Less commonly, some fluorophores can exhibit a large spectral shift upon physical interactions with certain specific materials. A good example is polyviny

-l diphenylquinoline which shows a fluorescence spectral shift from 486 nm to 529 nm upon exposure to acidic compounds [99]. Here, the H^+ ions interact with the electron clouds associated with the HOMO and LUMO of the fluorophore via the hydrogen bonding between the H^+ ions and the electronegative parts of the fluorophore. This process is referred to as protonation. Unlike solvatochromism, this interaction involves electrostatic or hydrogen bonding, and the effect can be quite strong because the external ions (e.g., H^+) can come in especially close proximity and can even become physically bound to the conjugated backbone of the fluorophore.

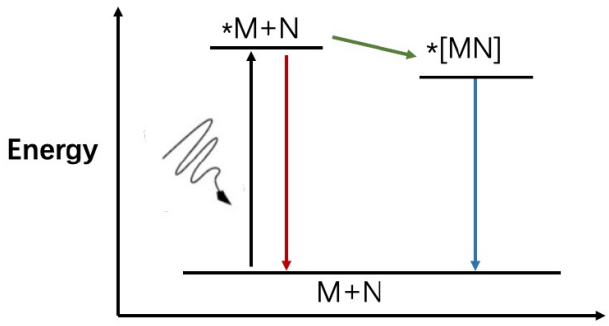

Figure 1.16: A diagram for the energy transfer between the excited monomer *M and formed exciplex complex *[MN]. The ground-state monomer (M) can be excited into the excited state (*M). *M can then form the excited exciplex *[MN] with the surrounding molecule N via a physical bond. The difference in energy levels between ground-state monomer and exciplex complex cause the emission color shift98.

Another fluorescence color change mechanism results from the formation of an exciplex state. When an excited fluorophore (*M) interacts with a ground-state surrounding molecule (N), they can form a physically (electrostatic) bonded complex referred to as an exciplex [100]. Alternatively, the excited fluorophore (*M) also can interact with the ground-state of the same fluorophore (M) to form an excimer [101]. The excited-state complex *[MN] or *[MM] results in the development of a new energy state (Fig. 1.16). This state has lower energy than that of excited-state fluorophore, with the difference in energy being released when the bond between *M and N or M forms. When the exciplex or excimer decays to the ground state, it then dissociates to form

unbound M and N molecules [102], [103].

A good example of the latter process can be found in the pyrene excimer system. An excited-state pyrene molecule can form a pyrene excimer with a nearby ground-state pyrene molecule. The fluorescence of the pyrene is at about 405 nm; whereas, the *[MM] excimer emits at ca. 460 nm [104]. A common application occurs in the noble gas – halide exciplex lasers. These lasers capitalize on the formation and subsequent dissociation of the exciplex state to create a population inversion resulting in pulsed lasing action from the excimer [105]. These lasers are very strong (typical pulse energies of 250 mJ) and emit in the deep UV part of the electromagnetic spectrum [106].

1.5 P4VB (1,4-bis(4-pyridyl-π)-vinyl) benzene) and its derivates

My work in this thesis involves a new chromophore with a wide color tunability across the visible spectrum. The design of this chromophore, its optical character, and its potential applications will be discussed in the following sections. It also features in the three main publications forming Chapters 3, 4, and 5 of this thesis. The chromophore has a UIPAC name bis(4-pyridyl)dineopenytoxyl-p-phylenedivinylene (np-P4VB) and was synthesized by our ATUMS collaborator, Dr. Sergey Vagin, at the Technical University of Munich (TUM). All of the optical work was done at the University of Alberta and will be discussed in detail in the experimental section.

The chemical structure of np-P4VB is a derivative of distyrylbenzene (DSB) (Fig. 1.1). DSB has an $S_0 \rightarrow S_1$ absorption peak at ca. 365 nm and a fluorescence peak in the violet, at around 400 nm. Previous studies on DSB indicated little solvent dependence on the emission spectrum [107]. The introduction of different substitutes leads to various DSB derivatives. One example is 1,4-bis(β-pyridyl-2-vinyl) benzene (P2VB), which is different from DSB insofar as

it has pyridine endgroups, with the nitrogens located on the 2-position (Fig. 1.17b) [107]. The basic fluorescent properties of P2VB were first studied by Ebeid et al., who determined that its emission peaked at about 400 nm upon excitation with a 337-nm nitrogen laser. Protonation of the pyridine groups caused a weak fluorescence wavelength shift from 414 nm to 423 nm [108]. However, there were no further studies of P2VB since then.

P4VB was first reported in Ref. [108], but was barely studied since (in fact, there are no subsequent works). In comparison to P2VB, P4VB has the nitrogen atoms located on the pyridine 4-positions, so the electron cloud associated with the unpaired electrons are more easily accessible. The P4VB molecules have a blue-violet $S_1 \rightarrow S_0$ emission centered at 450 nm in dimethyl sulfoxide (DMSO). The QY was reported to be as high as 65% at 10^{-5} M concentrations in DMSO, decreasing for more concentrated solutions (10^{-2} M) [108]. The formation of the P4VB excimer gave an additional peak at 490 nm. The emission of P4VB was reported to a redshift by 50 nm [108], which is larger than the shift of the protonated P2VB, likely because of the easier accessibility of the nitrogen atom in the pyridine groups.

For this work, bulky and low-reactivity neopentyl ($C_2H_{12}O$) side groups were attached to the P4VB base conjugated structure (Fig. 1.17d). This improves the solubility in organic solvents and limits the intermolecular reactions (e.g., excimer formation), while retaining the accessibility of the nitrogen atoms. This chromophore was initially synthesized to be a fluorescent linker in a metal-organic framework [109]. When initially characterizing this chromophore, we found a surprisingly strong fluorescence color shift and lasing capability across the visible spectrum [33], leading to several more thorough investigations presented in this thesis. This work will be described in the main research chapters to follow.

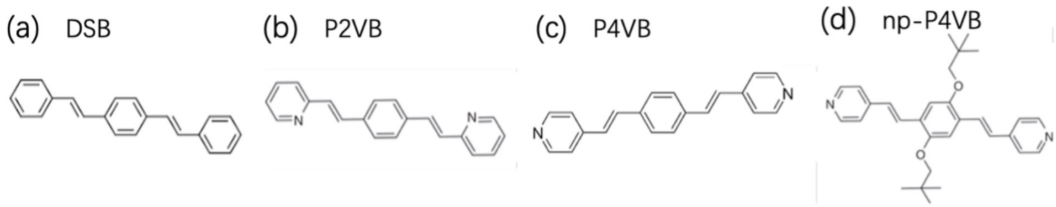

Figure 1.17: Chemical structures of (a) DSB, (b) P2VB, (c) P4VB [108], and (d) np-P4VB.

1.6 Brief Conclusion

The purpose of this introduction was to compactly introduce and review the basic photophysics and emission mechanisms common to organic fluorophores. Of course, this is a huge field, so this chapter presented an attempt to condense the material as a reference source of relevance to the scientific work presented in the following chapters. We first categorized organic fluorophores into some general types and families, in order to place the P4VB fluorophore as a member of the DSB family of organic dyes. Then some fundamental properties of organic fluorophores, including the elementary photophysics that one generally needs to understand in the field, was provided in a short reference-style format. This introduction finally gave a brief background on the fluorophore that forms the main topic of the investigations to follow.

Chapter 2

Experimental methods

All of the published chapters that follow contain an experimental section. The purpose of this section is to provide a more detailed description of the procedures so that they can be more easily reproduced if necessary in future studies.

2.1 Making P4VB solutions

Stock dye solutions were made by weighing out typically 17 mg P4VB on a laboratory scale (Sartorius, ±0.1 mg) and dissolving it at room temperature in 20 mL of an organic solvent (e.g., toluene, dioxane, ethanol DMF, DMSO, benzene, or acetone) to obtain an np-P4VB concentration of 2 mM. A magnetic stir bar was used to aid the dissolution of the dye. The dye solutions were then diluted from the initial stock solutions to produce the desired concentrations.

2.2 Fluorescence spectroscopy

2.2.1 Solution-based fluorescence and absorption measurements

To measure the fluorescence of the solutions, the solutions were put into a 3 mL fused quartz cuvette or 1 mL fused quartz microcuvette (if the solution volume was small). The cuvette was held on a 3D printed cuvette holder. Flu-

orescence was collected by an optical fiber, sent through a longpass filter, and then through another fiber connected to an Ocean Optics 2000+ spectrometer. A longpass filter was used to block the excitation light. The pump light is was from a UV-optimized Argon ion laser with laser lines at 352 and 364 nm. The fluorescence spectra were collected using the SpectraSuite software package.

The spectrometers were always intensity calibrated by using a standard reference light source. The calibration process was done by taking a reference spectrum first, and then taking a dark spectrum. The software then corrects the reference spectrum using the formula $I_\lambda = P_{\lambda,T} \cdot \frac{I_{S,\lambda} - I_{D,\lambda}}{I_{R,\lambda} - I_{D,\lambda}}$,where I_λ is the intensity at wavelength λ, the subscript S refers to the sample spectrum, D refers to the dark spectrum, and R is the reference spectrum. $P_{\lambda,T}$ is the Planck spectrum for the known temperature of the calibration lamp. Every subsequent collected spectrum is then corrected in the same way.

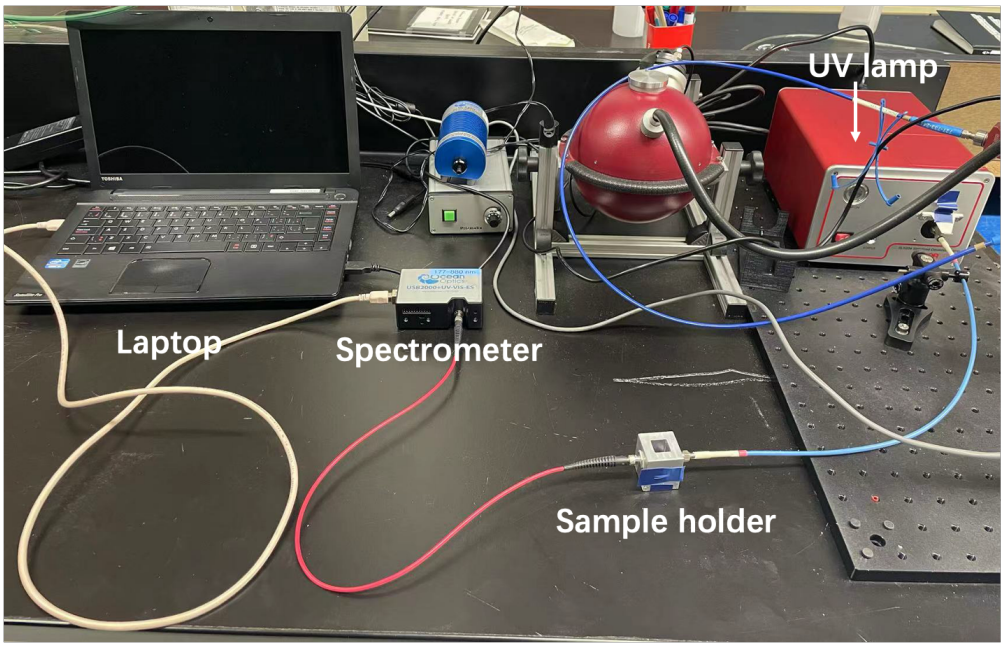

Figure 2.1: A photo of the absorption setup. An integrating sphere (used for PLQY) is in the background.

Absorption spectroscopy was performed using an Ocean Optics 2000+ spectrometer (117-880 nm) where the excitation light was from a SLS204 stabi-

lized deuterium lamp. The spectrometer, the lamp, and dye solutions were interfaced using optical fibers (Fig. 2.1). The absorption measurements used the same 3 mL fused quartz cuvettes, with a pure solvent used as the blank. The np-P4VB solutions had to be diluted to a final concentration of about 100 μM. The absorbance of the sample at a certain wavelength λ is given by $A(\lambda) = Log_{10}\frac{I_{B,\lambda}-I_{D,\lambda}}{I_{S,\lambda}-I_{D,\lambda}}$, where I_λ is the intensity at wavelength λ, and the subscripts S, B, and D represent the sample, blank, and dark spectrum, as before.

2.2.2 Fluorescence lifetimes

Fluorescence lifetimes were measured using an pulsed diode laser at 405 nm (Alphalas Gmbh) with 40 ps pulses. The luminescence was collected by using an optical fiber (numerical aperture = 0.5), passed through a longpass filter, and then detected by an HPM-100-50 hybrid PMT (Becker-Hickl). The PMT has a response time of $\sim$ 200 ps. The data were collected using the photon counting software package SPCM64 from Becker-Hickl (Fig. 2.2).

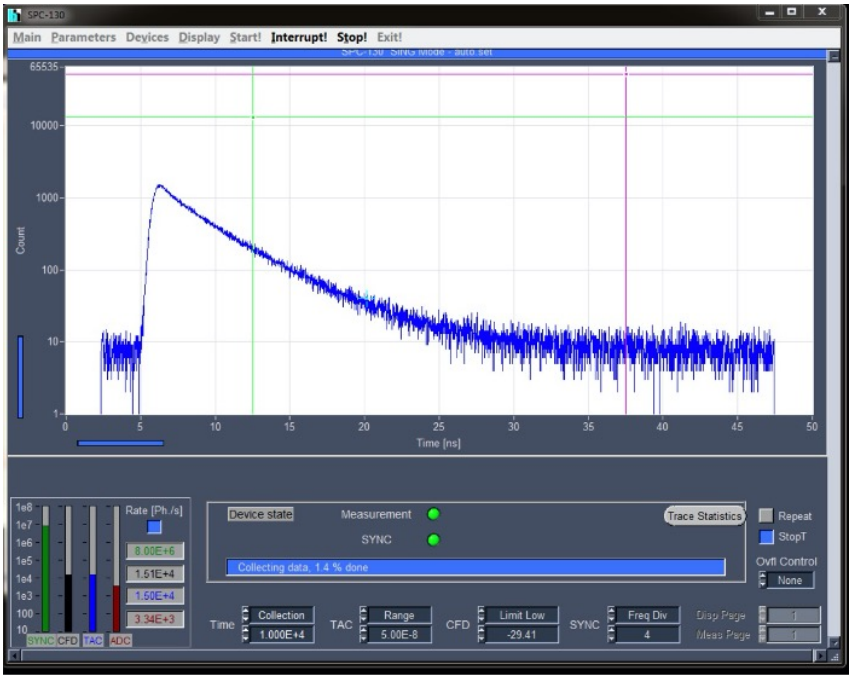

Figure 2.2: A screen shot showing the data collection for the time resolved PL.

2.2.3 Fluorescence quantum yield (QY)

The QY was measured in an integrating sphere with a 365 nm LED excitation source (Prizmatix) (Fig. 2.3). First, the np-P4VB solutions were prepared with absorbance between 0.1 and 0.2 at the excitation wavelength. Two 3 mL quartz cuvettes were filled with the np-P4VB solution and the plain solvent blank. The cuvette has a white cap with a magnet, which can be fixed on the holder in the integrating sphere. The 365 nm LED was connected with a power meter and the inlet of the integrating sphere.

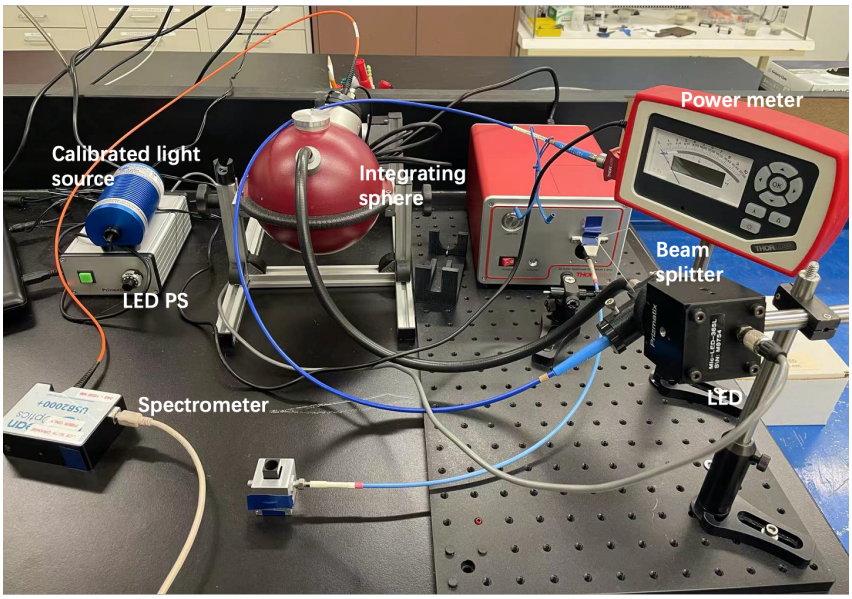

Figure 2.3: A photo of the QY measurement setup.

The QY measurements require six spectral data files. These are:

1. Calibrated reference spectrum
2. Calibrated dark spectrum
3. Blank PL spectrum
4. Blank dark spectrum
5. Sample PL spectrum
6. Sample dark spectrum

Each of these files was collected with the the setup shown in Fig. 2.3. The LED and spectrometer were allowed to warm up and stabilize for 15-30

minutes. The power output of the LED was continuously monitored with a power meter and adjusted accordingly if it was found to drift at all during the measurement. The final calibration and calculations for the QY were done by using a Mathematica code written for this purpose by William Morrish and Al Meldrum.

2.3 Fluorescence imaging of np-P4VB MOFs

In my first paper, I worked on the np-P4VB metal-organic frameworks (MOFs) to find the color-switching and polarized emission. The np-P4VB molecules were used as organic ligands in the MOFs, which formed square layered platelets (about 150 μm along their long edges). The np-P4VB MOFs were synthesized in DMF by our collaborator Dr. Sergei Vagin in department of chemistry at TUM.

First, I prepared the np-P4VB MOFs on a glass substrate in air. A small number of np-P4VB MOFs in DMF (dimethyl formamide) were collected by using a glass pipette, and were transferred with some DMF solution to the surface of the glass substrate. The DMF needed to be evaporated for about 5 minutes until the surface was dry.

Then the substrate was put on the microscope stage to take fluorescence images. The excitation light source was a 405 nm LED. The light from the LED was focused on the MOFs and the fluorescence was collected through a 10X objective lens and imaged using a Retiga 1350EX fluorescence camera. The fluorescence images were collected and saved using the Q-capture software in computer.

The MOFs were next exposed to HCl in order to change their color from green to orange. The acid effectively protonates the P4VB ligands, as described in chapter 3. Direct contact between MOFs and HCl solutions was found to break the structure of the MOFs. So instead I used the vapor from

a strong HCl (12 M) solution. Small volumes of the HCl solution were taken with a glass pipette, and then the pipette was kept about 1 cm above the MOFs for 10 seconds. The color of MOFs can change to orange within ∼10 seconds.

In order to investigate the polarization of the fluorescence emission of the np-P4VB MOFs, a polarizer was placed between the 405 nm LED and the sample, which served both to polarize the LED excitation and acted as an analyzer for the fluorescence. Fluorescence images of np-P4VB MOFs were taken at different polarization angles relative to the MOF platelets. Then the fluorescence images were imported into Mathematica to read the fluorescence intensity and to plot the relationship between fluorescence intensity and the polarization angle.

2.4 Paper-based CO_2 sensors

The paper-based CO_2 sensors were fabricated by dipping a piece of filter paper (Fisher brand P4 grade filter paper) into a P4VB solution (0.2 mM) in ethanol that had been prepared as described above. After the filter paper was filled with dye solution, the solvent was allowed to evaporate over 15 minutes, leaving the P4VB dispersed in the cellulose fibers of the filter paper. Alternatively, the P4VB solution was placed on the filter paper by using a glass pipette, depositing three drops of the solution onto the paper, and allowing it to dry.

2.4.1 CO_2 gas sensing

The CO_2 gas sensing apparatus was constructed by using quarter inch tubing and two gas controllers (Fig. 2.4). The gas cylinders contained nitrogen (99.998% purity) and CO_2 (98% purity). The nitrogen gas was used as the carrier gas, and the tubing connected with two gases had a CO_2/N_2 test gas mixture. The CO_2 concentration was controlled by adjusting the ratio of the flow rates, which were varied from 0 to 5 NL/h (NL = normal liters, "normal" means the normal conditions with a given temperature (20^oC) and pressure (1

atm)) of the two gases in different experiments. The two knobs can be used to change the flow rate, and numbers can be read from the position of the cones in the gas controllers (Fig. 2.4).

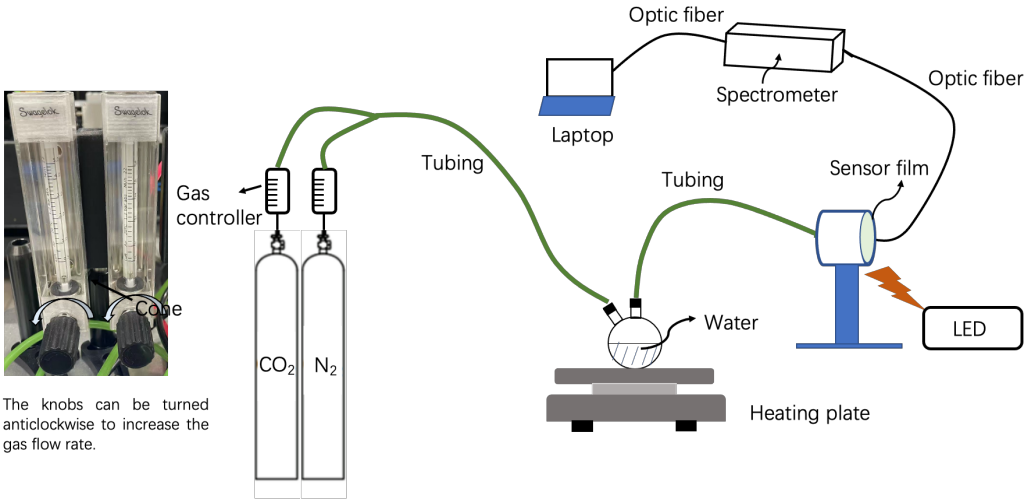

Figure 2.4: A diagram of the CO_2 sensing experiments. The LED wavelength was 365 nm. The sensor paper was put in a cylindrical holder to receive the mixture of gas.

The mixed gas was delivered into a flask containing water at 40^{o}C. This temperature was controlled by a hot plate. Heating increases the amount of water vapor, which in turn increases the formation of H_2CO_3. In some experiments, the standardized CO_2 line was replaced with room air (contains about 410 ppm CO_2) or human breath (contains 4-5% CO_2) to test the sensing ability of the filter paper in some more complicated gas mixtures.

The np-P4VB-infused filter paper was excited by a 365 nm LED (Prizmatix) and the fluorescence was collected by an optical fiber and delivered to an Ocean Optics USB 2000+ spectrometer (340-1030 nm). The spectral data were collected using the SpectraSuite software package, which allows automatic saving at a prescribed time interval. In order to create a sensorgram, the system was set to save the fluorescence spectrum every 5 seconds.

2.5 Sensing with fluorescent microfluidic droplets

In my third paper, I needed to prepare octanol fluorescent droplets (oil phase) containing np-P4VB. These oil droplets are dispersed on the surface of a hydrophobic silicon (Si) wafer in an aqueous environment. This technique was developed in the Zhang lab (CME, University of Alberta) (Fig. 2.5) and is described further below.

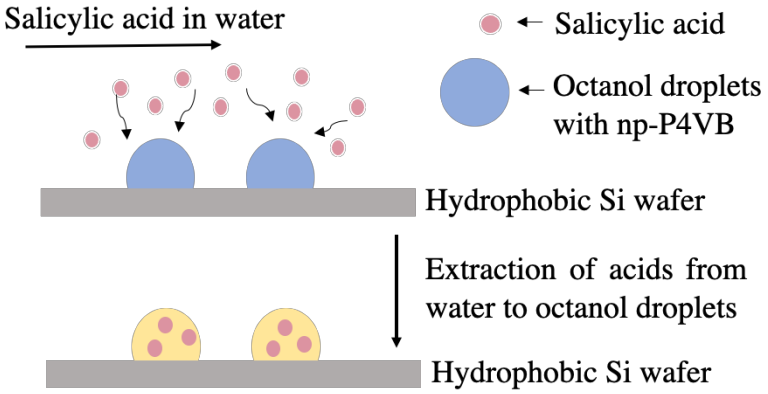

Figure 2.5: A diagram illustrating the sensing principle. The octanol droplets stay on the surface of the hydrophobic Si wafer. When the aqueous solutions containing salicylic acid are pumped over the octanol droplets, the salicylic acid preferentially enters the droplets.

2.5.1 Formation of fluorescent microfluidic droplets in the fluid chamber

First, the three solutions used in the solvent exchange method needed to be prepared. These will be referred to as solution A, solution B, and solution C. Solution A was a mixture of octanol, ethanol, and Milli-Q water at a volume ratio of 3:50:50 with 0.23 mM or 0.023 mM np-P4VB dissolved in this mixture. The ethanol worked as the co-solvent for the water and octanol; otherwise largely immiscible water and octanol cannot mix sufficiently well.

Solution B was octanol-saturated water. To produce solution B, octanol was added into the water until some octanol could not be dissolved; then satu-

ration was obtained by shaking the mixture periodically over about four days. Because the density of octanol is lower than that of water, the over-saturated octanol floats on the surface of water. The octanol-saturated water was extracted by using a glass pipette. Solution B can be prepared in a relatively large volume of ∼20 mL.

Solution C was the analyte solution. In my work, solution C was salicylic acid (IUPAC name: 2-hydrobenzoic acid) in octanol-saturated water. The amount of salicylic acid powder was weighed using laboratory scale (Sartorius, ±0.1 mg) according to the required concentrations, and then these powders were dissolved in the octanol-saturated water. The volume of solution C that could fit into the syringe was 5 mL.

After the preparation of solution A, solution B, and solution C, the next step was to set up the fluid chamber (Fig. 2.6). The fluid chamber mainly consists of inlet tubing, outlet tubing, a spacer, a hydrophobic silicon wafer (∼1 cm × 1 cm), and a transparent cover glass. The silicon wafer was prepared by coating it with 95% octadecyl-trichlorosilane (OTS) (which was done by students in the Zhang lab). The OTS-coated hydrophobic silicon wafer then affixed to the bottom of the fluid chamber by using a small piece of the double-sided tape (smaller than the wafer). Then the spacer was put on the bottom of the fluid chamber. The cover glass was put on the spacer to create a sealed area around the OTS-coated wafer and fixed tightly by using four clips (Fig. 2.6).

Finally, the droplets were formed on the silicon wafer by pumping solution A and then solution B inside the chamber. First, solution A (3 mL) was pumped into the fluid chamber by using a 5 mL biocoat disposable (BD) syringe until the area between the cover glass and the wafer was full. Then 5 mL of solution B was pumped into the fluid chamber by using the same syringe. During this process, the pump rate needed to be slow enough to ensure the formation of the droplets with a suitable size. If the rate is too

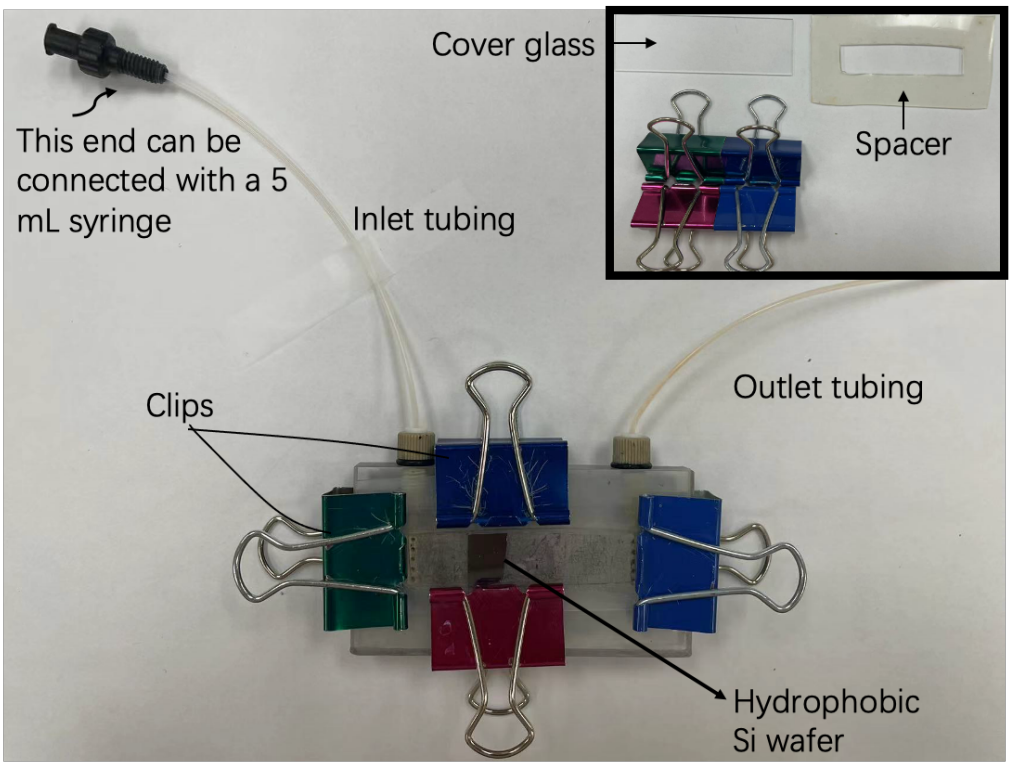

Figure 2.6: A photo of the fluid chamber and related attachments.

fast, the droplets can be too large. The Nanojet syringe pump was used to control the pump rate at 15 mL/h. When solution B was fully pumped in the chamber, the droplet formation was considered finished. Finally, solution C (the analyte) was injected using another syringe, which replaced the empty syringe during the previous step, and was likewise connected with the inlet of the chamber.

2.5.2 Fluorescence imaging and analysis of the microfluidic droplets

The fluorescence of the np-P4VB droplets was monitored on a Nikon TE2000e inverted epifluorescence microscope using a 405 nm LED as the excitation light source. The fluid chamber was fixed on the stage of the microscope, and the syringe pump was also put on the microscope stage near to the chamber (Fig. 2.7). The syringe connected with the chamber was fixed on the syringe pump, and the pump rate was set at 15 mL/h. An empty beaker was put under the

outlet of the chamber in order to collect the waste solutions from the chamber.

The light from the LED was focused on the droplets and the fluorescence was collected via a 20X objective lens with a numerical aperture of 0.4. A Sony α6400 digital camera was used for imaging the droplets. When the fluorescent droplets were located in the live image, the syringe pump was then turned on. Solution C was then pumped into the fluid chamber at a rate of 15 mL/h. At the same time, the camera was used to take fluorescence images of the droplets every minute. In order to minimize photobleaching effects, the LED was always turned off unless a photo was being taken.

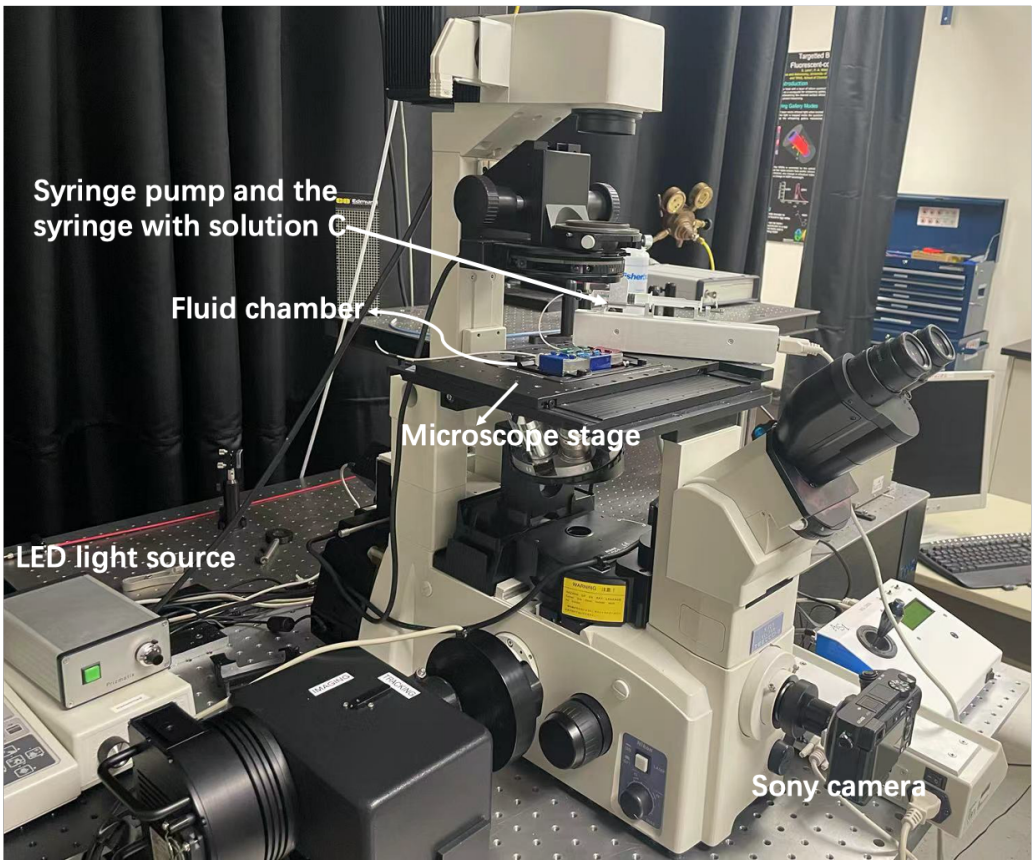

Figure 2.7: A photo of the Nikon microscope, the syringe pump and fluid chamber.

After collecting the fluorescence images of the droplets, the analysis of the images was done by using ImageJ, an open-source image-processing software

package. ImageJ can split the images of the fluorescent droplets into red, green, and blue channel (Fig. 2.8). In order to analyze the color change of the droplets, I chose a pixel area (20 × 20 pixels) on the center of one droplet and read the average pixel intensity of this area from each color channel. For each channel, the chosen center position and the pixel area on the droplet was kept the same.

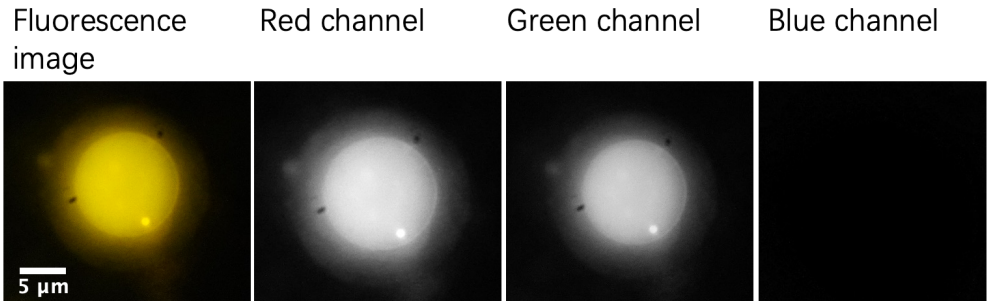

Figure 2.8: A fluorescence image of a droplet, showing the three-color channel split.

2.6 Conclusion

This chapter mainly showed how to measure the optical properties of the dye solution, such as fluorescence from the solution and solid state, absorption, lifetime, QY, and fluorescence microscopy. All experimental steps and notables, such as the preparation of the dye samples, were also described in more detail than in the published chapters to follow. During the experiments I also met some unexpected experimental difficulties, like the photobleaching effects from LED in droplet experiments, and these issues were discussed as well.

Chapter 3

Metal-Organic Framework with Color-Switching and Strongly Polarized Emission

3.1 Introduction

Organic chromophores are widely used for biological imaging [110], [111], biorecognition [112], sensing [113], [114], and laser applications [115]. These functions generally require a chromophore with good photostability and high fluorescence quantum yield. For many applications, the fluorescence should also change controllably in response to certain environmental stimuli. For example, chemical sensing of pH [114] or explosives [116] is often achieved by measuring the fluorescence quenching due to charge transfer between the chromophore and the analyte [117]. For biological imaging, a color change can indicate the presence of specific biogenic conditions [118], and wide control over the emission wavelength is important for display technologies and tunable lasing applications [119]. Color-changing chromophores also have potential applications for monitoring the intensity of pipelines and other structures used for oil and gas extraction or wind energy [120].

Solvent-medicated changes in the absorption or fluorescence spectrum of π-conjugated organic chromophores are well known. The polarity of the host solvent can modify the electronic structure of organic chromophores (i.e., solvato-chromism) including coumarins [121], [122], indoles [123], hemicya-

nines [124], pyrazines [125], fluorescein [126], and many others. Whether the energy gap increases or decreases depends on the degree of stabilization of the ground and excited states [127], [128]. Neglecting specific solvent interactions, the overall scale of the solvatochromic shift is related to the relative difference in the dipole moments associated with the levels involved in the luminescent transition [95]. Building these switchable fluorescent properties into metal-organic frameworks (MOFs) in which the ligand chromophores can be strongly aligned suggests a means to achieve exceptional control over the luminescence, as compared to the absorption-based color changes recently reported [129]–[131].

Charged species in the solvent can also weakly bind to the chromophore, redistributing its electronic states and changing the resulting absorption and luminescence spectra. This mechanism is of great interest in the development of luminescent pH detectors and chemosensors. It is especially common in conjugated molecules having cyano or pyridine groups due to the susceptibility of the nitrogen atoms to protonation [132]–[137]. Protonation can cause large changes in the energy gap of many conjugated organic chromophores, often due to extensive electronic delocalization in the excited state [138], [139]. Fluorescence quenching can also occur upon protonation of molecules that emit via internal charge transfer [140]. However, the properties of crystalline phases exposed to protonating or deprotonating agents have been reported in only few cases [133], and in the case of luminescent MOFs, only a quenching effect has been observed to date [141], suggesting potential applications in explosives sensing [142]–[144].

In this work, we synthesize a linear aromatic scaffold of the distyrylbenzene class, in which the outer benzenes are replaced by reactive and accessible pyridine groups. The molecule was designed as a platform for hybrid structures such as metal-organic frameworks (MOFs) and metal-ion complexes in which the luminescence properties such as emission wavelength and polarization states can be controlled. The large amount of recent work on

protonation-induced quenching and color shifts in luminescent dyes implies novel applications of these chromophores as scaffolds for larger complexes and solid-state materials exhibiting extensive control over the fluorescent properties. MOFs in particular are of interest for novel solid-state luminescent materials [145]–[147], but polarized and color-controlled luminescent MOFs have not yet been reported.

3.2 Experimental section

A linear organic chromophore [bis(4-pyridyl)dineopentoxyl-p-phenyl- enedivinylene (np-P4VB)] was synthesized as the fluorescent scaffold. It has a conjugated backbone consisting of one benzene ring and two terminal pyridines having the nitrogens in the highly accessible fourth position, as well as bulky neopentoxyl side groups intended to minimize intermolecular interactions (a structural diagram is shown in the inset of Fig. 3.1b). We recently described the synthesis of np-P4VB in detail [119] and the same procedure was used here.

The accessibility of the pyridyl groups in np-P4VB for coordination with metal ions allows incorporation of this chromophore as a building unit in the MOF structure. We previously demonstrated that a similar chromophore with methoxy substituents instead of neopentyloxy forms microcrystalline-pillared "TDC-MOF-7" upon reaction with 9,10-triptycenedicarboxylic acid (H_2TDC) and zinc nitrate in dimethylformamide (DMF) [148]. However, the small size (a few micrometers) and irregular shape of the resulting crystals hindered any single-crystal photonic application of the material. The unsatisfactory results in terms of crystal size and shape may have originated from the poor solubility of the methoxy-substituted chromophore. Furthermore, TDC-MOF-7 rapidly decomposed after removal of the guest DMF molecules from the MOF scaffold. We hypothesized that all these negative features could be diminished upon utilization of a chromophore with bulkier substituents.

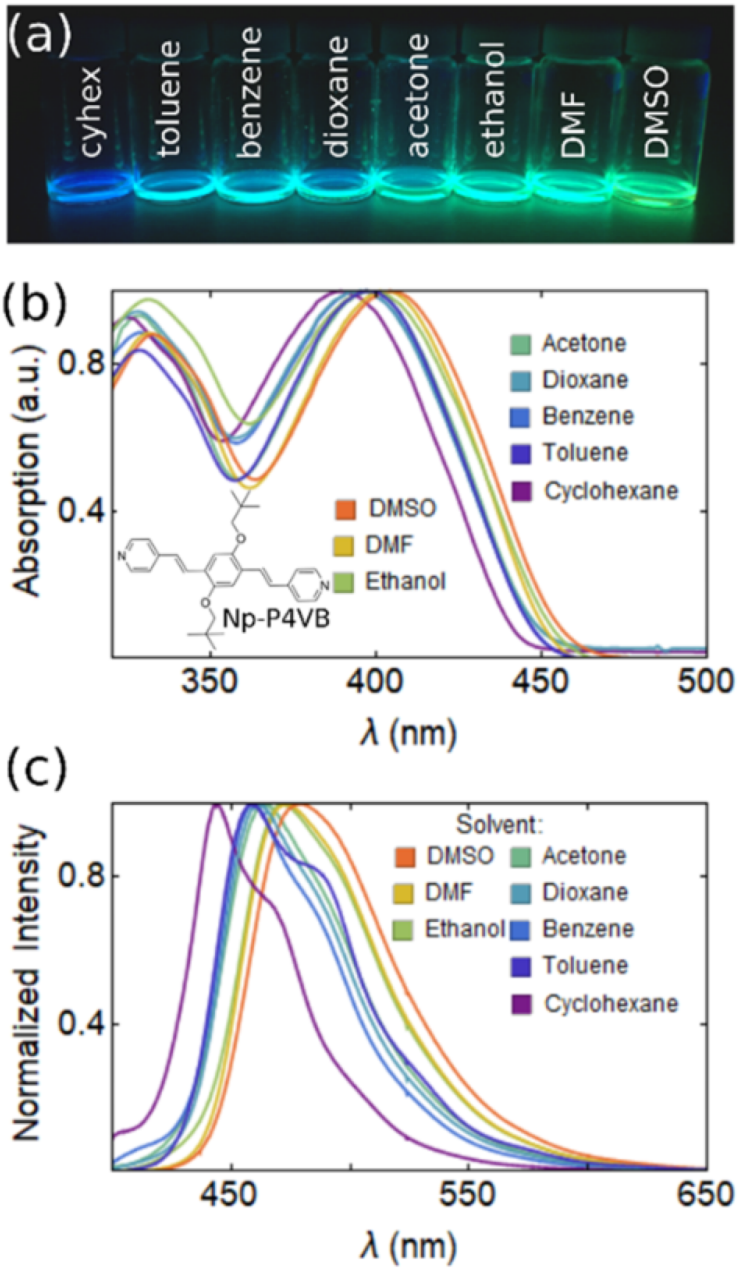

Figure 3.1: (a) Photograph of np-P4VB (2.0 mM, except cyclohexane at 0.7 mM) dissolved in various solvents. The photograph was taken under a blacklight. The corresponding absorption and photo-luminescence spectra are shown in (b) and (c), respectively. The data are normalized to clearly compare the peak wavelengths for the various solvents. Reprinted with permission from Chem. Mater. 2019, 31, 15, 5816–5823. Copyright 2019 American Chemical Society.

In a typical reaction, dissolution of equimolar amounts of np-P4VB, H_2TDC, and $Zn(NO_3)_2{\cdot}4H_2O$ in DMF with, e.g., 10 mM concentration of zinc gave a homogeneous orange reaction mixture, which was subsequently filtered and heated at 90^oC. Formation of bright-yellow crystals of np-P4VB TDC-interlinked MOFs (TDC-MOF-8) on the walls of the reaction vessel occurred within few hours. The reaction was continued for 1-2 days. After removal of the supernatant, washing with pure DMF by decantation, exchanging the washing solvent to CH_2Cl_2, and subsequent drying in vacuo, solvent-free MOF material was prepared with yields of up to 75% (calculated for Zn). Fourier-transform infrared spectrum indicated the presence of some amine contaminations in the MOF, but no free DMF. Certain variations of crystal habit and size were observed in experiments with different ratios of the reagents, different concentrations, different solvents, e.g., diethyl formamide, or N-methylpyrrolidone, different temperatures, or in presence of various additives. Particularly, addition of acetic acid improved the shape and size of the TDC-MOF-8 crystals (Fig. A.1).

The crystalline product was analyzed by powder X-ray diffraction at room temperature using a STOE Stadi P diffractometer equipped with a Ge (111) monochromator for Cu $K_{\alpha 1}$ radiation (λ = 1.54056 Å) and a Dectris Mythen DCS 1 K solid-state detector. Alternatively, a PANalytical Empyrean diffractometer was used.

Fluorescence spectroscopy was performed using the 351-364 nm lines of an Ar^+ ion laser as the excitation source and an intensity-calibrated miniature spectrometer from Ocean Optics. Fluorescence lifetimes were measured using a picosecond pulsed diode laser at 405 nm (Alphalas GmbH) interfaced to a HPM-100-50 photomultiplier tube from Becker-Hickl with a response time of about 200 ps. The decay traces were obtained using the SPC-130 module from Becker-Hickl. Absolute quantum yield (AQY) was measured in an adapted integrating sphere with a 405 nm light-emitting diode (LED) excitation source. Fluorescence microscopy also used a 405 nm LED for exci-

tation equipped with a setup for measuring the fluorescence polarization state.

3.3 Results and discussions

We start by investigating the solution properties of the fluorescent np-P4VB chromophore used as the MOF scaffold. The dry material formed fibrous yellowish needles up to several mm in length with a green-yellow fluorescence peaking at about 550 nm. The np-P4VB crystals dissolved well in a variety of common solvents including toluene, dimethyl sulfoxide, ethanol, DMF, hexane, and several others (Table 3.1). In pure solvents, the solution fluorescence spectra peaked in the teal or blue part of the spectrum (Fig. 3.1a,c), while the absorption spectra were characterized by two peaks, one in the UV and the other in the violet region (Table 3.1 and Fig. 3.1b). The absolute quantum yield varied from 50 to 68% in various pure solvents. The fluorescence lifetimes showed a single exponential decay (Fig. A.2) with lifetimes between 1 and 3 ns (Table 3.1).

Table 3.1: Absorption and Fluorescence Characteristics of np-P4VB in Different Solvents. Reprinted with permission from Chem. Mater. 2019, 31, 15, 5816–5823. Copyright 2019 American Chemical Society.

Solvent	$\lambda_{abs,1}$ (nm)	$\lambda_{abs,2}$ (nm)	λ_{PL} (nm)	τ (ns)	AQY (%)
acetone	328	398	464	2.24	58
benzene	328(303)	394(388)	459	2.02	59
cyclohexane	325	389	444	1.86	50
dioxane	328	395	461	2.24	55
DMF	331(307)	402(394)	473(525)	2.37	59
ethanol	331	398	472	2.35	61
toluene	328	398	458	1.89	55
DMF, $Zn(NO_3)_2{\cdot}4H_2O$	318(325)	419(426)	537(574)	3.09	49
Zn-MOFs			513	2.09	
DMF, HCl	366(347)	460(462)	591(613)	2.83	25
Zn-MOFs, HCl			600	2.43	

The PL and absorption wavelengths are related to the static dielectric constants (ε) of different solvents, with the luminescence shifting toward longer wavelengths for larger values of ε (Fig. 3.2a). Within the set of solvents having a uniformly low dielectric constant (i.e., $\varepsilon < 3$), the wavelength shift could still be correlated with related parameters such as the polarity index [149] (Fig. 3.2b). Thus, the solvent polarity plays a clear role in the positive solvatochromic shift in np-P4VB luminescence, which can be extended over a range of about 35 nm from deep blue to teal green. Some scatter in the data can be related to a variety of secondary effects related to specific solute-solvent interactions [150].

In general, the AQY increased for a longer-wavelength emission, as did the nonradiative luminescence decay time (Fig. 3.2d), where the radiative and nonradiative decay times were extracted from the AQY and the overall luminescence decay assuming a two-level system. However, there was no relationship between the radiative lifetime component and the other parameters (Fig. 3.2c). Similar trends were observed when these parameters were plotted as a function of the absorption peak wavelengths. Thus, the solvent appears to affect the nonradiative decay mode more strongly than the radiative one, implying that the purely vibrational decay modes become less probable as the solvent polarity increases.

Stronger effects were observed when the solvent contained impurities that can interact with the pyridine groups, as shown by the addition of the nitrate of Zn^{2+} or an acid (H^+), which shifted the luminescence from blue to green or red, respectively (Fig. 3.3a). For a concentration of 10 μM np-P4VB in ethanol, the PL shift from blue to red saturated at 100 μM HCl, i.e., 10 times higher concentration as compared to that of the base chromophore. At higher chromophore concentrations above 1 mM, the ratio became closer to 1:2, which is suggestive of double protonation as expected on the basis of the molecular structure.

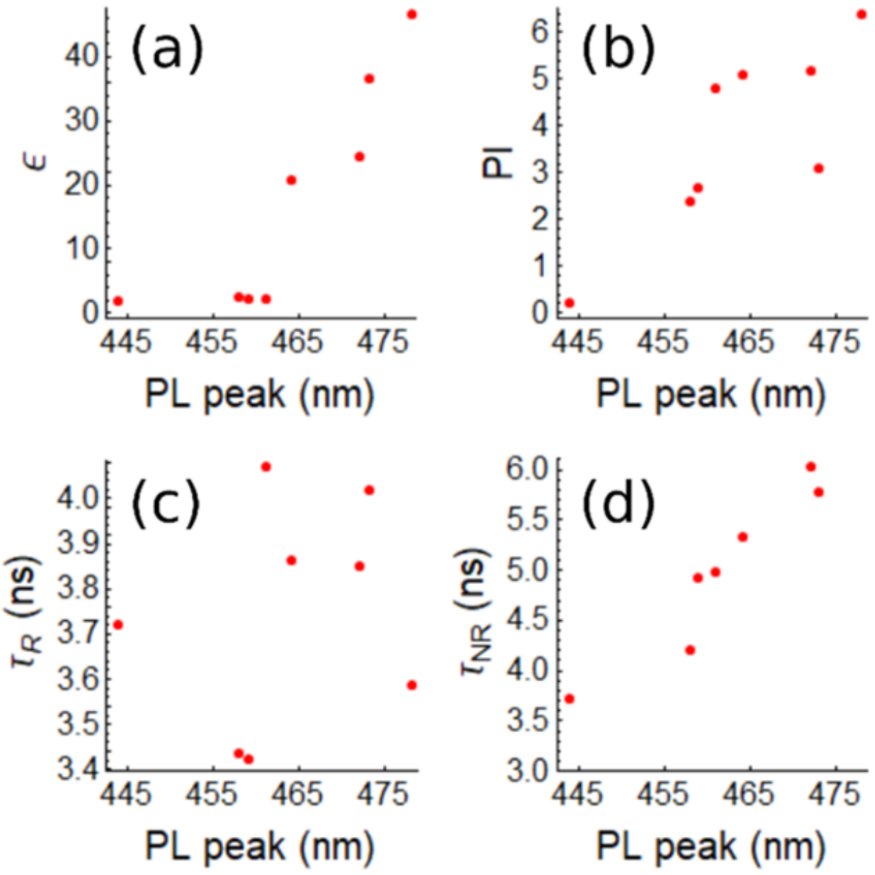

Figure 3.2: Relationship between the PL peak wavelength and (a) the static dielectric constant; (b) the polarity index; (c) the radiative lifetime; (d) and the nonradiative lifetime in various pure solvents (Table 3.1). Reprinted with permission from Chem. Mater. 2019, 31, 15, 5816–5823. Copyright 2019 American Chemical Society.).

The PL peak did not shift uniformly from blue to red with increasing acid concentration, rather the blue peak was gradually quenched while the red one became stronger (Fig. 3.3b,c). The red emission showed a double-peak structure at lower concentrations, gradually becoming a single-skewed emission band. Several previous studies have shown that aromatic molecules with this color-shifting property can be used as a sensitive pH sensor [151]. Here, a simple analysis of the PL peak position yielded a solvatochromic 3σ detection limit of 8 μM for HCl in water (pH = 5.1) at a chromophore concentration of 10 μM, which is similar to other color-shifting chromophores [152] and commercially available pH-sensitive [153].

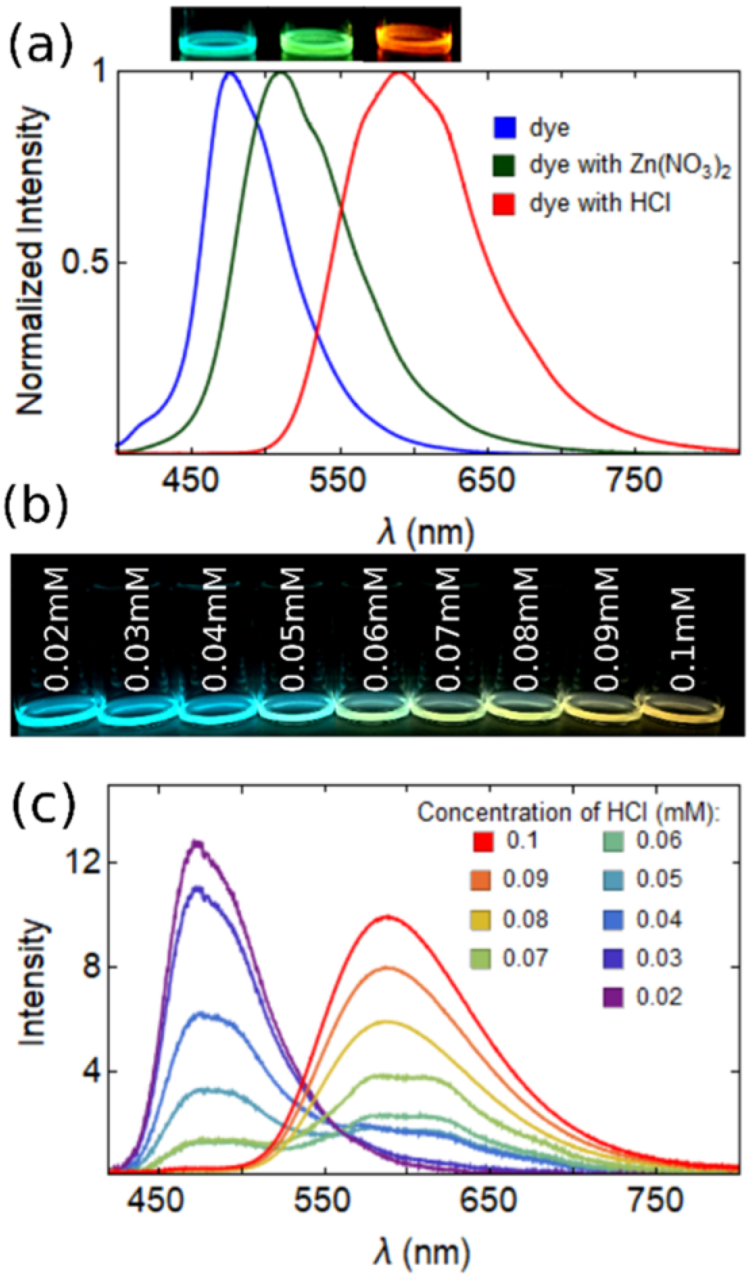

Figure 3.3: (a) Fluorescence spectra and photographs of np-P4VB (2 mM) in ethanol and with Zn^{2+} and H^+ (500 mM $Zn(NO_3)_2$ and 100 mM HCl respectively). (b) Blacklight photograph of np-P4VB (10 μM) in ethanol with different acid concentrations shown; the corresponding photoluminescence spectra are shown in (c). There is a hint of a double-peaked emission for intermediate acid concentrations, possibly suggesting a mixture of singly and doubly protonated states. Reprinted with permission from Chem. Mater. 2019, 31, 15, 5816–5823. Copyright 2019 American Chemical Society.

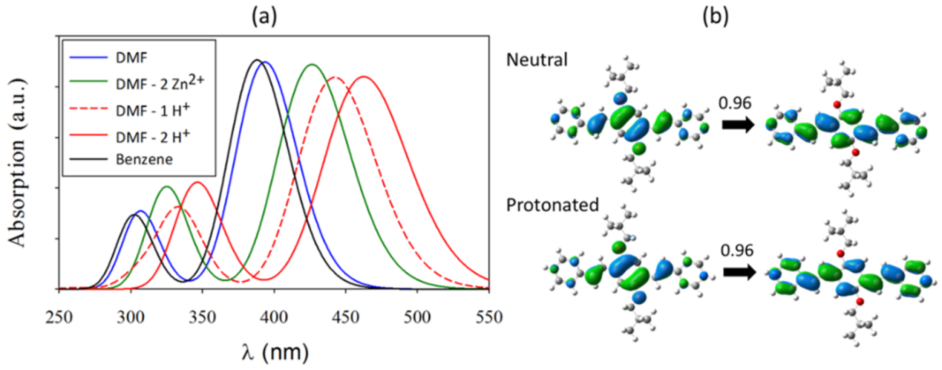

Figure 3.4: (a) Absorption spectra of np-P4VB computed at the time-dependent density functional theory (TD-DFT) level in different solvent environments. (b) Orbitals involved in the first transition (the highest occupied molecular orbital (HOMO) on the left and the lowest unoccupied molecular orbital (LUMO) on the right), as obtained from the natural transition orbitals (NTO) analysis, for the neutral and fully protonated species in DMF. Reprinted with permission from Chem. Mater. 2019, 31, 15, 5816–5823. Copyright 2019 American Chemical Society.

To undertand the role played by specific chromophore-ion interactions as the origin of the solvent-mediated shifts in the luminescence, a quantum chemistry analysis was performed. This was based on density functional theory (DFT) implemented in the Gaussian software package. The calculations used the CAM-B3LYP exchange-correlation functional and a 6-31++G(d,p) Gaussian basis set. Solvent effects were accounted for using the PCM implicit solvation model [154]. Specific interactions with ionic species in the solvent were captured from an explicit introduction of the species in the calculation. Optical absorption and emission properties were simulated using time-dependent DFT, neglecting vibrational effects, using the ground- and first-excited-state-optimized structures. The predicted DFT values are reported in brackets in Table 3.1.

The simulated absorption spectrum was dominated by two intense peaks in the 300-350 nm region and the 400-460 nm region (Fig. 3.4a). By modifying the dielectric environment to match with values reported for DMF and

benzene solvents, we recovered the experimental solvatochromic trend, with the calculations predicting the correct ordering for the two solvents. This finding agrees with the observed solvatochromism in Fig. 3.1 and 3.2, pointing to a dielectric polarization origin. The first excited state was simulated with a good quantitative accuracy, matching with the experimental value within less than 0.1 eV. The accuracy of the second excitation was somewhat lower, matching the experimental value within 0.3 eV.

Upon introduction of Zn^{2+} and H^{+} cations in the vicinity of the nitrogen group of pyridine, a significant redshift was observed at the theoretical level, in agreement with the experimental trend. The simulated first excitation peaks after binding at the nitrogen sites were also in good quantitative agreement, matching the experiment values within 7 nm. This directly points to the role of specific ion binding as the origin of the high control over the molecular luminescence. The successive introduction of first and second protons led to an intermediate peak shift (Fig. 3.4a), confirming the pH sensitivity of the molecule and suggesting that partial protonation might be the origin of the double-peak structure in Fig. 3.3c.

The first excited state natural transition orbitals (NTO) [155] for both neutral and fully protonated molecules (Figure 3.4b) showed that specific ion binding did not affect the nature of the transition, which was still a clear HOMO to LUMO $\pi - \pi^*$ transition dominating the NTO analysis (0.96 coefficient). However, ion binding promotes a better orbital delocalization, especially in the LUMO state in the region of the external rings. At the structural level, the specific ion binding led to a smaller twist angle between the central and external aromatic rings (19 vs 11°). This implies an increasingly extended conjugation that is induced and controlled by the presence of ions in the solution.

The emission wavelength was computed at the TD-DFT level and taking the Stokes shift into account (Table 3.1). Those were qualitatively in

agreement with the experimental results. The absolute match with the experimental emission peaks was less accurate than that for the absorption peaks, but the largest difference is still reasonable, within 0.3 eV for the neutral species. The trend that prevailed for the absorption spectra was still observed for the emission spectra, and the capture of ion provides the same control for both emission and absorption.

Experiments and the DFT calculations agree that np-P4VB shows extensive fluorescence wavelength tunability. This can be attributed to the excellent steric accessibility of the nitrogen atoms and the bulky, protective side groups that minimize intermolecular interactions. These properties, combined with the linear structure of the conjugated backbone, suggest that np-P4VB is an excellent candidate for the formation of more complicated molecular structures with extensive luminescence control.

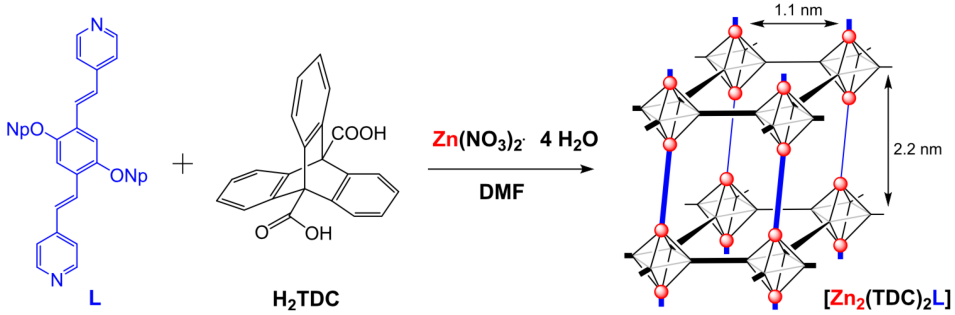

Figure 3.5: Illustration of the structure of TDC-MOF-8. The np-P4VB (blue) scaffold links the Zn-TDC square arrays into a slightly tilted layered structure. Reprinted with permission from Chem. Mater. 2019, 31, 15, 5816–5823. Copyright 2019 American Chemical Society.

After fully characterizing the chromophore, the next step was to demonstrate its ligand role in a metal-organic framework. We initially hypothesized that this might preserve the color-changing ability while taking advantage of the linear conjugated backbone to create a highly polarized and switchable emission. Following the procedure described in the Experimental Section, we built a "pillared" paddle wheel Zn-MOF in which the np-P4VB served as

the network of coordinating ligands ("TDC-MOF-8"; Fig. 3.5). Each paddle wheel cluster in this MOF is formed by two Zn^{2+} ions interlinked by four μ-O,O'-coordinated carboxylic groups of four TDC units. Each TDC unit thus interconnects two di-zinc clusters, resulting in two-dimensional ZnTDC layers with a square array topology. These layers are linked by the np-P4VB via coordination to the axial positions of the paddle wheel Zn^{2+} clusters at the each of the two pyridine end groups. According to the PXRD (Fig. A.3), the resulting MOF has a monoclinic unit cell and is stabilized by large neopentyl side groups, which, unlike in previous work [148] at least partly fill the voids between the fluorescent linkers.

The increased stability of TDC-MOF-8 allows removal of the solvent from the MOF pores without the complete destruction of the coordination network observed in related MOFs [142]. The color of the guest-free TDC-MOF-8 was stable and remained yellow after prolonged air exposure (weeks). Resolvation in DMF resulted in the reappearance of the PXRD reflection inherent to the originally synthesized MOF.

The np-P4VB MOFs formed layered square platelets up to about 150 μm on their long edges (Fig. 3.6a). This structural motif is consistent with the PXRD results and the crystal structure proposed in Figure 3.5. The layered appearance ultimately resulted in square platelets that were typically about 2 μm thick. The facets of the MOF platelets were not perfectly smooth but typically contained few small (about 5 μm) square cavities or depressions. The platelets tended to stack into "book-like" clusters that could be up to tens of micrometers thick.

The MOFs were characterized by a visibly greenish-yellow fluorescence, which peaked at 513 nm (Fig. 3.6b), a value that is similar to that reported in Table 3.1 for the interaction of np-P4VB with Zn^{2+} ions in solution. The fluorescence was found to be polarized nearly perpendicular to the platelet surfaces (Fig. 3.6c). The polarization anisotropy, A, was measured with the

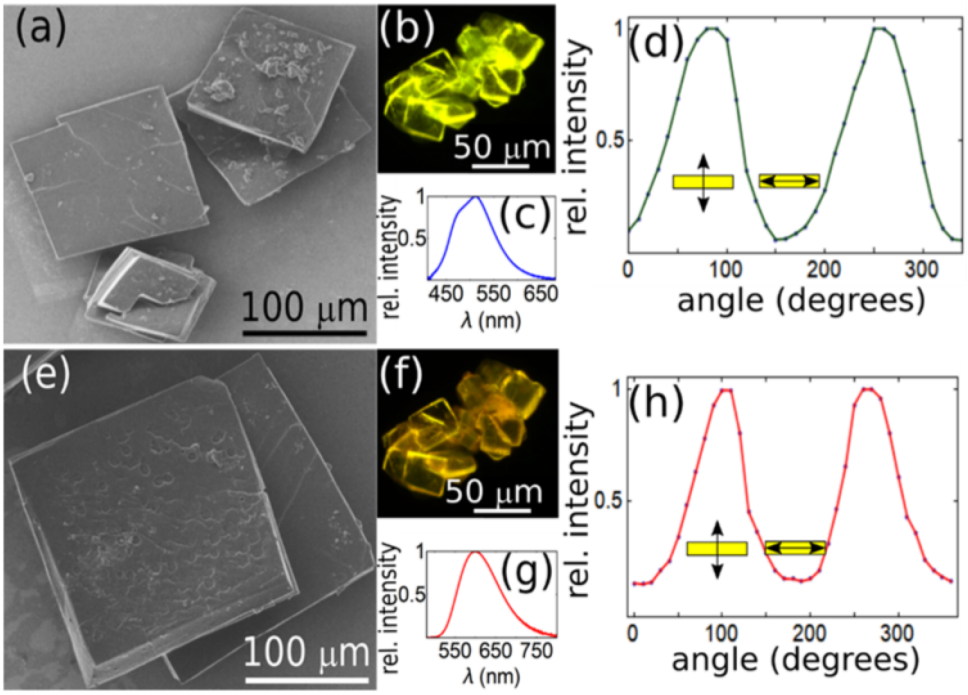

Figure 3.6: Structure and luminescence of np-P4VB MOFs before (a-d) and after (e-h) fuming with HCl. (a) Helium ion image of MOF platelets; (b) fluorescence image showing a cluster of MOFs; (c) MOF fluorescence spectrum; and (d) fluorescence polarization curve taken in the directions illustrated with respect to the MOF platelets. Panels (e) and (f) are the same as the first four panels after fuming the MOFs with HCl. Reprinted with permission from Chem. Mater. 2019, 31, 15, 5816–5823. Copyright 2019 American Chemical Society.

viewing direction parallel to the excitation direction, and the both excitation and emission polarizations maintained parallel to each other but rotated with respect to the MOF crystals. Randomly oriented chromophores or those in which the emission transition moment is randomly oriented will have an anisotropy of zero. For the np-P4VB MOF viewed edge on, the anisotropy measured as described above ranged between 0.7 and 0.8, where $A = \frac{I_{\parallel} - I_{\perp}}{I_{\parallel} + 2I_{\perp}}$ and the symbols represent the fluorescence intensities measured parallel and perpendicular to the platelet surface normal, respectively. Fluorescence emitted in a direction parallel to the platelet surface normal, however, showed little evidence of polarization (A = $\sim$ 0). Thus, the polarization anisotropy strongly favors the direction of the conjugated backbone of the np-P4VB

in the crystalline MOF structure illustrated in Fig. 3.5, yielding a highly polarized luminescence parallel to the platelet normal.

To demonstrate the fluorescence color-changing ability, the MOFs were then exposed to HCl vapors to protonate them. A droplet of 12 M HCl was placed 5 mm from the location of the MOFs and the protonation-induced fluorescence change was observed over a period of several minutes. In some experiments, the MOFs were fumed by holding them over a beaker of HCl. While no differences were observed in the overall MOF shapes or structures after fuming (Fig. 3.6a,e), the initially yellowish fluorescent platelets changed to reddish orange (Fig. 3.6b,f). Throughout this process, the polarization anisotropy remained statistically unchanged (Fig. 3.6d,h) in the range of 0.7-0.8, within the variations from different individual grains and viewing angles with respect to the platelet normal.

The strong polarization anisotropy arises because the MOF structure enforces a high degree of orientation on the linear np-P4VB scaffold molecules. The anisotropy is one of the highest seen so far [156] due to the consistent alignment of the structural np-P4VB scaffold, which appears to remain intact throughout the interaction with HCl fumes. This shows that the selection of a ligand with a linearly conjugated backbone and a MOF structure that enforces a consistent ligand orientation, combined with possible waveguide polarization effects within each thin MOF platelet, can lead to a nearly complete luminescence polarization, which, in this case, can even survive the protonation reaction and associated color change.

The location of the H^+ and the corresponding counterion in the protonated MOF structure can be speculated on the basis of the absorption of HCl via the formation of carboxylato-chlorozincate clusters [157] with simultaneous protonation of pyridine units of the np-P4VB ligand. The latter can remain in proximity to the zinc clusters via hydrogen bonding to the carboxylate group, which would maintain the overall highly aligned network similar

to those observed in protonated amino acids [158] and also paddle wheel Zn-carboxylate structures with axially coordinated chloride ligands [159]. The presence of chloride within the HCl-fumed MOF crystals was clearly evidenced by energy-disperse X-ray (EDX) analysis (Fig. A.4), though the quantification, e.g., of Zn/Cl ratio is not possible due to the lack of a suitable standard. Protonated crystals exhibit a PXRD pattern similar to the solvent-free dried MOF for which the reflections due to ZnTDC layers were predominantly detectable (Fig. A.5). This suggests a light loss of structural order upon protonation.

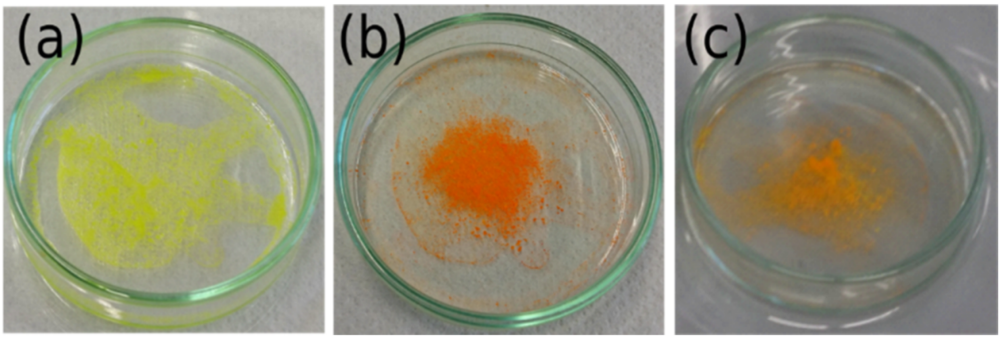

Figure 3.7: (a) As-synthesized TDC-MOF-8; (b) after fuming with HCl vapors for several minutes; and (c) after subsequent exposure to concentrated NaOH for 24 h without direct contact. The initially yellow MOFs turn orange (with a corresponding change in the PL spectrum); after exposure to NaOH, they appeared to at least partly deprotonate, leading to a yellow-orange color. Reprinted with permission from Chem. Mater. 2019, 31, 15, 5816–5823. Copyright 2019 American Chemical Society.

The MOFs could be induced to switch back at least partly to their original color by exposure to concentrated NaOH (Fig. 3.7). This suggests that at least some of the H^+ and its counterion are not very strongly bound into the MOF structure. However, even after several days, we did not observe a complete reversal to the original green-yellow color, whereas the original transition from yellow to reddish takes only a few minutes. Thus, while the MOF switches readily toward longer wavelengths, the removal of the acid is difficult and only a partial reversal could be observed. The rate and degree of

color changes were frequently observed to be faster in the case of the smallest MOFs (Fig. A.6), suggesting that better reversibility can be obtained by controlling the size of the MOF platelets.

We further tested the color change under exposure to fumes of trifluoroacetic acid and acetic acid, which have fairly different counterion sizes. No consistent differences were observed in response to these different acids that could not be explained as a result of their different acidity. While these acids do have quite different sizes as compared to HCl, they all remain significantly smaller than the interplanar spacing of the MOFs (Fig. 3.5). With such a large spacing, there is limited ability to select different acids within the size range of the three investigated acid counterions. Contact with liquid acid or solution, however, caused the MOFs to change color instantly and caused an obvious loss of structural integrity.

The photophysics of the MOFs was further investigated by measuring their luminescence lifetimes. The luminescence lifetimes of the MOFs were found to be slightly shorter than those of equivalent pure solvents (e.g., by comparing the Zn/ MOFs in DMF with the pure dye in DMF with dissolved Zn^{2+}; Table 3.1). This result is likely due to FRET-related carrier migration and recombination at surface-related defects. While the Zn-MOFs developed here are much larger than those for which similar lifetime decreases were reported[160], the individual wafers from which the platelets are constructed are submicrometer in scale, as observed by ion microscopy (Fig. A.7). Thus, carriers are likely to meet interfacial defects after traveling relatively short distances compared to the size of the whole platelets, consistent with the shorter observed luminescence lifetimes.

This TDC-MOF demonstrates color switching, compared to a recent study in which only a quenching effect was reported and suggested as a possible MOF-based pH-sensing mechanism [141]. The ability to generate at least partly reversible fluorescence switching is considered more desirable

for fluorescence-based sensing applications [117], since the dual-channel measurement leads to lower signal-to-noise ratios and an improved sensitivity. Furthermore, the dominant emission into one polarization can improve the performance of hybrid fluorescent systems for light emission, sensing, or lasing applications. Presumably, the formation of different coordination frameworks, for example, using different metal cations, might permit the creation of MOFs whose fluorescence color could be "dialed in" for any specific application.

3.4 Conclusions

We developed a simple organic chromophore that shows a striking fluorescence response to changes in the chemical environment. Its solvatochromic shift results in tunable luminescence through the blue and teal parts of the spectrum. Interaction with the surrounding ions causes even stronger changes, resulting in green or red luminescence. The strong luminescence color control arises from ion binding at the nitrogen sites, which tunes the degree of charge delocalization through the conjugated backbone of the molecular structure. Given the excellent fluorescent properties such as a high quantum yield, good photostability, and relative lack of intermolecular interactions due to large side chains, np-P4VB is a candidate fluorescent scaffold in metal-organic frameworks with extensively controllable fluorescence properties. In this work, we developed a zinc-based paddle wheel MOF that forms well-defined platelets in which the molecular framework enforces the alignment of np-P4VB along the principle axis. The resulting luminescence was highly polarized while also demonstrating a strong color-changing ability. The stacked MOF platelets shifted from a greenish-yellow to a red-orange fluorescence upon exposure to HCl fumes, without any visible degradation of the platelet structure, and could at least partly recover the original spectrum. This work demonstrates a fluorescent MOF that preserves a high degree of polarization anisotropy and color-switching ability, suggesting possible hybrid material routes toward robust experimental control over the light emission properties.

Chapter 4

An Ultrasensitive Fluorescent Paper-Based CO_2 Sensor

4.1 Introduction

Measurement of carbon dioxide (CO_2) is important in environmental, agricultural, biological, food, and medical industries[161]–[164]. CO_2 is also a greenhouse gas and is thought to be an important factor in climate change. It is used industrially for agricultural pest control and for experimental plant growth [165]. CO_2 is mixed with oxygen to form an inhalable gas for medical uses, is widely used in carbonated drinks [164], [166], and can be used to increase subsurface oil recovery [167]. Continuous CO_2 gas sensing is thus often required in order to ensure compliance with environmental standards, monitor safe levels for workers, determine smart building occupancy, and perform laboratory measurements [168].

Current CO_2 sensors are based on infrared absorption or electrochemical interactions that measure resistance or current[164], [169]–[180]. Sensors that use infrared absorption spectroscopy can be exceptionally sensitive, with detection limits well into the parts-per-billion range, but they cost tens of thousands of dollars. Electrochemical sensors are much less expensive (typically $100-300) but they typically suffer from a high cross sensitivity to other gases, have poor temperature stability, and the limit of detection is on the order of thousands of ppm [164], [181]–[183]. Compared to these types

of CO_2 sensors, fluorescence-based CO_2 sensors are potentially attractive because of their potentially simple construction, but their ultimate detection limits and chemical stability remain problematic [184], [185].

Paper-based sensors are attractive because of their versatility and low cost. Microfluidic paper-based devices are under widespread investigation for many biomedical applications, and paper sensors have been proposed for glucose monitoring, protein detection, and nerve-agent detection [186]–[188]. One previous paper-based CO_2 sensor was reported but it required colorimetric analysis of up to four dyes and was only demonstrated for solution-based sensing [189], as opposed to operating in the gas phase which is key for most of the aforementioned applications. To the best of our knowledge, only one previous paper-based CO_2 gas sensor has been demonstrated [190], but no detection limits were reported

Fluorescence-based sensors can use one of several techniques for CO_2 sensing (Table 4.1). One method is to sense carbonic acid (H_2CO_3) formed from the reaction between CO_2 and water. In this strategy, carbonic acid reacts with pH-sensitive fluorescent dye causing a change in the fluorescence intensity or color [184]. Another method uses the reaction between CO_2 and an amine group in a dye to form a carbamate, which quenches or shifts the fluorescence spectrum [191]. Alternatively, the amine group can first be deprotonated by reaction with an anion (e.g., F^-) in solution. The deprotonated amine group can then react with CO_2, thus activating a change in the emission [192], [193].

The limit of detection (LoD) for fluorescence sensors based on amine reactions range widely in the literature, with calculated or extrapolated values much lower than experimental ones (Table 4.1). Some calculated LoDs can be extremely low for chemical sensors (i.e., several tens of ppm); however, these sensors show poor or negligible reversibility and have long recovery times or no recovery at all, and are thus a one-use application (e.g., as absorbants)

[192]. In comparison, carbonic acid methods can be reversible and show fast response and recovery times [194]. This is especially desirable for multi-use applications, but this method appears to suffer from a comparatively poor LoD. The aim of this work is to show a reversible color-shift fluorescent gas sensor with a low LoD and reversibility on a convenient paper-based platform.

Table 4.1: Comparison of Fluorescence-Based Optical CO_2 Sensors (The numbers inside the parentheses are the lowest concentration detected experimentally; without the parentheses indicates an extrapolated LoD.). Reprinted with permission from ACS Appl. Mater. Interfaces 2020, 12, 18, 20507–20513. Copyright 2020 American Chemical Society.

Method	Sensing signal	LoD (%)	Response time (s)	Recovery time (s)	Ref.
amine	intensity	0.0026(0.1)			[195]
amine	color	0.04			[196]
anion activated	intensity	0.003(0.004)			[175]
anion activated	color	0.0038(6.4)			[192]
carbonic acid	intensity	(0.038)	"fast"		[197]
carbonic acid	intensity	(0.04)			[198]
carbonic acid	intensity	(2.5)			[199]
carbonic acid	intensity	0.11(1)	10	180	[177]
carbonic acid	color	0.25(0.25)	30	60	[184]
carbonic acid	color	2.3(7.7)	5	5	[200]
carbonic acid	color	0.6(0.6)	30	60	[184]

In order to achieve this, we capitalize on the reversible protonation reaction that takes place in bis(4-pyridyl)dineopentoxyl-p-phenylenedivinylene (np-P4VB: Fig. 4.1), a chromophore that we recently designed for its exceptional stability and fluorescence color-shift properties [119]. The molecular backbone has been synthesized a few times recently in the literature but generally with short-chain sidegroups (i.e., methoxy groups) [201]–[203]. When the highly-accessible nitrogen atoms on the two terminal pyridine rings of np-P4VB are protonated, a fluorescence shift from teal to orange results from the extensive electron delocalization in the lowest unoccupied molecular orbital [204]. Smaller but distinct fluorescence shifts occur as a result of pos-

itive solvatochromism (a redshift upon exposure to solvents of higher polarity).

Here, we will show that np-P4VB can be developed as a sensitive paper-based fluorescent CO_2 gas sensor. The LoD is the lowest observed for a sensor of this type, while showing full reversibility and a relatively fast response time in a simple paper-based sensor format. Furthermore, the ratiometric method employed by this color-shift chromophore permits almost complete cancellation of the effects of bleaching, power fluctuations, or other extraneous variations in the sensor signal.

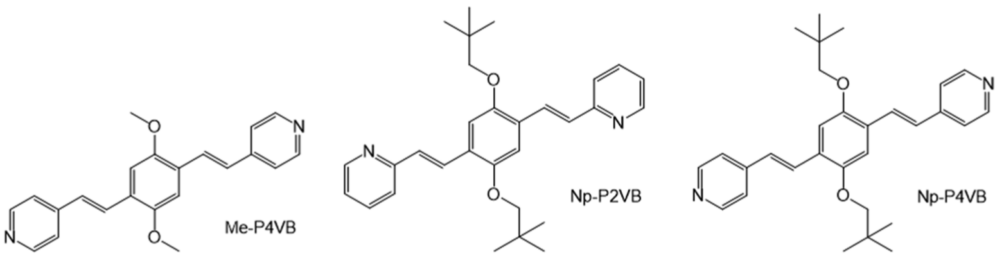

Figure 4.1: Stick diagrams illustrating the molecular structures of me-P4VB, np-P2VB, and np-P4VB. Reprinted with permission from ACS Appl. Mater. Interfaces 2020, 12, 18, 20507–20513. Copyright 2020 American Chemical Society.

4.2 Experimental section

The synthesis, identification, and characterization of np-P4VB with neopentyl side groups was described by us in detail previously [119]. The neopentyl groups serve as bulky protective "barriers" against intermolecular interactions which can otherwise lead to extensive luminescence quenching in similar molecules [119]. When dried from solution, the resulting crystals form aggregations of thin yellow fibers with a strong green fluorescence (Fig. B.1). In solution, the quantum efficiency is up to 80%.

To compare performance and shed light on the mechanisms, we synthesized two related molecules. 2,5-dineopentoxy-1,4-bis[2-(2-pyridyl)ethenyl]benzene

(np-P2VB) was synthesized following the same protocol as for np-P4VB except that pyridine-2-carboxaldehyde was used in the last step instead of pyridine-4-carboxaldehyde. Synthesis of 2,5-dimethoxy-1,4-bis[2-(4-pyridyl)ethenyl]benzene (me-P4VB) was performed according to literature procedure [205]. The structures were verified by NMR (Fig. B.2, B.3) and are represented in Fig. 4.1.

The paper-based sensors were fabricated by dipping a piece of Fisher brand P4 grade filter paper into a solution of 0.2 mM np-P4VB in ethanol. The solvent was then allowed to evaporate over a period of several minutes, leaving the np-P4VB dispersed in the cellulose fibers of the paper. The CO_2 gas sensing apparatus was constructed from quarter inch tubing and two flow controllers (Fig. 4.2). Nitrogen (99.998% purity) was used as the carrier gas and the other line contained a CO_2 + N_2 test gas mixture (either 100 ppm or 1% pre-mixed with balance nitrogen). The CO_2 concentration was controlled by changing the flow rate of the two gases, which were varied from 0 to 5 NL/h in different experiments. Mixed gas was delivered into a flask containing water at 40^oC in order to deliver sufficient water vapor to the gas flow. For some experiments the standardized CO_2 line was replaced with room air (410 ppm CO_2) or human breath (nominally 4-5% CO_2) in order to test the sensor response under more complicated gas mixtures.

The resulting gases were then allowed to flow directly through the paper sensor, while its fluorescence was measured in real time. The fluorescence was excited with a 365 nm LED (Prizmatix) and was collected by a standard 1 mm optical fiber (numerical aperture = 0.5). The fluorescence was analyzed with an intensity-calibrated Ocean Optics USB2000+ spectrometer. The system saved the spectrum automatically every 5 seconds as the gas flows were adjusted to deliver CO_2 or to purge the sensor, in order to generate sensorgrams. A set of blanks was also run in order to confirm the sensing mechanism, as described further below.

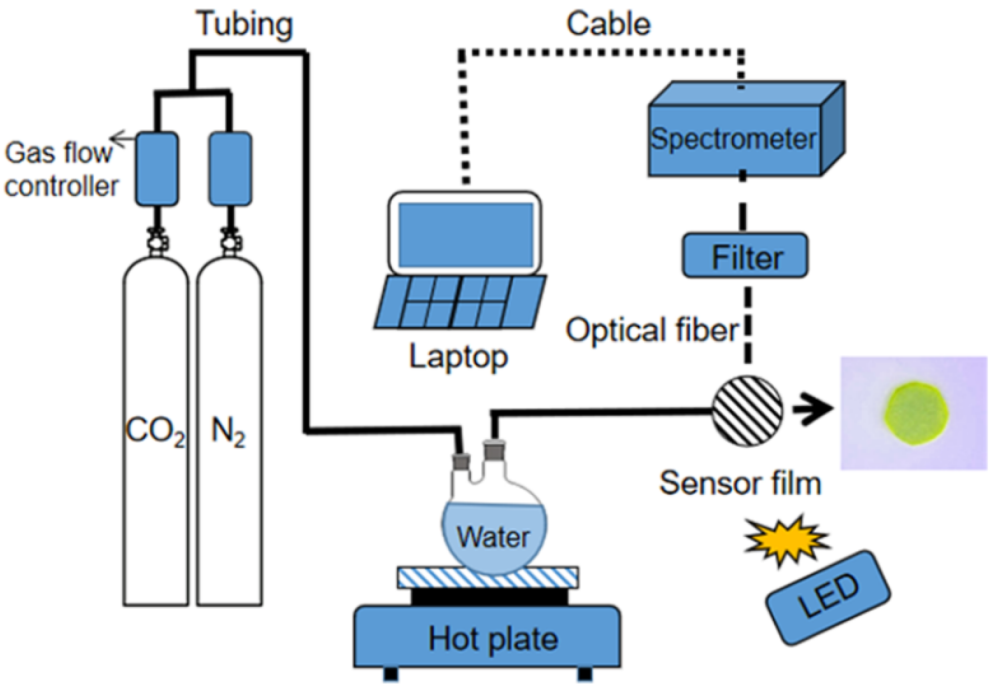

Figure 4.2: Schematic of the experimental setup. CO_2 mixed with N_2 as a carrier gas was passed over a warm water bath (40^oC), and then flowed through fluorescent paper. A 365-nm LED illuminated the sample, and a fiber was used to collect the fluorescence, which was analyzed in real time by a miniature spectrometer. Reprinted with permission from ACS Appl. Mater. Interfaces 2020, 12, 18, 20507–20513. Copyright 2020 American Chemical Society.

4.3 Results and discussion

The fluorescence spectrum of the as-formed solid crystals of np-P4VB peaked at 520 nm, but after being dissolved in ethanol the emission peaked at 475 nm (Fig. 4.3a), appearing a bright teal to the eye. After being infused in filter paper and allowed to dry, the emission changed in color from teal to yellow-green as the peak emission shifted from 475 to 550 nm. The fluorescence of the dried filter paper tended to gradually photobleach over a period of several minutes, whereas little-to-no bleaching was observed in the original solution. This is likely a result of the formation of singlet oxygen or long-lived triplet states that can diffuse out of the excitation spot in the solution phase but cannot do so when dried in the filter paper.

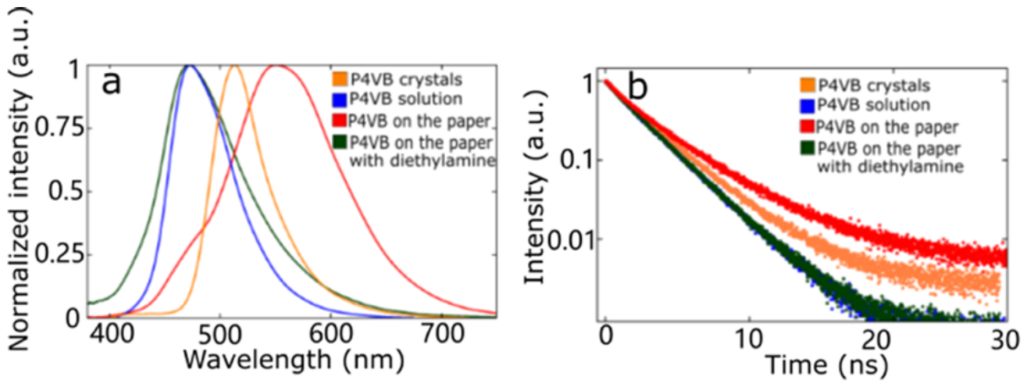

Figure 4.3: (a) PL spectra of the P4VB in crystals, ethanol solution, and on base-blocked and unblocked paper. (b) Fluorescence lifetimes for the same set of samples. Reprinted with permission from ACS Appl. Mater. Interfaces 2020, 12, 18, 20507–20513. Copyright 2020 American Chemical Society.

The pronounced long-wavelength shift that occurred upon drying the dye in the paper suggests that the paper itself is slightly acidic. While cellulose (the main constituent of paper) is nominally non-acidic, many acidic impurities are known to occur during paper fabrication and even to accumulate over time (i.e., lignin and hemicellulose produce slightly acidic degradation byproducts in paper). These would result in a redshift of the fluorescence, here observed from teal to yellow, via a partial protonation of the dye. In order to verify this hypothesis, the paper was first dipped in diethylamine, a rather strong and volatile organic base, in order to block the acidic components of the paper. After drying, the same infusion procedure as above was followed with the np-P4VB. In this case, the fluorescence remained teal and no spectral shift was observed between the starting solution and the dried filter paper.

The fluorescence lifetimes showed a single exponential decay in all cases, varying from 2.3 and 2.4 ns for the teal emission (in solution or on the diethylamine-blocked paper) up to 2.6 ns for the solid np-P4VB crystals and 2.9 ns when the chromophore was dried on filter paper without the blocking solution (Fig. 4.3b). Thus, we observe a consistent monotonic increase in the fluorescence lifetime as the peak of the PL spectrum shifts from teal through yellow in color.

In order to verify the ability of the fluorescent paper to act as a pH sensor, we first exposed it to acid vapors over a beaker of strong HCl (12 M). The initially teal fluorescence quickly changed over several seconds, gradually becoming orange (Fig. 4.4). This shows that the chromophore remains highly sensitive to protonation even when dispersed in the cellulose fibers. The color change is also consistent with that occurring after exposure of the np-P4VB crystals to acid vapors, which also turned the fluorescence from green to orange over a period of less than a minute (Fig. B.1).

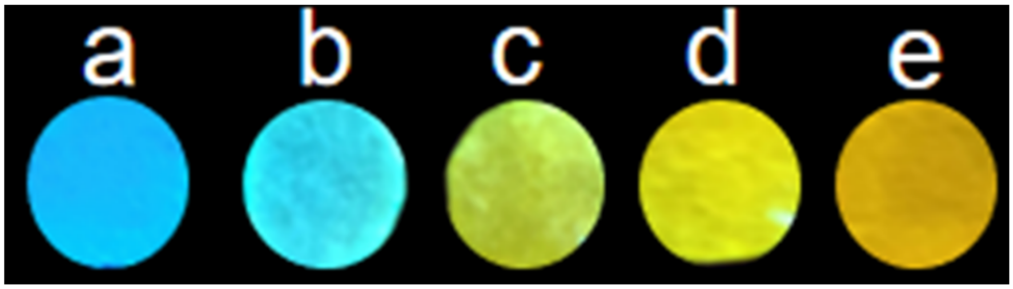

Figure 4.4: Photographs of np-P4VB-infused paper taken under a black light. Images (a and b) are the dye-infused paper (a) with and (b) without pre-treatment with diethylamine. Photos (c-e) show the color evolution starting from (b) exposure to the acid vapor from 12 M HCl for 5, 10, and 20 s, respectively. The color shifts from green to orange. The images were taken with a OnePlus 7 Pro cellphone camera and are reasonable approximations to the observed colors, although (b) appears significantly greener and (e) appears slightly redder to the naked eye than they do in the image. Reprinted with permission from ACS Appl. Mater. Interfaces 2020, 12, 18, 20507–20513. Copyright 2020 American Chemical Society.

The main problem with protonation-induced fluorescence color shifting by weak acids is that a high acid concentration is required since completing the shift requires double-protonation of the dye molecules. However, we recently showed that positive solvatochromic shifts also occur in this chromphore [119]. While the redshift is much less dramatic than it is for protonation, there is a consistent shift toward longer wavelengths as the static dielectric constant (or polarity index) of the solution increases. This shift could, in principle, be sensitive to small changes in acid concentration, not as a direct

result of protonation but rather because of a weaker perturbation of the LUMO-HOMO transition [204].

In order to clarify the sensor results, we first performed a set of blank runs. The first blank simply used filter paper (no dye). A weak whitish PL was observed and did not change upon exposure to the CO_2-H_2O-N_2 gas mixture. Next, a sample of np-P4VB-infused paper showing strong green-yellow fluorescence (550 nm) was exposed either to dry N_2 or to N_2 that was passed over the warm water. In these cases, no shift in the spectrum was found, although photobleaching did occur as usual (Fig. B.4). Dry CO_2 was also attempted, with no resulting spectral shift. In comparison, when CO_2 was added to N_2 and flowed over the warm water bath, a clear redshift was observed whose magnitude varied monotonically with CO_2 concentration (Fig. 4.5a).

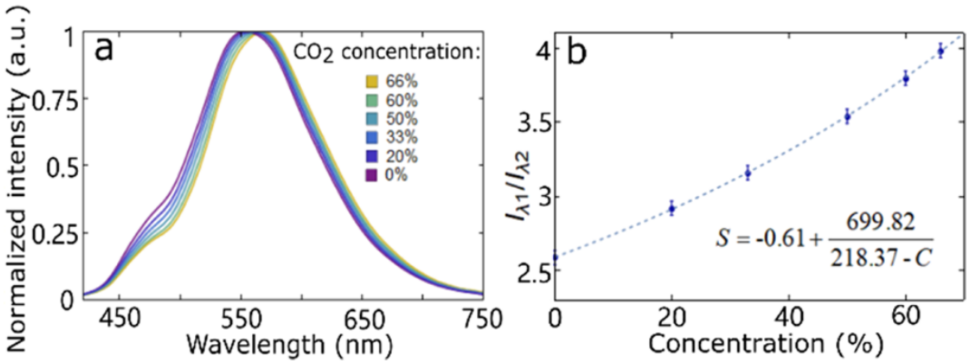

Figure 4.5: (a) Normalized photoluminescence spectra of filter paper infused with np-P4VB upon exposure for 5 min to different CO_2 levels ranging from 0 to 66%. (b) Ratiometric wavelength shift as a function of CO_2 concentration. The dashed line curve is a best fit from $S = a_1 + a_2/(a_3 + C)$. The error bars represent 3σ of the standard deviation of three measurements on the same sample at a CO_2 concentration of 20%. The error measurements were taken by finding the saturation shift level, then regenerating the sensor paper as described in the sensorgram measurements and repeating the CO_2 exposure. Reprinted with permission from ACS Appl. Mater. Interfaces 2020, 12, 18, 20507–20513. Copyright 2020 American Chemical Society.

While the mechanisms for the color shift are difficult to determine

unambiguously from these experiments, several conclusions can nevertheless be drawn. First, we observe that CO_2 and water vapor are needed to obtain the luminescence spectral shift. Since the carrier gases were gently passed over a still warm water bath, there are unlikely to be any water droplets carried to the sensor. There is probably condensation of the water vapor within the paper, thus wetting it and providing a medium for dissolving CO_2 and the formation of carbonic acid, which is then sensed by the np-P4VB via interactions with the weakly basic pyridine groups. Based on the small color shift, there appears not to be a proton transfer occurring, rather only a weakly bound associate of np-P4VB and carbonic acid, which perturbs the HOMO-LUMO gap and causes a small but clear redshift in the emission spectrum. These ideas are consistent with NMR results on samples pressurized under CO_2 and exposed to acid (Fig. B.5 and B.6) and with detailed UV-vis absorption spectroscopy (Fig. B.7).

In order to verify these ideas, two variations of the chromophore were synthesized and tested (see Experimental Section). np-P2VB has the same molecular backbone and sidegroups, but the pyridine nitrogen atoms are on the pyridine 2 position and thus should be less sterically accessible. me-P4VB has smaller, shorter sidegroups and is expected to show an increased degree of intermolecular interaction. Indeed, the acid response for np-P2VB was quite poor compared to that of np-P4VB (Fig. B.8), consistent with the hypothesis that the position of the nitrogen in the pyridine rings is key to sensor performance. me-P4VB showed broadly similar performance as that of np-P4VB but showed limited solubility in ethanol solutions, consistent with the deleterious effects of increased molecular interactions with the shorter sidegroups. The sensing performance was also tested and showed precisely analogous behavior (i.e., good performance for P4VB and poor to negligible performance for P2VB; Fig. B.9).

To quantify the luminescent spectral shift and eliminate the effects of

bleaching, a ratiometric approach was employed, in which the signal $S = \frac{I_{\lambda_1}}{I_{\lambda_2}}$ with λ_1= 570 nm and λ_2 =481 nm. These wavelengths show relatively large intensity changes upon exposure to the test gas. The experimental values for S varied monotonically as a function of CO_2 gas concentration ranging from 0 to 66% (Fig. 4.5b). The observed shift was linear for each of the two wavelengths, so that dividing the two linear relationships yields S = $a_1 + a_2/(a_3 + C)$, where a_1, a_2, and a_3 are fitting parameters and C is the concentration. The relationship between the sensor response, S, and CO_2 concentration is clearly monotonic (Fig. 4.5b) and in agreement with the simple model.

To find the LoD, one needs an estimate of the sensitivity and the noise level. In order to estimate the noise, the standard deviation of the signal S was taken from 130 points under unchanging conditions. The sensitivity, m, was estimated conservatively at the low-concentration region where the slope in Fig. 4.5b is the smallest. With this method, we find that the LoD = 3σ/m = 250 ppm.

The LoD is among the lowest for carbonic-acid-based sensing schemes and is as good as those obtained for many non-reversible reactions (Table 4.1). In order to verify this performance, real-time sensorgram measurements were performed as the CO_2 was injected periodically at different concentrations. For a 1% CO_2 mixture, the response was clear and repeatable (Fig. 4.6), with a characteristic rise time of 100 seconds to reach the maximum signal. Upon stopping the CO_2 flow and switching the N_2 over the warm water, the fluorescence shifted back to its original value after $\sim$ 45 seconds. Thus, the sensor is regenerated after each exposure due to exchange of the gases or removal of the condensate within the paper.

Further tests were conducted with 0.1% and 0.01% CO_2 in N_2 gas mixtures. The signal strength is likely related to the equilibrium concentration of carbonic acid present in the paper. While the strength of the signal decreases

for these low concentrations, even at 100 ppm (0.01%) the signal is clear and repeatable (Fig. 4.6a, inset), although at this scale, it does appear on top of a slightly changing background. Lower flow rates were used for the lower concentrations, which resulted in a longer regeneration time as shown in Fig. 4.6 as confirmed by varying the flow rates for the same concentration (Fig. B.10). The magnitude of the final signal was only modestly affected by the flow rate, however.

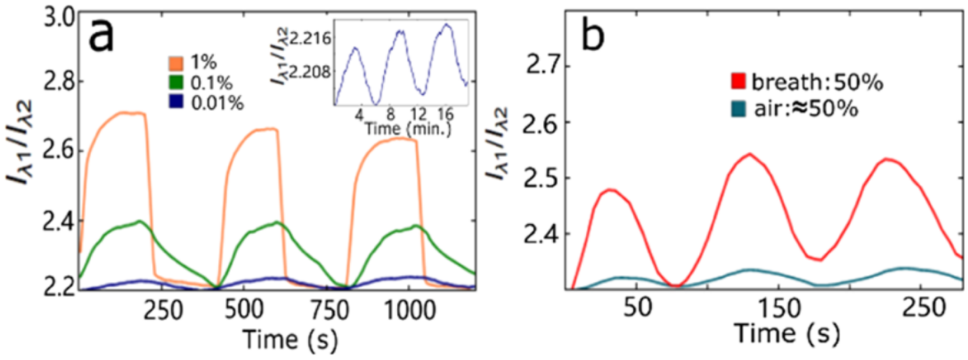

Figure 4.6: (a) Sensorgram response of the np-P4VB-infused paper, which was exposed to different concentrations of CO_2 (1% for the orange line, 0.1% for the green line, and 0.01% for the blue line). The spectra showed an obvious wavelength shift under CO_2 and changed back when the CO_2 flow was changed to pure N_2. (b) Response of the CO_2 sensor recurrently exposed to atmospheric air (blue line) or human breath (red line). Reprinted with permission from ACS Appl. Mater. Interfaces 2020, 12, 18, 20507–20513. Copyright 2020 American Chemical Society.

In order to verify how well the CO_2 sensor works in more complicated gas mixtures, it was tested with human breath and with atmospheric air. Human breath consists of a mixture of CO_2 (5% depending on the individual), water vapor (5%), N_2 (74%), O_2 (15%), and a mixture of trace gases and possibly some volatile organic compounds. A "breath test" was performed by having an experimenter breathe into a tube which was connected to another tube with flowing N_2 (2 NL/h). The breathing rate was controlled as well as reasonably possible for a roughly 50% dilution with the carrier gas.

As shown in Fig. 4.6b, the sensor responded clearly to human breath, with the signal appearing much the same as for the pure CO_2 measurements, although it was significantly smaller than expected for 2.5% CO_2. Two factors may contribute to the weaker-than-expected signal: first, it was difficult to ensure a consistent and accurate breathing rate into the tube (especially considering that the sensor response was 100 seconds at the flow rates used), and second, there could be interfering effects from many possible gases that might be present.

The sensor response to atmospheric air was also evaluated, where current background CO_2 levels are 410 ppm [206]. Compressed air was injected into the sensor apparatus at the same flow rate as the 99.998% N_2 carrier gas (2 NL/h), so that the effective CO_2 concentration delivered to the sensor was $\sim$ 205 ppm. The sensor responded repeatably to the atmospheric CO_2 level and the signal strength was in good agreement with those for the pure gas mixtures shown in Fig. 4.5.

The errors and repeatability of the paper-based sensors were next evaluated further. By using the signal stability of a single sensor under fixed conditions, the 3σ signal noise was 0.092%. Repeating the same measurements by regenerating the sensor yielded slightly larger errors. Comparing the results for the same CO_2 exposures with different samples yielded errors of 3%, especially if the measurements were taken at different times after the sample was prepared or using drop casting vs. dipping methods. These effects can be seen in Fig. 4.6, where the samples do not all start at precisely the same initial signal level. This suggests that either sample calibration is needed or that special care must be taken to quantify the effects of aging and exposure to atmospheric CO_2, water vapor, and other gases.

The experimental LoD appears nevertheless to be significantly smaller than the calculated one. From Fig. 4.6a, 100 ppm of CO_2 yields an experimental SNR of 53. If we assume that the LoD is determined by 3σ of the random noise

in Fig. 4.6b, the LoD becomes as low as 5.7 ppm assuming a linear response, which is in agreement with the model at low concentrations. Essentially, these data feature experimental detection of CO_2 at levels considerably lower than the extrapolated LoD from high-concentrations of CO_2 using variable mixed gas flow rates. This means that while exceptionally low concentrations of CO_2 are detectable by fluorescence, an absolute quantification at such low CO_2 levels would be difficult without further calibrations and age/responsivity studies. Additionally, there may be significant error in the mixed gas flow rates at this level, which contribute to the measured errors, although this is not related to the actual sensor performance.

Batch-to-batch variability was also tested by comparing the response of prepared paper sensors from different original boxes. This variation was found to be about 3%, which is similar to the errors shown in Fig. 4.5b from multiple regenerations from the same sample. Thus, we conclude that batch-to-batch variability is not a major concern for practical application, and the errors are essentially controlled by aging, oxidation, or currently uncontrolled variables in the sample preparation and gas handling.

Np-P4VB was designed to offer excellent fluorescence color shift sensor performance by having accessible pyridine groups on a protected but relatively short conjugated backbone. Outstanding CO_2 sensing performance can be achieved in a paper-based format into which the np-P4VB is infused and dried. Np-P4VB-infused paper shows a solvatochromic-like redshift of the PL spectrum upon exposure to CO_2-carrying gases. This was attributed to the complex environment around the np-P4VB molecules embedded in the paper, which evidently contains carbonic acid formed as different concentrations of CO_2 pass through the moist paper. The carbonic acid interacts with the basic pyridine groups in the np-PV4B, shifting the fluorescence and resulting in the measured sensor signal. These results present the lowest reported detection limits for a paper-based CO_2 gas sensor to date.

These results present the lowest reported detection limits for a paper-based CO_2 gas sensor to date. An additional advantage of this sensor is that the effects of photobleaching (see Fig. B.4), quenching, or LED power fluctuations were eliminated. The reason is that all of these effects were evidently of the same magnitude over the whole spectrum, and thus, the fluorescent ratiometric approach simply cancelled them out.

4.4 Conclusion

Np-P4VB-infused paper offers outstanding sensor performance in a simple and universal design. The ratiometric approach easily cancels simple problems such as photobleaching and excitation power variability. The sensor response time is on the order of 1 minute, which is comparable with other fluorescence-based sensors. It responds reliably to complex multi-component atmospheric gases, provided that no other acidic gases are present. Detection of 100 ppm was shown experimentally, with an extrapolated LoD of only 5.7 ppm. Hundreds of such paper sensors can easily be made from a single 1 mL stock solution and they require virtually no processing, lithography, or printing, thus rendering the sensor exceptionally simple and inexpensive to produce. Sensors of this type could find future applications in smart buildings or other locations requiring continuous background CO_2 monitoring, but care must be taken to minimize sensor aging under uncontrolled atmospheric conditions. Future improvements in the fabrication and testing processes would permit a more standard and uniform sample-to-sample response to be achieved.

Chapter 5

Ultrasensitive Picomolar Detection of Aqueous Acids in Microscale Fluorescent Droplets

5.1 Introduction

Ultrasensitive chemical sensing is expected to be of great importance in environmental [207], water safety [208], air quality [209], and biochemical applications [210]–[212]. For example, ultra-sensitive (i.e., sub-nanomolar) chemical sensors are being developed to detect tiny quantities of intracellular hydrogen ions which can present important early indications of disease [213]. The sensitive detection of acidic nitroaromatic compounds (i.e., picric acid) has been widely investigated for trace explosives sensing [214]. The detection of trace lactic acid is important for health and food safety [215]. Ultrasensitive detection of H_2S is needed for worker safety and for health applications including the detection of metabolic abnormalities associated with a variety of diseases [216]. These are just a few examples in which the sensitive detection of acidic compounds is of major consequence.

Because of the widespread importance and numerous applications associated with the sensing of $[H^+]$, a large number of acid sensors have been reported in recent years. Electrochemical sensors for various acids are based on current or resistance measurements and have extrapolated limits of detection (LoDs) mainly in the micromolar regime or slightly below [217], [218]

(see Table 5.1). Colorimetric sensing is based on optical absorption changes and has yielded calculated LoDs as low as 11.6 nM for enzyme immobilization and detection of okadaic acid [219]. Fluorescence sensing strategies appear to have some of the lowest calculated LoDs so far, with reports into the single nanomolar range [220]. Further decreasing the LoD has proven challenging, however, because of detector noise and low light levels or weak sensing signals [221].

Microdroplets have the potential to yield an ultra-low limit of detection for acid sensing [223].The idea is based around a partition of $[H^+]$ from the analyte into the microdroplet, which can, in principle, lead to a concentration enhancement that multiplies the detection signal. The partition coefficient is the ratio of the equilibrium concentrations of the analyte in two immiscible liquid systems, and it is widely applied for chemical extraction and analysis [237]. Colorimetric studies of liquid droplets recently showed that the droplet-based detection method is fast, requires small sample volumes, and yielded an experimental LoD of 0.1 mM [238]. The method developed in this work will preserve the first two advantages but decrease the LoD by more than six orders of magnitude. Obviously, more costly and time-consuming methods like mass spectroscopy [239] and surface-enhanced Raman scattering (including from microdroplets [240]) can provide chemical sensing down to the parts-per-billion range, but they require complex and expensive apparatus and are unsuitable for the detection of $[H^+]$ in solution.

The proposed method is based on a fluorescent color-change chromophore that we recently developed for wide-gamut lasing applications [119]. This chromophore has a simple 3-ring aromatic structure with terminal pyridine groups that are ideally situated for protonation. The fluorescence changes from blue to orange upon protonation, while maintaining a quantum efficiency in excess of 30%, allowing facile detection of protons via a ratiometric method as opposed to fluorescence quenching. This makes the detection scheme robust against photobleaching or fluctuations in the excitation source. By

Table 5.1: The LoDs, type, and methods of acid sensors reported. Reprinted with permission from ACS Sens. 2022, 7, 1, 245–252. Copyright 2021 American Chemical Society.

LoD	Type	Method	Citation
5.7 muM (lactic acid)	Calculated	Electrochemical	[222]
10^{-4} M (acetic acid)	Measured	Colorimetric	[223]
0.13 μmol/l (ascorbic acid)	Calculated	Fluorescence intensity	[224]
0.1 μM (folic acid)	Calculated	Electrochemical	[217]
0.1 μM (ascorbic acid, uric acid)	Calculated	Electrochemical	[218]
44 ppb (picric acid)	Calculated	Fluorimetric	[225]
1.6 μmol/l (uric acid)	Calculated	Fluorescent	[211]
10 μM (lithocholic acid)	Experimental	Optical transition	[226]
0.15 μM (ascorbic acid)	Calculated	Fluorescence	[227]
15.12 μ (ascorbic acid)	Calculated	Electrochemical	[221]
0.5 μM (ascorbic acid)	Calculated	Colorimetric	[228]
37 nM (hypochlorous acid)	Calculated	Ratiometric fluorescence	[229]
30.6 nM (hypobromous acid)	Calculated	Fluorescence	[230]
0.8 nM (picric acid)	Calculated	Fluorescence	[231]
1 nM (salicylic acid in living cell)	Calculated	Fluorescence	[220]
11.6 nM (okadaic acid)	Calculated	Colorimetric	[219]
0.093 μM (picric acid)	Calculated	Fluorescence	[232]
10 nM (ascorbic acid)	Calculated	Fluorescence	[233]
0.1 μM (uric acid)	Calculated	Electrochemical	[234]
5.8 μM (folic acid)	Calculated	Fluorescence	[235]
5 μM (ascorbic acid)	Calculated	Fluorescence	[236]

combining these key advantages with a "super-enhancement" via partitioning into microdroplets, we will demonstrate a simple, robust, and extremely sensitive [H^+] sensor with a limit of detection well into the picomolar regime.

5.2 Experimental

5.2.1 Synthesis of np-P4VB

The synthesis and molecular characterization of the conjugated organic chromophore [bis(4-pyridyl)dineopentoxyl-p-phenyl-enedivinylene (np-P4VB)] followed the method we described in detail in Ref. [119]. This synthesis resulted in several hundred mg of np-P4VB, which appears as a fluorescent yellow powder. The as-synthesized np-P4VB was used directly for the formation of fluorescent octanol microdroplets.

5.2.2 Preparation of fluorescent microdroplets

The solution used to form the fluorescent droplets (solution A) follows established solvent-exchange methods [241], [242] but in this case it employed a mixture of octanol, ethanol, and water at a volume ratio of 3:50:50 with either 0.23 mM or 0.023 mM np-P4VB dissolved into the mixture. The ethanol works as the co-solvent for the otherwise largely immiscible water-octanol combination. Solution A was then injected into the fluid analysis chamber as the first step. The chamber consisted of a hydrophobic silicon wafer functionalized with 95% octadecyl-trichlorosilane [243] (Acros Organic, USA) affixed to the bottom of a solvent exchange chamber with a glass viewing window (Fig. 5.1). Then octanol-saturated water from a Milli-Q water purification system (saturation obtained by shaking the water-octanol solution periodically over four days and extracting the water with a syringe; solution B) was injected to replace solution A. At the mixing front between solution A and solution B, there is an octanol oversaturation leading to the nucleation of octanol droplets on the chamber surface. The saturation limit for octanol

in water is 0.3 g/L at room temperature so solution B was first saturated with octanol to avoid the dissolution of the octanol droplets. The np-P4VB is expected to partition preferentially into the droplets because it has a higher saturated concentration in octanol as compared to ethanol, and it is insoluble in water. Thus, the concentration of the dye in droplets is based on the partition between bulk Solution A phase and octanol droplets (Solution B).

Solution A was first pumped into the chamber until it was full, and then solution B was pumped in, leaving small fluorescent droplets of solution A scattered over the silicon substrate. Finally, solution C (the analyte) was pumped into the chamber at a rate of 15 mL/h. Solution C is the analyte, composed of salicylic acid (IUPAC name: 2-hydrobenzoic acid) dissolved at various concentrations in milli-Q water saturated with octanol.

5.2.3 Final preparation and sensing measurements

The droplet fluorescence was monitored on a Nikon TE2000e inverted epifluorescence microscope using a 405-nm LED as the excitation source and a Sony model α6400 digital camera to record color images. Analysis of the images was done using an open-source image-processing software (ImageJ [244]).

5.3 Results and discussion

5.3.1 Calibration

We first needed to calibrate the fluorescence response of np-P4VB as a function of its concentration in octanol (Fig. 5.2). This calibration permits an independent measurement of the unknown np-P4VB concentration that partitions into the octanol phase. Fig. 5.2a shows a blacklight photograph of several vials of octanol with np-P4VB concentrations ranging from 2.3 mM to 11.5 mM. With increasing dye concentration, the solution turns from pale

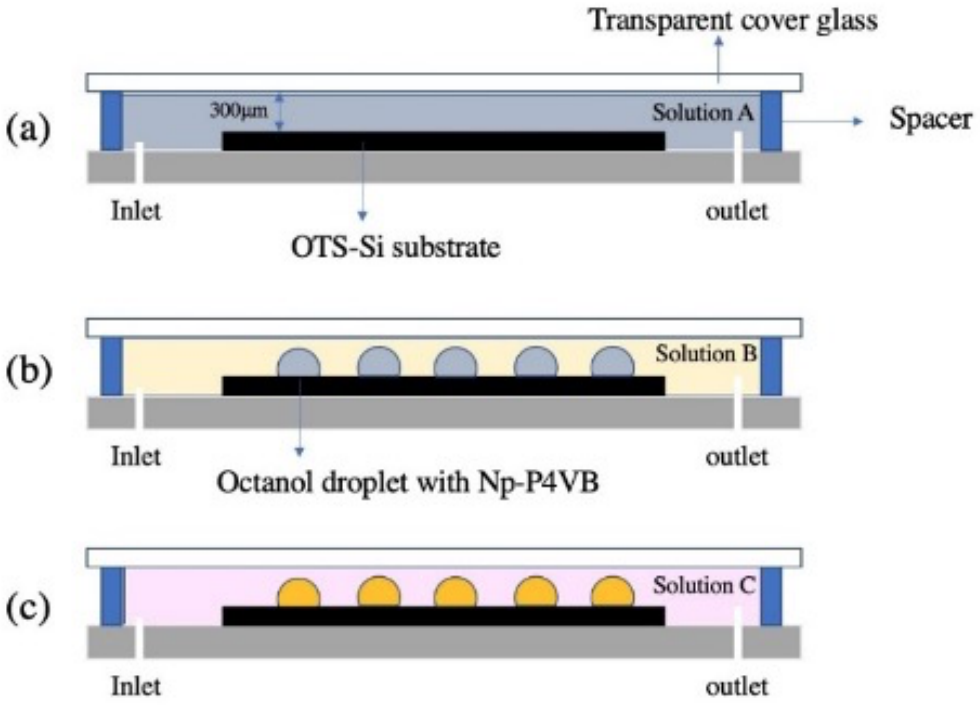

Figure 5.1: Schematic of the experimental procedure. (a) Analysis chamber containing solution A with the functionalized silicon substrate (black). (b) After solution B is pumped into the chamber, the fluorescent droplets form on the substrate. (c) After solution C is pumped into the chamber, the analyte in the solution is extracted into the droplets which accordingly change their fluorescence spectrum. Reprinted with permission from ACS Sens. 2022, 7, 1, 245–252. Copyright 2021 American Chemical Society.

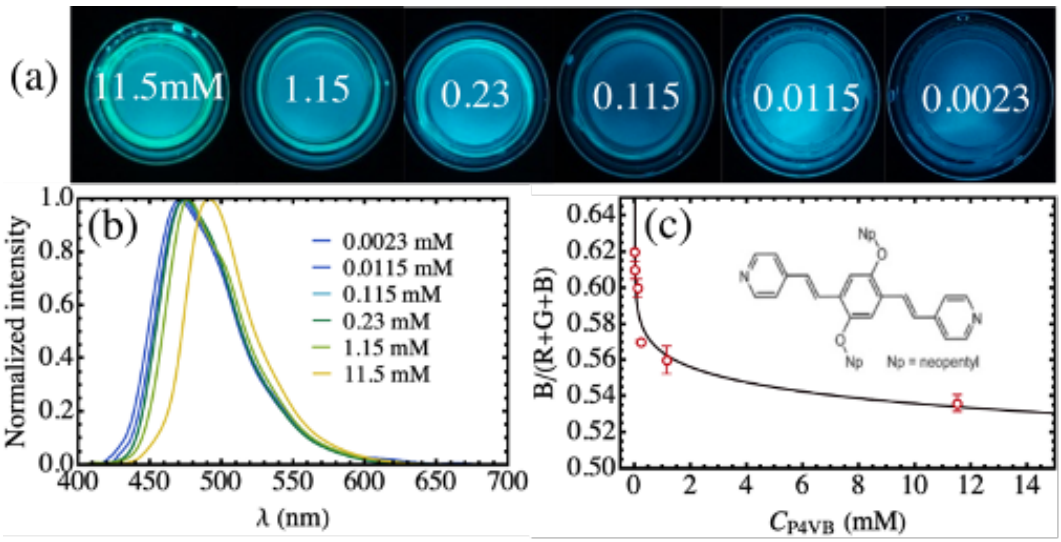

Figure 5.2: (a) Photograph of several vials of np-P4VB illuminated under a blacklight, at concentrations ranging from 0.0023 to 11.5 mM. (b) The corresponding photoluminescence spectra; (c) The measured signal, S, along with the fit calibration curve (a). A model of the np-P4VB molecular structure is shown in the inset. The errors were obtained as described in the Appendix C. Reprinted with permission from ACS Sens. 2022, 7, 1, 245–252. Copyright 2021 American Chemical Society.

blue to an emerald green (the corresponding fluorescence spectra shown in Fig. 5.2b). The droplets were imaged from the same direction as the light source (the top) in order to minimize inner filter effects which can change the apparent emission color by self absorption. We then constructed a dye concentration calibration curve by fitting the data to a power law given by S=aC^b_{P4VB}+c where a, b, and c are fitting parameters and C_{P4VB} is the dye concentration. The signal S is represented by R/(R+G+B) where R, G, and B are the pixel intensities in the red, green, and blue image channels, respectively (see the Appendix C for how the pixels were selected and averaged, and for a description of the errors). The model fits the data well with a = -0.18, b = 0.06, and c = 0.75 (Fig. 5.2c), allowing unknown np-P4VB concentrations to be found by analyzing the fluorescence color of the as-prepared octanol droplets.

When salicylic acid is added to the octanol, the np-P4VB dye turns

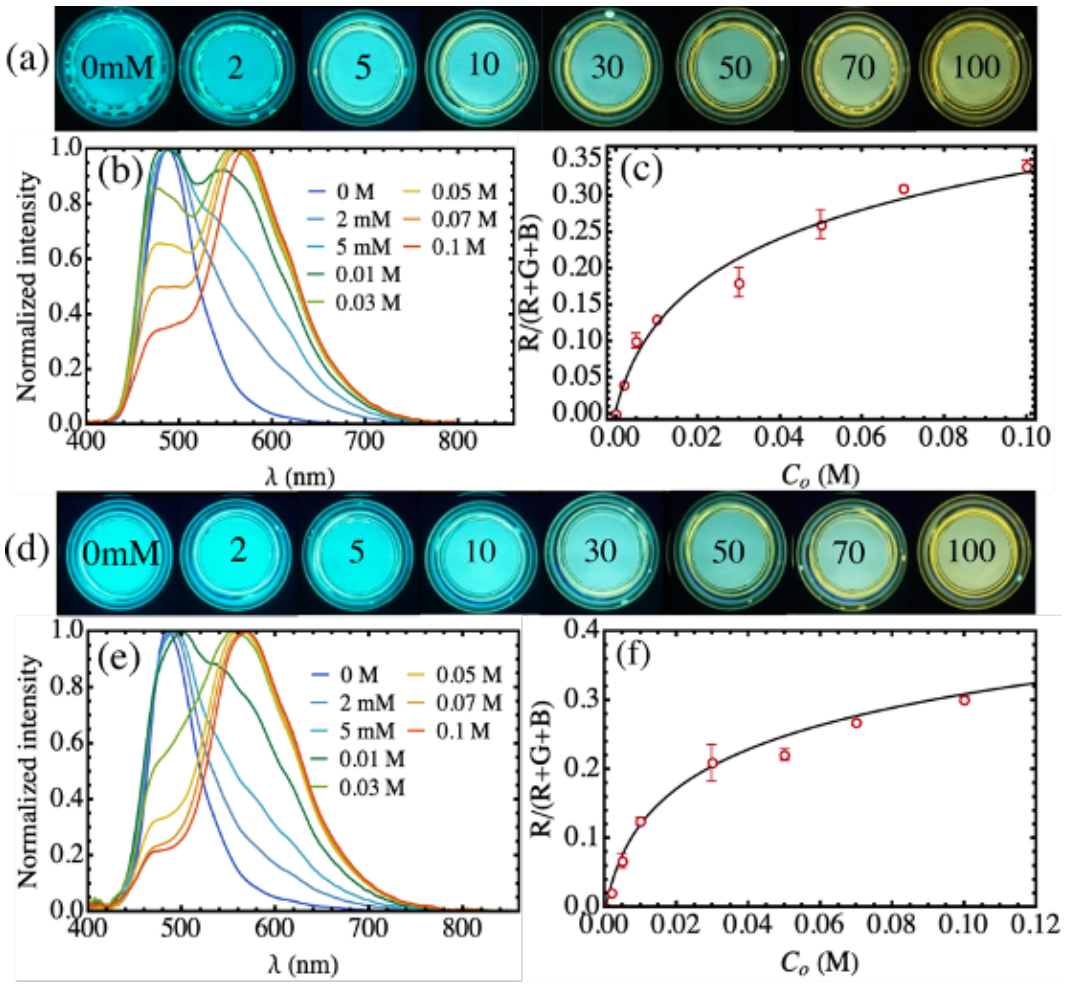

Figure 5.3: (a) Blacklight fluorescence photograph showing ten vials of octanol containing 7.41 mM np-P4VB. Salicylic acid was added at concentrations from $C_o = 0$ to 100 mM, as labeled on each vial from left to right; (b) the corresponding fluorescence spectra from the solutions in (a); (c) the calibration curve from the RGB intensity analysis of the vials in (a) fit using $S = aLog(bC_o+z)$, with the parameters a = 0.11, b = 214.18, and z = 1.08 (a). Panels (d-f) show the same information for 1.46 mM dye concentration, where the fitting parameters in (f) were a = 0.09, b = 279.08, and z = 0.92. Reprinted with permission from ACS Sens. 2022, 7, 1, 245–252. Copyright 2021 American Chemical Society.

from pale blue through pale green and eventually toward yellow, as the acid concentration increases (Fig. 5.3). The color change results from the protonation of the terminal pyridine groups and the resulting changes in the HOMO and LUMO energy levels of np-P4VB [204]. In order to determine the concentrations of salicylic acid into the droplets, we need to perform a second color calibration. The color shift signal is shown for two different dye concentrations (7.41 mM and 1.46 mM, in accordance with the dye concentrations in the droplets discussed below, as determined from the first calibration). With the signal defined in the same way as before, we obtain the salicylic acid calibration, which was then fit with a model given by $S = a \cdot \mathrm{Log}(bC_o + z)$, where C_o is the concentration of salicylic acid in water-saturated octanol, and a, b, and z are fitting parameters. The model is not intended to have physical meaning but does provide a reasonably good fit to the calibration data, and thus allows the concentration of salicylic acid to be estimated from a color analysis of the droplet fluorescence images. We also verified the emission colors and spectra for the different excitation wavelengths used (e.g., the blacklight, whose spectrum peaks around 370 nm, vs. the 405 nm LED) and found no meaningful differences.

5.3.2 Analysis of sensing dynamics

The octanol droplets (from Solution A) in milli-Q water yielded a visible pale blue fluorescence (Fig. 5.4, top left). As the salicylic acid solution (Solution C) was pumped over the droplets, the fluorescence gradually changed to yellow after a period of several minutes, indicating the protonation of np-P4VB in the octanol droplets. The color change occurred slowly at first, followed by an increasing rate of change toward the eventual saturation of the yellow emission. The intensities in the blue and green channels decreased over this time, whereas the intensity in red channel started at zero and increased over 5 minutes (Fig. 5.4, rows 2-4). The sensing signal was defined in the same way as previously (i.e., $S = R/(R+G+B)$), permitting a time-dependent measurement of C_o, the salicylic acid concentration in the droplets via the

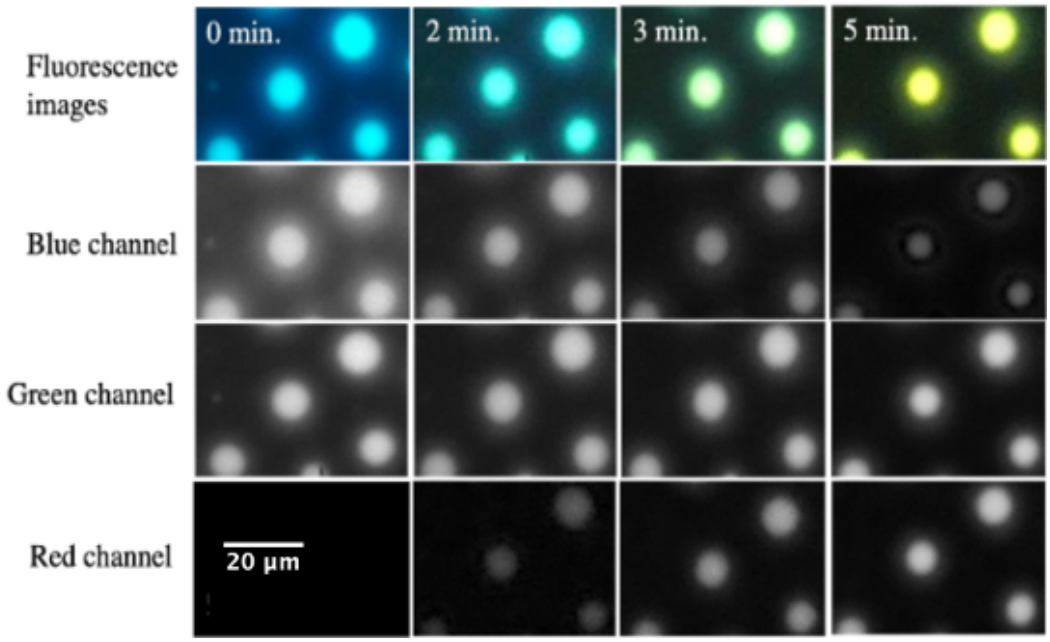

Figure 5.4: Fluorescence microscope images of fluorescent octanol droplets as flowing water with salicylic acid ($C_w = 10^{-3}$ M; Solution C) was pumped over them. The np-P4VB concentration in the droplets was found to be C_{P4VB} = 1.03 mM from the calibration curve in Fig. 5.2. The images were taken over a period of 5 minutes from the start of the fluid flow. These droplets ranged from approximately 4 to 20 micrometers in diameter. Reprinted with permission from ACS Sens. 2022, 7, 1, 245–252. Copyright 2021 American Chemical Society.

calibration curve in Fig. 5.3b.

At saturation, the fluorescence images in Fig. 5.4 (last column) avail a measure of the acid partition coefficient for salicylic acid, according to $P_{o/w} = C_o/C_w$ (where as before C_o and C_w are the concentrations of acid in the octanol droplet and the original aqueous phase, respectively, and $P_{o/w}$ is the partition coefficient). From a color analysis of in Fig. 5.4 (top right image) in which C_w was 1 mM, the acid concentration in the droplet was C_o = 495 mM, yielding a partition coefficient of $P_{o/w}$ = 251, in reasonably good agreement with a previously published value 224 for salicylic acid in the octanol-water system [245]. The observed color was independent of the dimensions of the droplet, which is unlike the case for absorption-based colorimetric imaging [223].

By converting the droplet colors to their corresponding acid concentration, we find that the time dependent acid concentration follows a sigmoidal curve with an onset delay followed by an increasing concentration change, and then eventually saturating near 192 and 90 mM, for $C_w = 10^{-4}$ and 10^{-6} M, respectively (Fig. 5.5). There was a clear, monotonic droplet size dependence of this process, with which occurred more quickly for the smallest droplets. A simple model was derived for the time dependence of C_t as a function of the droplet size, where several mechanisms were expected to contribute to the acid concentration in the droplet. First, there will be a delay time t_0 as Solution C is pumped into the chamber and replaces Solution B. Next, the boundary between solution B and C will not be a step function, but is instead a diffusive mixing region that will take some time to flow past the droplets. This depends on the mixing zone length and the fluid speed in the chamber (1.05 mm/s). Then once the droplet is exposed to a certain aqueous acid concentration, there is diffusion-driven mass transport of acid from the aqueous phase into the octanol droplet. Finally, the larger droplets will respond more slowly because of their larger volume and smaller surface-to-volume ratio.

To calculate the time dependence of the concentration, the mixing region was assumed to follow the one-dimensional diffusion equation. Obviously, the diffusion rate will be increased owing to the flow, which has Reynolds numbers of approximately 5 and 100 for the chamber and tubing, respectively, and is thus expected to be laminar [246], [247]. The mass transport is routinely modeled as a first-order reaction given by $dC_t/dT = AK/V(P_{o/w}C_w–C_o)$, where C_t is the acid concentration in the droplet at time t, A and V are the surface area and volume of a droplet, respectively, K is the mass transfer coefficient, and as before $P_{o/w}$ is C_o/C_w,. This yields $C_t/C_o = 1–exp(-KtA/V)$ after integration, where as before C_o is the saturation concentration in the octanol droplet (i.e., the value at the plateau of the curves in Fig. 5.5). These considerations yield:

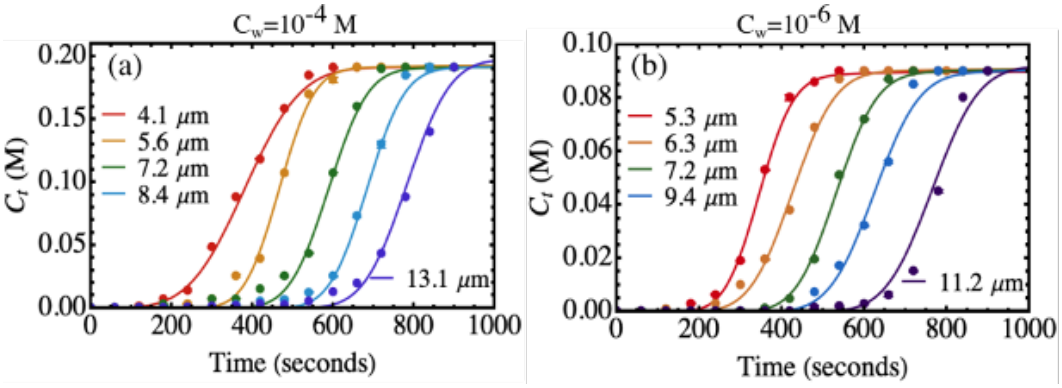

Figure 5.5: The relationship between the droplet concentration C_t and pumping time (minutes) for (a) 10^{-4} M and (b) 10^{-6} M salicylic acid in water, for several different droplet diameters (see the legends). The lines represent the best linear least squares fit from Eq. (5.1). The dye concentration in the droplets was 7.41 mM. Reprinted with permission from ACS Sens. 2022, 7, 1, 245–252. Copyright 2021 American Chemical Society.

$$C_t = B\left(\frac{1}{2}Erf\left(\frac{v\,(t-t_0)}{\sqrt{2Dt_0}}\right)+\frac{1}{2}\right)\cdot\left(1-exp\left(\frac{-3Kt}{R}\right)\right) \tag{5.1}$$

In Eq. (5.1), B is a scaling parameter, v is the flow velocity, t_0 is the time for the center of the mixing region to reach the droplet and yield a detectable color change, D is the effective diffusion coefficient for the acid in aqueous solution (Solutions B and C), t is the pumping time, and R is the droplet radius. The data in Fig. 5.5 were then fit with Eq. (5.1), with the free variables B, D, K, and t_0.

Eq. (5.1) fits the experimental data reasonably well overall (Fig. 5.5). The fitting parameters are summarized in the Appendix C, from which several observations can be made. First, the scaling pre-factor is similar for all sizes within each C_w, indicating that the saturated acid-in-droplet concentration C_o is effectively the same regardless of the droplet diameter. The delay times are close to the estimate obtained from the flow rate and the experimental dimensions (tubing and chamber lengths) but increase for the larger droplets because t_0 also depends on the ability to detect a signal from acid diffusing into proportionally larger droplets, an idea in accordance with previous colorimetric studies [223]. The effective diffusion coefficient for salicylic

acid in the aqueous solution was within the range of low 10^{-5} m^2/s in the model fits, which is about 4 orders of magnitude higher than the published value [248], [249]. The observed variations were likely due to experimental uncertainties (e.g., physically connecting the tubing to different syringes when switching solutions), but in general the high values are in agreement with a flow-related increase in the effective diffusion rate [250]. Despite the approximate nature of the model and the noise in the time-dependent data, there is good overall conformity with trend of the data (Fig. 5.5).

5.3.3 Measured partition coefficients

We next analyzed how the measured partition coefficients depend on the aqueous acid concentration C_w. The published partition coefficient for salicylic acid in the octanol-water is 224, which is similar to the value of $P_{o/w}$ = 251 that we obtain from the fluorescence analysis of the droplets at high C_w (Fig. 5.6b) [245]. However, the super partitioning of acid into the droplet is readily apparent in Fig. 5.6a, which plots C_o vs. C_w for two different values of C_{P4VB}. For all tested C_w, the saturated droplet concentration C_o was always larger for the higher dye concentration, implying that the dye enhances the partitioning of salicylic acid. Moreover, lower values of C_w lead to a significantly greater measured partition coefficient (Fig. 5.6b), which reaches values as high as 1.00×10^6 when C_w is 10 nM. Importantly, this enhancement can improve the limit of detection by similar orders of magnitude.

While the situation is complicated by the equilibria associated with the double protonation of the np-P4VB and the possible formation of various intermediates or associates, one can make a simple approximation by assuming that the np-P4VB will simply "lock away" a fraction of the dissociated protons via protonation of its terminal pyridines. Accordingly, one can write an effective partition, P_{eff}, as

$$P_{eff} = P_{o/w} + m \cdot (C_{P4VB}/C_w)^a \tag{5.2}$$

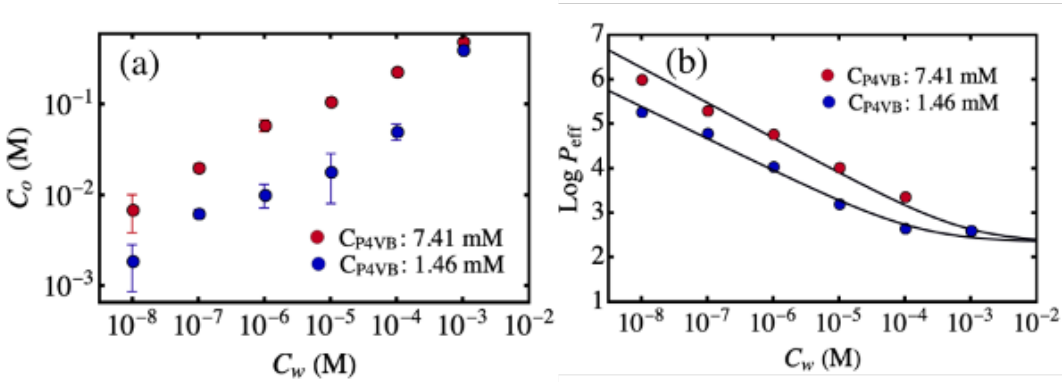

Figure 5.6: (a) The relationship between C_o (the acid concentration in the octanol droplets) and C_w (the acid concentration in water). The errors in C_w were assumed to be negligible. (b) The corresponding partition coefficients. The model fit is given by Eq. 2 with m =63.91, and a =0.77 for the 7.41 mM solution. For the C_{P4VB} = 1.46 mM, the fitting parameters were m = 47.21, and a = 0.72. The errors in Log(P_{eff}) were smaller than the data points. Reprinted with permission from ACS Sens. 2022, 7, 1, 245–252. Copyright 2021 American Chemical Society.

where m is an efficiency factor and C_{P4VB} is the dissolved dye concentration. Based on the published pKa = 2.97 for salicylic acid, aqueous free proton concentrations are about 1000 times lower than C_w; further, each np-P4VB molecule can accept two protons, leading to an additional enhancement of the droplet partition coefficent. By performing a linear-least-squares fit of Eq. (5.2) to the measured partition coefficients, we obtain the model lines shown in Fig. 5.6b. When C_w is higher than C_{P4VB}, there is so much acid that the enhanced partitioning associated with the dye becomes negligible, as can be seen from the flattening of the curves toward the expected value at high C_w in Fig. 5.6b and its eventual saturation at $P_{o/w} =\sim 260$, which is fairly close to the previously published value of 224 [245]. However, when $C_{P4VB} >> C_w$, then the presence of so much excess np-P4VB significantly enhances the partitioning of the acid into the droplet.

The super-partitioning effect could significantly lower the detection limit for fluorescent droplet-based sensing schemes. In order to verify this idea, we attempted to experimentally detect an aqueous acid concentration of 1 nM.

From the above discussion, one might expect that a high C_{P4VB} is desirable, but there is a trade-off against the ability to detect the fluorescence color shift. In other words, high C_{P4VB} enhances the super-partitioning effect, but it also means that more acid is required to protonate the minimum detectable fraction yellow-emitting dye molecules. In fact, from Fig. 5.6 we observe about a three-times enhancement of the partition for a tenfold increase in the dye concentration.

5.3.4 Limit of detection

The enhanced partitioning effect could lower the detection limit for fluorescent-droplet-based sensing schemes. To verify this, we attempted to experimentally detect an aqueous acid concentration of 1 nM. From the above discussion, one might expect that a high C_{P4VB} is desirable, but there is a trade-off against the ability to detect the fluorescence color shift. In other words, high C_{P4VB} enhances the partitioning, but it also means that more acid is required to protonate the minimum detectable yellow-emitting fraction of dye molecules.

To find an estimate of the LoD for this system, we therefore made two changes. We attempted to measure $C_w = 1$ nM, with an estimated C_{P4VB} concentration of 0.031 mM. For small levels of protonation, the color shift is correspondingly small and appears mainly in the green channel, as can be observed in Fig. 5.3b,e, where the initial response to the acid is a shift toward the green (which is then followed by the appearance of the orange emission peak). Therefore, for such low acid concentrations, we defined the signal as G/B. The response of this signal to $C_w = 1$ nM is shown in Fig. 5.7, over a 25-minute period from the initial injection of Solution C. Compared to the blank (Millipore water only), we find a clear increase in the sensing signal over this time frame. Obviously, the change becomes larger for longer times and may eventually lead to a sigmoidal curve as observed for much higher acid concentrations in Fig. 5.5.

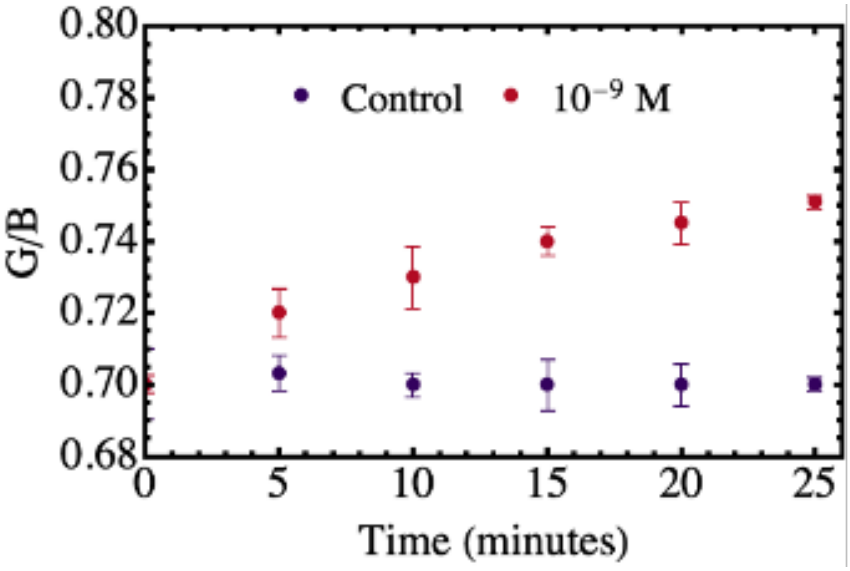

Figure 5.7: The sensing signal (G/B) as a function of time with $C_w = 1$ nM and $C_{P4VB} = 0.031$ mM compared to a control (milliPore water). The droplet diameter was 15 μm. The errors are from 4 independent measurements, in this case of a single pixel, as explained in the text. Reprinted with permission from ACS Sens. 2022, 7, 1, 245–252. Copyright 2021 American Chemical Society.

The LoD can be estimated from $3\sigma_{noise}/S$, where σ_{noise} is the uncertainty in the signal (see Appendix C) and S is the sensitivity, which is estimated from the magnitude of the change in the signal between the sample and the blank. Accordingly, after 25 minutes and using a single image pixel, we find that S = 0.045 nM^{-1} and σ_{noise} is 0.002. With these values, the LoD is 1.3×10^{-10} M. If we instead find the signal by averaging over 100 image pixels from the center of the vials, the noise was lowered to 0.0005 and the resulting LoD is 3.1×10^{-11} M. This is significantly better than previous fluorescence-sensing-based strategies for acid detection [219], [220], [222], and is even competitive with chemical sensing by more advanced and expensive methods such as surface enhanced Raman scattering for the detection of fluorescent dyes [240]. We repeated the process for a higher np-P4VB concentration, and obtained a slightly poorer LoD of 1.5×10^{-9} M, implying that the lower np-P4VB concentration better balanced the competing effects described previously. Potentially even lower LoDs might be obtained if the dye concentration were further optimized.

5.4 Final comments

The data suggest that the presence of the np-P4VB in the droplet is responsible for the enhanced partitioning of the acid. In all cases we found that the more dye was present in the droplet, the greater the resulting partition coefficient. However, the equilibrium concentrations of acid in the droplet were higher than expected based on the amount of dye present. For example, for $C_w = 0.1$ mM and $C_{P4VB} = 7.41$ mM, we found that the acid concentration was $C_o = 192$ mM. We had initially expected that the acid concentration enhancement might simply be found from bulk partition coefficient and the addition of twice the dye concentration because of the two protonation sites. This would yield an expected $C_o = P_{literature}C_w + 2C_{P4VB} = 224(0.1mM) + 2(7.41mM) = 37.2mM$, in comparison to the obtained value of 192 mM, for an additional unexpected enhancement by a factor of 5. This might be at least in part attributed to an error in the calibrations attributed from the IFE, although we made every effort to minimize this effect as described previously. Moreover, there is convincing evidence for association-related enhancement of the solute partition in water-octanol systems [251], [252] and for clustering or association during protonation of pyridine groups specifically [253]. We thus speculate that similar behavior may occur at the np-P4VB-terminal pyridine groups in the slightly acidified octanol droplets. Finally, we briefly comment on the trade-off between throughput and LoD. This sensor concept was designed for minimizing the LoD, which in general has a trade-off with respect to throughput for practical sensing applications. Here, one analysis takes ca. 5-20 min to perform depending on the degree of sensitivity required, whereas simply by infusing our dye into filter papers we can easily perform acid sensing well into the sub-mM regime in a matter of seconds. However, the LoD for the droplet-based sensing shown here is far lower and is one of the lowest reported for fluorescence-based sensors.

5.5 Conclusion

Droplet-based chemical sensing depends on the preferential partitioning of the analyte from the bulk phase into the droplet. The fluorescent droplet methods developed here are not subject to optical thickness color variations in comparison to previous methods. Strictly speaking, the detection apparatus needs to consist only of an objective lens and a consumer camera. This is possible because color-change fluorescence, as opposed to quenching, offers the ability to perform a ratiometric analysis from color images, increasing the ease of use and resulting in stable and repeatable sensing performance. We demonstrated that fluorescent droplets, when incorporating a specially prepared dye, can lower the LoD by more than 6 orders of magnitude compared to droplet-based colorimetric methods, and established by a fairly wide margin, to the best of our knowledge, the lowest detection limit reported for droplet- based optical sensing technologies. Moreover, we demonstrate detection from an aqueous analyte, which is important for certain applications.

Droplet-based sensing schemes appear to have the potential to compete with or even exceed the ability of much more complicated and expensive methods, such as surface-enhanced Raman scattering, to detect exceptionally low concentrations of the desired analyte. The method could be readily extended to other analytes; for example, the np-P4VB molecule is also sensitive to a small number of other cations (specifically Zn^{2+} and Cd^{2+}), which cause fluorescence color changes into green or yellow, respectively [119]. Although this would require careful calibration to avoid cross sensitivity to these two cations, other color-change chromophores could, in principle, be designed for specific analytes using the same principles as those explored here.

Chapter 6

Conclusion and future works

6.1 Summary

The main objective of this work was to study the optical performance and sensing applications of distyrylbenzene-related fluorophore (P4VB). In the first part, we reviewed the basic photophysics of organic fluorophores. The history of distyrylbenzene-related P4VB-type derivatives was summarized and their properties were compared to those of P4VB to understand its optical and sensing performance.

Chapter 2 mainly discussed the experimental methods used in the research work. The methods used for the optical measurements, such as fluorescence, absorption, QY, and TRPL, as well as the preparation methods, were discussed in more detail than was done in the publications in order to help make the work more reproducible. I also described some of the difficulties encountered, such as the photobleaching effects from the LED light source while attempting sensing measurements, and how these difficulties were handled.

Chapters 3 to chapter 5 were published papers about P4VB. Chapter 3 focused on a large color shift of P4VB under exposure to different local environments and described a P4VB-metal organic framework system. In that chapter, the basic characterization of P4VB was performed, and then it was utilized as an organic linker for Zn-based MOF. This system has a highly polarized fluorescence because of the alignment of P4VB along the MOF axis,

and the MOF crystals also showed a strong fluorescence color change when exposed to acid vapor.

Chapter 4 focused on a gas sensing application of P4VB. That work developed a P4VB-infused paper-based CO_2 sensor with a high sensitivity and simple design. The sensing mechanism was based on the formation of carbonic acid from CO_2 and water; the resulting protonation and associated fluorescence color shift of the P4VB resulted in the sensing signal. The ratiometric spectral analysis method minimizes the effects of photobleaching from the LED light source. The P4VB-infused paper sensor could detect (100 ppm (experimental) and 5.7 ppm of CO_2 (calculated)) and has a response time of $\sim$1 minute.

Chapter 5 discussed the sensing performance of P4VB-loaded oil droplets. P4VB was incorporated in octanol to form fluorescent droplets. Sensing was strongly enhanced by the large partition coefficient of the analyte (salicylic acid) between the surrounding water and the oil droplets. The salicylic acid is partitioned into oil phase from the water phase and concentrated inside the small droplets, lowering the overall limit of detection by orders of magnitude. The LoD was lowest among reported droplet-based sensing technologies.

6.2 Future work

Leading from the work in this thesis, the next main project to be embarked upon is to see if P4VB can be functionalized for binding to proteins for biological sensing and imaging applications. The project was initially started as a spin-off from my work, and led already to one publication in Nano Letters, on which I was the fourth author [254]. Currently we are binding P4VB inside live cells and find that it penetrates the cell and binds to actin filaments and other cellular structures. The hope is that P4VB may serve as a pH sensor inside the cell, allowing one to measure subtle changes in pH character (for example, between healthy cells and cancer cells). The results so far are pre-

liminary and we do not yet know whether this idea will work or not, but if so, it could have a fairly profound influence in terms of the kinds of data one can report in biological imaging.

The second direction enabled from this thesis is in the area of droplet-based fluorescence sensing. Obviously, P4VB is not the only fluorophore that could capitalize from the partition coefficient between an aqueous analyte and a liquid droplet. I am currently working with PDFs Razieh Firouji Haji and Maryam Aghajamali (University of Calgary) to show a similar drastic improvement of the sensing capacity with graphene quantum dots in dichlorobenzene droplets, for ultrasensitive detection of nitro-aromatics. So far, this work is proving successful and a manuscript is in submission on which I am the lead author.

At minimum, these two directions appear to be rewarding avenues for further study. While organic fluorophores have been widely studied and investigated for a very long time, the richness of organic chemistry and the ability to do so much with molecular fluorophores implies that it will be fertile ground for decades to come.

References

[1] N. V. Ignatov and F. F. Litvin, "Photoinduced formation of pheophytin-/chlorophyll-containing complexes during the greening of plant leaves," *Photosynthesis Research*, vol. 42, no. 1, pp. 27–35, 1994. 1

[2] S.-Y. Seo, J. Lee, J. H. Shin, E.-S. Kang, and B.-S. Bae, "The thermo-optic effect of si nanocrystals in silicon-rich silicon oxidethin films," *Applied physics letters*, vol. 85, no. 13, pp. 2526–2528, 2004. 1

[3] S. J. Remington, "Green fluorescent protein: A perspective," *Protein Science*, vol. 20, no. 9, pp. 1509–1519, 2011. 1

[4] R. M. C. Dawson, D. C. Elliott, W. H. Elliott, and K. M. Jones, *Data for biochemical research*. Clarendon press, 2002, vol. 3. 1

[5] S. Benkhaya, S. M'rabet, and A. El Harfi, "Classifications, properties, recent synthesis and applications of azo dyes," *Heliyon*, vol. 6, no. 1, e03271, 2020. 1, 2

[6] ——, "A review on classifications, recent synthesis and applications of textile dyes," *Inorganic Chemistry Communications*, vol. 115, p. 107 891, 2020. 1

[7] G. T. Hermanson, *Bioconjugate techniques*. Academic press, 2013. 2

[8] W. A. McMillan, *Compositions and methods enabling a totally internally controlled amplification reaction*, US Patent 6,312,929, Nov. 2001. 2

[9] J. B. Birks and L. G. Christophorou, "Excimer fluorescence spectra of pyrene derivatives," *Spectrochimica Acta*, vol. 19, no. 2, pp. 401–410, 1963. 2

[10] M. R. Osborne and N. T. Crosby, *Benzopyrenes*. Benzopyrenes, 1987. 2

[11] L. Brooker, "The cyanine dyes and related compounds.," *Interscience Publishers,*, 1964. 2

[12] O. Valdes-Aguilera and D. C. Neckers, "Aggregation phenomena in xanthene dyes," *Cheminform*, vol. 22, no. 35, 1989. 2

[13] J. F. Corbett, "A relationship between colour and structure for simple nitro dyes," *Coloration Technology*, vol. 83, no. 7, pp. 273–276, 2010. 2

[14] F. Ramirez and S. Dershowitz, "The structure of quinone-donor adducts. i. the action of triphenylphosphine on p-benzoquinone, 2,5-dichloro-p-benzoquinone and chloranil," *Journal of the American Chemical Society*, vol. 78, no. 21, pp. 5614–5622, 1956. 2

[15] V. K. Sharma, P. D. Sahare, R. C. Rastogi, S. K. Ghoshal, and D. Mohan, "Excited state characteristics of acridine dyes: Acriflavine and acridine orange," *Spectrochimica Acta Part A Molecular and Biomolecular Spectroscopy*, vol. 59, no. 8, pp. 1799–1804, 2003. 2

[16] K. H. Drexhage, "Fluorescence efficiency of laser dyes," *Journal of Research of the National Bureau of Standards*, vol. 80A, no. 3, p. 421, 1976. 2

[17] M. Clark, "Handbook of textile and industrial dyeing," 2011. 2

[18] K. Hara, T. Sato, R. Katoh, A. Furube, Y. Ohga, A. Shinpo, S. Suga, K. Sayama, H. Sugihara, and H. Arakawa, "Molecular design of coumarin dyes for efficient dye-sensitized solar cells," *J.phys.chem.b*, vol. 107, no. 2, pp. 597–606, 2003. 2

[19] C. Miao, W. Cui, H. Zhou, R. Wang, and W. Yang, "Nondoped, deep-blue, organic light-emitting diodes with low-efficiency roll-off based on a simple anthracene–triazole hybrid fluorescent molecule," *Dyes and Pigments*, p. 109 672, 2021. 2

[20] T. E. Bush and G. W. Scott, "Fluorescence of distyrylbenzenes," *Journal of Physical Chemistry*, vol. 85, no. 2, pp. 144–146, 2002. 2

[21] B. S. Pilgrim and N. R. Champness, "Metal-organic frameworks and metal-organic cages – a perspective," *ChemPlusChem*, vol. 85, no. 8, 2020. 4

[22] H. Xu, R. Chen, Q. Sun, W. Lai, Q. Su, W. Huang, and X. Liu, "Recent progress in metal–organic complexes for optoelectronic applications," *Chemical Society Reviews*, vol. 43, no. 10, pp. 3259–3302, 2014. 4

[23] S. J. Tang, Z. Liu, Y. J. Qian, K. Shi, Y. Sun, C. Wu, Q. Gong, and Y. F. Xiao, "A tunable optofluidic microlaser in a photostable conjugated polymer," *Advanced Materials*, vol. 30, no. 50, pp. 1804556.1–1804556.7, 2018. 4

[24] U. Scherf, S. Riechel, U. Lemmer, and R. Mahrt, "Conjugated polymers: Lasing and stimulated emission," *Current Opinion in Solid State and Materials Science*, vol. 5, no. 2-3, pp. 143–154, 2001. 4

[25] D. Raković, R. Kostić, L. Gribov, S. Stepanyan, and I. Davidova, "Vibrational spectroscopy and comparative study of trans-polyacetylene, poly (p-phenylene) and poly (p-phenylene vinylene)," *Synthetic metals*, vol. 41, no. 1-2, pp. 275–278, 1991. 4

[26] G. W. Yoder, "Theoretical studies of electronic structure and bonding properties of conjugated polymers," Ph.D. dissertation, 1998. 4

[27] P. Jaideaw, *Optical and Electrical Properties of Multilayer Poly (2-methoxy-5-(2'-ethylhexyloxy)-1, 4-phenylene Vinylene)(MEH-PPV) and Organic Thin Films*. Mahidol University, 2003. 5

[28] B. Geffroy, P. L. Roy, and C. Prat, "Organic lightmitting diode (oled) technology: Materials, devices and display technologies," *Polymer International*, vol. 55, 2006. 5

[29] X. Zhou, D. S. Qin, M. Pfeiffer, J. Blochwitz-Nimoth, A. Werner, J. Drechsel, B. Maennig, K. Leo, M. Bold, and P. Erk, "High-efficiency electrophosphorescent organic light-emitting diodes with double light-emitting layers," *Applied Physics Letters*, vol. 81, no. 21, pp. 4070–4072, 2002. 5

[30] W. Cheng, H. Chen, C. Liu, C. Ji, and M. Yin, "Functional organic dyes for health-related applications," *View*, p. 20 200 055, 2020. 5

[31] X. Li, L. Yang, L. Zhao, X. L. Wang, K. Z. Shao, and Z. M. Su, "Luminescent metal-organic frameworks with anthracene chromophores: Small-molecule sensing and highly selective sensing for nitro explosives," *Crystal Growth & Design*, acs.cgd.6b00482, 2016. 5

[32] J. Jeon, K. H. Lee, and J. Rao, "A strategy to enhance the binding affinity of fluorophore–aptamer pairs for rna tagging with neomycin conjugation," *Chemical Communications*, vol. 48, no. 80, p.10034–10 036, 2012. 5

[33] S. Lane, S. Vagin, H. Wang, W. Heinz, W. Morrish, Y. Zhao, B. Rieger, and A. Meldrum, "Wide-gamut lasing from a single organic chromophore," *Light: Science & Applications*, vol. 7, no. 1, pp. 1–9, 2018. 5, 20, 24

[34] J. L. Belmonte-Vázquez, Y. A. Amador-Sánchez, L. A. Rodrıguez-Cortés, and B. Rodrıguez-Molina, "Dual-state emission (dse) in organic fluorophores: Design and applications," *Chemistry of Materials*, vol. 33, no. 18, pp. 7160–7184, 2021. 5

[35] D. Purohit, C. P. Sharma, A. Raghuvanshi, A. Jain, K. S. Rawat, N. M. Gupta, J. Singh, M. Sachdev, and A. Goel, "First dual responsive "turn-on" and "ratiometric" aiegen probe for selective detection of hydrazine both in solution and the vapour phase," *Chemistry–A European Journal*, vol. 25, no. 18, pp. 4660–4664, 2019. 5

[36] A. Ferguson, *Dye laser principles with applications*, 1991. 5

[37] M. C. Gather and S. H. Yun, "Single-cell biological lasers," *Nature Photonics*, vol. 5, no. 7, pp. 406–410, 2011. 6

[38] J. Daintith, *A dictionary of chemistry*. OUP Oxford, 2008. 6

[39] J. E. Huheey, E. A. Keiter, R. L. Keiter, and O. K. Medhi, *Inorganic chemistry: principles of structure and reactivity*. Pearson Education India, 2006. 6

[40] A. V. Mitin, "Exact solution of the hartree-fock equation for the h_2 molecule in the linear-combination-of-atomic-orbitals approximation," *Physical Review A*, vol. 62, no. 1, p. 010 501, 2000. 6

[41] C. D. Sherrill, "An introduction to hartree-fock molecular orbital theory," *School of Chemistry and Biochemistry Georgia Institute of Technology*, 2000. 6

[42] T. J. Zielinski, E. Harvey, R. Sweeney, and D. M. Hanson, "Quantum states of atoms and molecules," *Journal of Chemical Education*, vol. 82, no. 12, p. 1880, 2005. 6, 7

[43] *Bonding in hydrogen*, `http://butane.chem.uiuc.edu/pshapley/genchem1/L10/1.html`, Accessed: 2022-06-06. 6

[44] J. E. House, *Inorganic chemistry*. Academic Press, 2019. 7

[45] L. Pauling, "The nature of the chemical bond. application of results obtained from the quantum mechanics and from a theory of paramagnetic susceptibility to the structure of molecules," *Journal of the American Chemical Society*, vol. 53, no. 4, pp. 1367–1400, 1931. 7

[46] ——, *The nature of the chemical bond—1992*, 7. ACS Publications, 1992, vol. 69, p. 519. 7

[47] J. E. Huheey, E. A. Keiter, R. L. Keiter, and O. K. Medhu, "Inorganic chemistry," *j.chem.soc.abstr*, vol. 14, no. 340, pp. 12–12, 1893. 7

[48] "Hybridisation," Accessed: 2022-06-06. 7, 8

[49] "Hybridization of c_2h_2 - acetylene (ethyne)," Accessed: 2022-06-06. 8

[50] B. W. Darvell, "Resin restorative materials," *Materials Science for Dentistry (Tenth edition)*, 2018. 9

[51] G. L. Miessler and D. A. Tarr, *Inorganic Chemistry*. 1990. 9

[52] A. Shimizu, Y. Ishizaki, S. Horiuchi, T. Hirose, K. Matsuda, H. Sato, and J.-i. Yoshida, "Homo–lumo energy-gap tuning of π-conjugated zwitterions composed of electron-donating anion and electron-accepting cation," *The Journal of Organic Chemistry*, vol. 86, no. 1, pp. 770–781, 2020. 9

[53] D. W. Turner, *Photoelectron Spectroscopy*. 1974. 9

[54] C. L. Pettiette, S. H. Yang, M. J. Craycraft, J. Conceicao, R. T. Laaksonen, O. Cheshnovsky, and R. E. Smalley, "Ultraviolet photoelectron spectroscopy of copper clusters," *Journal of Chemical Physics*, vol. 88, no. 9, pp. 5377–5382, 1988. 9

[55] M. Zhu, H. Qian, and R. Jin, "Thiolate-protected au(20) clusters with a large energy gap of 2.1 ev.," *Journal of the American Chemical Society*, vol. 131, no. 21, pp. 7220–7221, 2009. 9

[56] R. S. Assary, F. R. Brushett, and L. A. Curtiss, "Reduction potential prediction of some aromatic nitrogen containing molecules," *RSC Advances*, vol. 4, 2014. 9

[57] A. K. Mishra and S. P. Tewari, "Density functional theory calculations of spectral, nlo, reactivity, nbo properties and docking study of vincosamide-n-oxide active against lung cancer cell lines h1299," *SN Applied Sciences*, vol. 2, no. 6, pp. 1–13, 2020. 9, 10

[58] Rabalais, J. Wayne, and J. W. Rabalais, *Principles of ultraviolet photoelectron spectroscopy*. Principles of ultraviolet photoelectron spectroscopy, 1977. 9

[59] M. Marghany, "Principle theories of synthetic aperture radar," *Synthetic Aperture Radar Imaging Mechanism for Oil Spills*, pp. 127–150, 2020. 9

[60] A. P. French and E. F. Taylor, *An introduction to quantum physics*. Routledge, 2018. 9

[61] C., Dennis, Hall, Nelson, W., Sharpe, Ian, P., Danks, and Yu, "Cyclic voltammetry studies on the complexation of metal cations by cryptands containing the ferrocene unit," *Journal of the Chemical Society*, vol. 7, no. 7, pp. 419–421, 1989. 9, 10

[62] R. M. Dreizler and E. K. Gross, *Density functional theory: an approach to the quantum many-body problem*. Springer Science & Business Media, 2012. 10

[63] T. Van Mourik, M. Bühl, and M.-P. Gaigeot, *Density functional theory across chemistry, physics and biology*, 2014. 10

[64] K. Burke, "Perspective on density functional theory," *The Journal of chemical physics*, vol. 136, no. 15, p. 150 901, 2012. 10

[65] P. Atkins and J. De Paula, *Atkins' physical chemistry, volume 8. ed*, 2006. 10

[66] V. Gold, *Compendium of chemical terminology*. Blackwell scientific publications, 1987. 11

[67] B. H. Bransden and C. J. Joachain, "Introduction to quantum mechanics," 1989. 11

[68] D. Frackowiak, "The jablonski diagram," *Journal of Photochemistry and Photobiology B Biology*, vol. 2, no. 3, pp. 399–399, 1988. 12, 13

[69] A. D. Craik, "George gabriel stokes on water wave theory," *Annu. Rev. Fluid Mech.*, vol. 37, pp. 23–42, 2005. 14

[70] C. M. Marian, "Understanding and controlling intersystem crossing in molecules," *Annual Review of Physical Chemistry*, vol. 72, no. 1, 2021. 14

[71] G. Nic, J. Jirat, B. Košata, S. A. Jenkins, and A. D. Mcnaught, *IUPAC Compendium of Chemical Terminology*. 2006. 14

[72] I. Kim, K. H. Cho, S. O. Jeon, W.-J. Son, D. Kim, Y. M. Rhee, I. Jang, H. Choi, and D. S. Kim, "Three states involving vibronic resonance is a key to enhancing reverse intersystem crossing dynamics of an organoboron-based ultrapure blue emitter," *JACS Au*, vol. 1, no. 7, pp. 987–997, 2021. 14

[73] C. M. Marian, "Spin–orbit coupling and intersystem crossing in molecules," *Wiley Interdisciplinary Reviews Computational Molecular Science*, vol. 2, no. 2, pp. 187–203, 2012. 14

[74] J. Vanderkooi, "An optical method for measurement of dioxygen concentration based upon quenching of phosphorescence.," *Journal of Biological Chemistry*, vol. 262, no. 12, pp. 5476–5482, 1987. 14

[75] P. J. Modreski and R. Aumente-Modreski, "Fluorescent minerals: A review," *Rocks & Minerals*, vol. 71, no. 1, pp. 14–22, 1996. 14

[76] D. C. Harris and M. D. Bertolucci, *Symmetry and spectroscopy: an introduction to vibrational and electronic spectroscopy*. Courier Corporation, 1989. 14, 15

[77] A. R. Edmonds and H. Mendlowitz, "Angular momentum in quantum mechanics," *Physics Today*, vol. 11, no. 4, pp. 34–38, 1958. 15

[78] A. M. Ellis, "Spectroscopic selection rules: The role of photon states," *Journal of chemical education*, vol. 76, no. 9, p. 1291, 1999. 15

[79] S. G. Schulman, Q. Q. Di, and J. Juchum, "Fluorescence spectroscopy, organic chemistry applications," 2017. 16

[80] Berlman and B. Isadore, "Identifying the lowest excited singlet state of biphenyl and its analogs," *Journal of Chemical Physics*, vol. 52, no. 11, pp. 5616–5621, 1970. 16

[81] "Fluorescence and phosphorescence," Accessed: 2022-06-06. 16

[82] C. King, B. Barbiellini, D. Moser, and V. Renugopalakrishnan, "Exactly soluble model of resonant energy transfer between molecules," *Physical Review B Condensed Matter*, vol. 85, no. 12, pp. 1092–1097, 2012. 17

[83] A. P. Demchenko, *Introduction to Fluorescence Sensing*. 2009. 17

[84] T. Förster and O. Sinanoglu, "Modern quantum chemistry," *Academic Press, New York*, vol. 3, pp. 93–137, 1965. 17

[85] M. A. Rizzo, G. H. Springer, B. Granada, and D. W. Piston, "An improved cyan fluorescent protein variant useful for fret," *Nature Biotechnology*, vol. 22, no. 4, pp. 445–449, 2004. 18

[86] P.-C. Cheng, "The contrast formation in optical microscopy," in *Handbook of biological confocal microscopy*, Springer, 2006, pp. 162–206. 18

[87] D. L. Dexter, "A theory of sensitized luminescence in solids," *The journal of chemical physics*, vol. 21, no. 5, pp. 836–850, 1953. 18

[88] *Dexter energy transfer*, https://chem.libretexts.org/Bookshelves/Physical_and_Theoretical_Chemistry_Textbook_Maps/Supplemental_Modules_(Physical_and_Theoretical_Chemistry)/Fundamentals/Dexter_Energy_Transfer, Accessed: 2022-06-27. 19

[89] R. J. Mayer and A. R. Ofial, "Nucleophilic reactivities of bleach reagents," *Organic Letters*, p. 2816, 2018. 19

[90] A. Hauser, "Intersystem crossing in the [fe $(ptz)_6$]$(bf_4)_2$ spin crossover system (ptz= 1-propyltetrazole)," *The Journal of chemical physics*, vol. 94, no. 4, pp. 2741–2748, 1991. 19

[91] M. C. DeRosa and R. J. Crutchley, "Photosensitized singlet oxygen and its applications," *Coordination Chemistry Reviews*, vol. 233, pp. 351–371, 2002. 20

[92] N. F. Desai and C. Giles, "The oxidation of azo dyes and its relation to light fading," *Journal of the Society of Dyers and Colourists*, vol. 65, no. 12, pp. 639–649, 1949. 20

[93] K. Isayama, N. Aizawa, J. Y. Kim, and T. Yasuda, "Modulating photo- and electroluminescence in a stimuli-responsive π-conjugated donor–acceptor molecular system," *Angewandte Chemie*, vol. 130, no. 37, pp. 12 158–12 162, 2018. 21

[94] J. Fan, M. Hu, P. Zhan, and X. Peng, "Energy transfer cassettes based on organic fluorophores: Construction and applications in ratiometric sensing," *Cheminform*, vol. 42, no. 1, pp. 29–43, 2012. 21

[95] C. Reichardt, "Solvatochromic dyes as solvent polarity indicators," *Chemical reviews*, vol. 94, no. 8, pp. 2319–2358, 1994. 21, 39

[96] H. Heinz, U. W. Suter, and E. Leontidis, "Simple and accurate computations of solvatochromic shifts in $\pi \rightarrow \pi^*$ transitions of aromatic chromophores," *Journal of the American Chemical Society*, vol. 123, no. 45, pp. 11 229–11 236, 2001. 21

[97] J. F. Deye, T. Berger, and A. G. Anderson, "Nile red as a solvatochromic dye for measuring solvent strength in normal liquids and mixtures of normal liquids with supercritical and near critical fluids [erratum to document cited in ca112 (18): 171383n]," *Analytical Chemistry*, vol. 62, no. 14, pp. 1552–1552, 1990. 21

[98] M. J. Minch and S. S. Shah, "Merocyanin dye preparation for the introductory organic laboratory," *Journal of Chemical Education*, vol. 54, no. 11, p. 709, 1977. 21

[99] L. Lu and S. A. Jenekhe, "Poly(vinyl diphenylquinoline): A new phtunable light-emitting and charge-transport polymer synthesized by a simple modification of polystyrene," *Macromolecules*, vol. 34, no. 18, pp. 6249–6254, 2001. 22

[100] P. Samanta, S. Dutta, and S. K. Ghosh, "Metal-organic frameworks for detection and desensitization of environmentally hazardous nitro-explosives and related high energy materials," *Metal-Organic Frameworks (MOFs) for Environmental Applications*, pp. 231–283, 2019. 22

[101] H. Haschimoto, *Comprehensive supramolecular chemistry*. 1996. 22

[102] Y. Ma, Z. Zhong, F. Peng, L. Ying, J. Xiong, J. Peng, and Y. Cao, "Dual hole transport layers for blue-light-emitting pled: Suppress the formation of exciplex towards high device performance and color purity," *Organic Electronics*, vol. 68, pp. 103–107, 2019. 23

[103] D. Luo, C.-W. Liao, C.-H. Chang, C.-C. Tsai, C.-W. Lu, T. C. Chuang, and H.-H. Chang, "Approach to fast screen the formation of an exciplex," *The Journal of Physical Chemistry C*, vol. 124, no. 18, pp. 10 175–10 184, 2020. 23

[104] G. K. Bains, S. H. Kim, E. J. Sorin, and V. Narayanaswami, "The extent of pyrene excimer fluorescence emission is a reflector of distance and flexibility: Analysis of the segment linking the ldl receptor-binding and tetramerization domains of apolipoprotein e3.," *Biochemistry*, vol. 51, no. 31, pp. 6207–6219, 2012. 23

[105] F. J. Duarte, *Tunable lasers handbook*. Elsevier, 1996. 23

[106] "Excimer lasers," Accessed: 2022-06-06. 23

[107] T. E. Bush and G. W. Scott, "Fluorescence of distyrylbenzenes," *Journal of Physical Chemistry*, vol. 85, no. 2, pp. 144–146, 2002. 23, 24

[108] E. Ebeid and A. J. Lees, "Molecular association in flexible diolefinic dyes," *The Journal of Physical Chemistry*, vol. 91, no. 22, pp. 5792–5795, 1987. 24, 25

[109] S. Vagin, A. Ott, H. C. Weiss, A. Karbach, D. Volkmer, and B. Rieger, "Metal-organic frameworks (mofs) composed of (triptycenedicarboxylato)zinc," *European Journal of Inorganic Chemistry*, 2008. 24

[110] A. Saini, K. J. Thomas, A. Sachdev, and P. Gopinath, "Photophysics, electrochemistry, morphology, and bioimaging applications of new 1, 8-naphthalimide derivatives containing different chromophores," *Chemistry–An Asian Journal*, vol. 12, no. 19, pp. 2612–2622, 2017. 38

[111] E. R. Reddy, S. Yellanki, R. Medishetty, L. Konada, N. P. Alamuru, D. Haldar, K. V. Parsa, P. Kulkarni, and M. Rajadurai, "Inside cover: Red fluorescent organic nanoparticle bioprobes: A photostable cytoplasmic stain for long term in vitro and in vivo visualization (chemnanomat 8/2015)," *ChemNanoMat*, vol. 1, no. 8, pp. 531–531, 2015. 38

[112] Y. Liu, C. H. Wolstenholme, G. C. Carter, H. Liu, H. Hu, L. S. Grainger, K. Miao, M. Fares, C. A. Hoelzel, H. P. Yennawar, *et al.*, "Modulation of fluorescent protein chromophores to detect protein aggregation with turn-on fluorescence," *Journal of the American Chemical Society*, vol. 140, no. 24, pp. 7381–7384, 2018. 38

[113] R. Z. Wu, X. Yang, L. Zhang, and P. Zhou, "Luminescent lanthanide metal-organic frameworks for chemical sensing and toxic anion detection," *Dalton Transactions*, vol. 46, no. 30, 2017. 38

[114] N. V. Roik, L. A. Belyakova, and M. O. Dziazko, "Optically transparent silica film with ph-sensing properties: Influence of chemical immobilization and presence of β-cyclodextrin on protolytic properties of alizarin yellow," *Sensors and Actuators B: Chemical*, vol. 273, pp. 1103–1112, 2018. 38

[115] H. Youtaro, M. Shinya, F. Toshiyuki, T. Shun, Y. Kenichi, and S. Fumio, "High-gain and wide-band optical amplifications induced by a coupled excited state of organic dye molecules co-doped in polymer waveguide," *Optics Letters*, vol. 43, no. 8, p. 1714, 2018. 38

[116] Y. Dong, J. Zhang, X. Tan, L. Wang, J. Chen, B. Li, L. Ye, B. Xu, B. Zou, and W. Tian, "Multi-stimuli responsive fluorescence switching: The reversible piezochromism and protonation effect of a divinylanthracene derivative," *Journal of Materials Chemistry C*, vol. 1, no. 45, pp. 7554–7559, 2013. 38

[117] M. Germain and M. Knapp, "Optical explosives detection: From color changes to fluorescence turn-on," *Cheminform*, vol. 38, no. 9, pp. 2543–2555, 2009. 38, 55

[118] Z. Tian, W. Wu, W. Wei, and A. Li, "Single-chromophore-based photoswitchable nanoparticles enable dual-alternating-color fluorescence for unambiguous live cell imaging," *Journal of the American Chemical Society*, vol. 131, no. 12, pp. 4245–52, 2009. 38

[119] S. Lane, S. Vagin, H. Wang, W. Heinz, W. Morrish, Y. Zhao, B. Rieger, and A. Meldrum, "Wide-gamut lasing from a single organic chromophore," *Light: Science & Applications*, vol. 7, no. 1, pp. 1–9, 2018. 38, 40, 58, 59, 63, 72, 74

[120] P. Chen, Q. Li, S. Grindy, and N. Holten-Andersen, "White-light-emitting lanthanide metallogels with tunable luminescence and reversible stimuli-responsive properties," *Journal of the American Chemical Society*, vol. 137, no. 36, pp. 11 590–11 593, 2015. 38

[121] N. Khanapurmath, M. V. Kulkarni, L. Pallavi, J. Yenagi, and J. Tonannavar, "Solvatochromic studies on 4-bromomethyl-7-methyl coumarins," *Journal of Molecular Structure*, vol. 1160, pp. 50–56, 2018. 38

[122] N. Srividya, P. Ramamurthy, and V. T. Ramakrishnan, "Solvent effects on the absorption and fluorescence spectra of some acridinedione dyes: Determination of ground and excited state dipole moments," *Spectrochimica Acta Part A Molecular Biomolecular Spectroscopy*, vol. 53, no. 11, pp. 1743–1753, 1997. 38

[123] S. S. Deshpande, H. S. Kumbhar, and G. S. Shankarling, "Solvatochromic fluorescence properties of phenothiazine-based dyes involving thiazolo [4, 5-b] quinoxaline and benzo [e] indole as strong acceptors," *Spectrochimica Acta Part A: Molecular and Biomolecular Spectroscopy*, vol. 174, pp. 154–163, 2017. 38

[124] J. Kabatc, B. Omiaowski, and J. Pczkowski, "The experimental studies on the determination of the ground and excited state dipole moments of some hemicyanine dyes," *Spectrochimica Acta Part A: Molecular and Biomolecular Spectroscopy*, vol. 63, no. 3, pp. 524–531, 2006. 39

[125] Y. Kubota, Y. Sakuma, K. Funabiki, and M. Matsui, "Solvatochromic fluorescence properties of pyrazine–boron complex bearing a β-iminoenolate ligand," *The Journal of Physical Chemistry A*, vol. 118, no. 38, pp. 8717–8729, 2014. 39

[126] B. Acemioğlu, M. Arık, H. Efeoğlu, and Y. Onganer, "Solvent effect on the ground and excited state dipole moments of fluorescein," *Journal of Molecular Structure: THEOCHEM*, vol. 548, no. 1-3, pp. 165–171, 2001. 39

[127] J. He and J. S. Chen, "The solvatochromic materials: A progress review," in *Materials Science Forum*, Trans Tech Publ, vol. 914, 2018, pp. 182–192. 39

[128] S. Nigam and S. Rutan, "Principles and applications of solvatochromism," *Applied Spectroscopy*, vol. 55, no. 11, p. 362, 2001. 39

[129] T. Gong, P. Li, Q. Sui, L.-J. Zhou, N.-N. Yang, and E.-Q. Gao, "Switchable ferro-, ferri-, and antiferromagnetic states in a piezo-and hydrochromic metal–organic framework," *Inorganic Chemistry*, vol. 57, no. 12, pp. 6791–6794, 2018. 39

[130] S. Hu, J. Zhang, S. Chen, J. Dai, and Z. Fu, "Efficient ultraviolet light detector based on a crystalline viologen-based metal–organic framework with rapid visible color change under irradiation," *ACS applied materials & interfaces*, vol. 9, no. 46, pp. 39 926–39 929, 2017. 39

[131] N. L. Strutt, D. Fairen-Jimenez, J. Iehl, M. B. Lalonde, R. Q. Snurr, O. K. Farha, J. T. Hupp, and J. F. Stoddart, "Incorporation of an a1/a2-difunctionalized pillar [5] arene into a metal–organic framework," *Journal of the American Chemical Society*, vol. 134, no. 42, pp. 17 436–17 439, 2012. 39

[132] K. Wang, S. Huang, Y. Zhang, S. Zhao, H. Zhang, and Y. Wang, "Multicolor fluorescence and electroluminescence of an ict-type organic solid tuned by modulating the accepting nature of the central core," *Chemical Science*, vol. 4, no. 8, pp. 3288–3293, 2013. 39

[133] J. Zhang, J. Chen, B. Xu, L. Wang, S. Ma, Y. Dong, B. Li, L. Ye, and W. Tian, "Remarkable fluorescence change based on the protonation–deprotonation control in organic crystals," *Chemical Communications*, vol. 49, no. 37, pp. 3878–3880, 2013. 39

[134] X. Y. Shen, Y. J. Wang, E. Zhao, W. Z. Yuan, Y. Liu, P. Lu, A. Qin, Y. Ma, J. Z. Sun, and B. Z. Tang, "Effects of substitution with donor–acceptor groups on the properties of tetraphenylethene trimer: Aggregation-induced emission, solvatochromism, and mechanochromism," *The Journal of Physical Chemistry C*, vol. 117, no. 14, pp. 7334–7347, 2013. 39

[135] J. Chen, S. Ma, J. Zhang, L. Wang, L. Ye, B. Li, B. Xu, and W. Tian, "Proton-triggered hypsochromic luminescence in 1, 1-(2, 5-distyryl-1, 4-phenylene) dipiperidine," *The Journal of Physical Chemistry Letters*, vol. 5, no. 16, pp. 2781–2784, 2014. 39

[136] Y. Dong, J. Zhang, X. Tan, L. Wang, J. Chen, B. Li, L. Ye, B. Xu, B. Zou, and W. Tian, "Multi-stimuli responsive fluorescence switching: The reversible piezochromism and protonation effect of a divinylanthracene derivative," *Journal of Materials Chemistry C*, vol. 1, no. 45, pp. 7554–7559, 2013. 39

[137] X. J. Zhou, C. Chen, C. X. Ren, J. K. Sun, and J. Zhang, "Tunable solid-state photoluminescence based on proton-triggered structural transformation of 4,4'-bipyridinium derivative," *Journal of Materials Chemistry C*, vol. 1, no. 4, pp. 744–750, 2012. 39

[138] S. Ma, J. Zhang, Y. Liu, J. Qian, B. Xu, and W. Tian, "Direct observation of the symmetrical and asymmetrical protonation states in molecular crystals," *Journal of Physical Chemistry Letters*, vol. 8, no. 13, p. 3068, 2017. 39

[139] Z.-Z. Li, X.-D. Wang, and L.-S. Liao, "Luminescence-/morphology-modulation of organic microcrystals by a protonation process," *Journal of Materials Chemistry C*, vol. 5, no. 27, pp. 6661–6666, 2017. 39

[140] Z. Qin, Y. Wang, X. Lu, Y. Chen, J. Peng, and G. Zhou, "Multistimuli-responsive luminescence switching of pyrazine derivative based donor–acceptor–donor luminophores," *Chemistry–An Asian Journal*, vol. 11, no. 2, pp. 285–293, 2016. 39

[141] S. H. Wu, S. Wang, W. L. Fang, X. F. Guo, and H. Wang, "An exceptionally stable zr-based fluorescent metal–organic framework for highly selective detection of ph," *Analytical Methods*, vol. 11, no. 1, pp. 36–43, 2019. 39, 54

[142] Z.-Q. Shi, Z.-J. Guo, and H.-G. Zheng, "Two luminescent zn (ii) metal–organic frameworks for exceptionally selective detection of picric acid explosives," *Chemical Communications*, vol. 51, no. 39, pp. 8300–8303, 2015. 39, 50

[143] J. Ye, L. Zhao, R. F. Bogale, Y. Gao, X. Wang, X. Qian, S. Guo, J. Zhao, and G. Ning, "Highly selective detection of 2, 4, 6-trinitrophenol and cu2+ ions based on a fluorescent cadmium–pamoate metal–organic framework," *Chemistry–A European Journal*, vol. 21, no. 5, pp. 2029–2037, 2015. 39

[144] B. Gole, A. K. Bar, and P. S. Mukherjee, "Fluorescent metal–organic framework for selective sensing of nitroaromatic explosives," *Chemical Communications*, vol. 47, no. 44, pp. 12 137–12 139, 2011. 39

[145] M. D. Allendorf, C. A. Bauer, R. K. Bhakta, and R. J. T. Houk, "Luminescent metal-organic frameworks," *Chemical Society Reviews*, vol. 38, no. 5, pp. 1330–1352, 2009. 40

[146] D. Yan, G. O. Lloyd, A. Delori, W. Jones, and X. Duan, "Tuning fluorescent molecules by inclusion in a metal–organic framework: An experimental and computational study," *ChemPlusChem*, vol. 77, no. 12, pp. 1112–1118, 2012. 40

[147] A. Gładysiak, T. N. Nguyen, S. L. Anderson, P. G. Boyd, R. G. Palgrave, J. Bacsa, B. Smit, M. J. Rosseinsky, and K. C. Stylianou, "Shedding light on the protonation states and location of protonated n atoms of adenine in metal–organic frameworks," *Inorganic chemistry*, vol. 57, no. 4, pp. 1888–1900, 2018. 40

[148] S. I. Vagin, A. K. Ott, S. D. Hoffmann, D. Lanzinger, and B. Rieger, "Synthesis and properties of (triptycenedicarboxylatio) zinc coordination networks," *Chemistry–A European Journal*, vol. 15, no. 23, pp. 5845–5853, 2009. 40, 50

[149] L. R. Snyder, "Classification of the solvent properties of common liquids," *Journal of Chromatography A*, vol. 92, no. 2, pp. 223–230, 1974. 44

[150] T. Zuehlsdorff, P. Haynes, M. Payne, and N. Hine, "Predicting solvatochromic shifts and colours of a solvated organic dye: The example of nile red," *The Journal of Chemical Physics*, vol. 146, no. 12, p. 124 504, 2017. 44

[151] J. Qi, D. Liu, X. Liu, S. Guan, F. Shi, H. Chang, H. He, and G. Yang, "Fluorescent ph sensors for broad-range ph measurement based on a single fluorophore," *Analytical chemistry*, vol. 87, no. 12, pp. 5897–5904, 2015. 45

[152] K.-K. Yu, W.-B. Tseng, M.-J. Wu, A. S. K. K. Alagarsamy, W.-L. Tseng, and P.-C. Lin, "Polyadenosine-based fluorescent probe for reversible ph sensing based on protonated adenine-adenine base pairs: Applications to sensing of enzyme-substrate system and enzymatic logic gates," *Sensors and Actuators B: Chemical*, vol. 273, pp. 681–688, 2018. 45

[153] S. Brasselet and W. Moerner, "Fluorescence behavior of single-molecule ph-sensors," *Single Molecules*, vol. 1, no. 1, pp. 17–23, 2000. 45

[154] J. Tomasi, B. Mennucci, and R. Cammi, "Quantum mechanical continuum solvation models," *Chemical reviews*, vol. 105, no. 8, pp. 2999–3094, 2005. 47

[155] E. R. Batista and R. L. Martin, *Natural transition orbitals*. Encyclopedia of Computational Chemistry, 2004. 48

[156] D. Yan, R. Gao, M. Wei, S. Li, J. Lu, D. G. Evans, and X. Duan, "Mechanochemical synthesis of a fluorenone-based metal organic framework with polarized fluorescence: An experimental and computational study," *Journal of Materials Chemistry C*, vol. 1, no. 5, pp. 997–1004, 2013. 52

[157] J. Estager, P. Nockemann, K. R. Seddon, M. Swadźba-Kwaśny, and S. Tyrrell, "Validation of speciation techniques: A study of chlorozincate (ii) ionic liquids," *Inorganic Chemistry*, vol. 50, no. 11, pp. 5258–5271, 2011. 52

[158] W. Hoffmüller, K. Polborn, and W. Beck, "Metal complexes of biologically important ligands, cxix. a tetrahedral zinc complex (l-tert-leucine)$\tilde{2}$zncl$\tilde{2}$ of carboxylate coordinated l-tert-leucine in the zwitterionic form," *ZEITSCHRIFT FUR NATURFORSCHUNG B*, vol. 54, no. 6, pp. 734–736, 1999. 53

[159] J.-Q. Liu, Z.-J. Jiang, Z.-H. Xu, and Y. Zhang, "Poly [chlorido [μ4-2, 2-(2-methyl-1h-benzimidazol-3-ium-1, 3-diyl) diacetato] zinc]," *Acta Crystallographica Section E: Structure Reports Online*, vol. 68, no. 6, pp. m751–m751, 2012. 53

[160] A. Monguzzi, M. Ballabio, N. Yanai, N. Kimizuka, D. Fazzi, M. Campione, and F. Meinardi, "Highly fluorescent metal–organic-framework nanocomposites for photonic applications," *Nano letters*, vol. 18, no. 1, pp. 528–534, 2018. 54

[161] B. H. Weigl and O. S. Wolfbeis, "Sensitivity studies on optical carbon dioxide sensors based on ion pairing," *Sensors Actuators B Chemical*, vol. 28, no. 2, pp. 151–156, 1995. 56

[162] T. Beuermann, D. Egly, D. Geoerg, K. I. Klug, W. Storhas, and F. J. Methner, "On-line carbon balance of yeast fermentations using miniaturized optical sensors," *Journal of Bioscience Bioengineering*, vol. 113, no. 3, pp. 399–405, 2012. 56

[163] E. Ljunggren and K. Bo, "Determination of total carbon dioxide in beer and soft drinks by gas diffusion and flow injection analysis," *Journal of Automatic Chemistry*, vol. 17, no. 3, pp. 105–108, 2007. 56

[164] D. Zhao, D. Miller, X. Xian, F. Tsow, and E. S. Forzani, "A novel real-time carbon dioxide analyzer for health and environmental applications," *Sensors and Actuators B: Chemical*, vol. 195, pp. 171–176, 2014. 56

[165] N. Stafford, "Future crops: The other greenhouse effect," *Nature*, vol. 448, no. 7153, pp. 526–528, 2007. 56

[166] C. Descoins, M. Mathlouthi, M. L. Moual, and J. Hennequin, "Carbonation monitoring of beverage in a laboratory scale unit with on-line measurement of dissolved co_2," *Food Chemistry*, vol. 95, no. 4, pp. 541–553, 2006. 56

[167] Z. Dai, H. Viswanathan, J. Fessenden-Rahn, R. Middleton, F. Pan, W. Jia, S.-Y. Lee, B. McPherson, W. Ampomah, and R. Grigg, "Uncertainty quantification for co_2 sequestration and enhanced oil recovery," *Energy Procedia*, vol. 63, pp. 7685–7693, 2014. 56

[168] K. Wetchakun, T. Samerjai, N. Tamaekong, C. Liewhiran, C. Siriwong, V. Kruefu, A. Wisitsoraat, A. Tuantranont, and S. Phanichphant, "Semiconducting metal oxides as sensors for environmentally hazardous gases," *Sensors and Actuators B: Chemical*, vol. 160, no. 1, pp. 580–591, 2011. 56

[169] T. Manuccia and J. Eden, "Infrared optical measurement of blood gas concentrations and fiber optic catheter.," DEPARTMENT OF THE NAVY WASHINGTON DC, Tech. Rep., 1985. 56

[170] Z. Liu, C. Zheng, C. Chen, H. Xie, Q. Ren, W. Ye, Y. Wang, and F. K. Tittel, "A near-infrared carbon dioxide sensor system using a compact folded optical structure for deep-sea natural gas hydrate exploration," *Analytical Methods*, vol. 10, no. 39, pp. 4838–4844, 2018. 56

[171] C. S. Chu and Y. L. Lo, "Highly sensitive and linear optical fiber carbon dioxide sensor based on sol-gel matrix doped with silica particles and hpts," *Sensors Actuators B Chemical*, vol. 143, no. 1, pp. 205–210, 2009. 56

[172] C.-S. Chu and J.-J. Syu, "Optical sensor for dual sensing of oxygen and carbon dioxide based on sensing films coated on filter paper," *Applied Optics*, vol. 56, no. 4, pp. 1225–1231, 2017. 56

[173] R. N. Dansby-Sparks, J. Jin, S. J. Mechery, U. Sampathkumaran, and Z. L. Xue, "Fluorescent-dye-doped sol-gel sensor for highly sensitive carbon dioxide gas detection below atmospheric concentrations," *Analytical Chemistry*, vol. 82, no. 2, pp. 593–600, 2010. 56

[174] S. Schutting, S. M. Borisov, and I. Klimant, "Diketo-pyrrolo-pyrrole dyes as new colorimetric and fluorescent ph indicators for optical carbon dioxide sensors," *Analytical Chemistry*, vol. 85, no. 6, pp. 3271–3279, 2013. 56

[175] "A benzobisimidazolium-based fluorescent and colorimetric chemosensor for co_2," *Journal of the American Chemical Society*, vol. 134, no. 43, pp. 17 846–17 849, 2012. 56, 58

[176] Y. Amao and N. Nakamura, "Optical co_2 sensor with the combination of colorimetric change of α-naphtholphthalein and internal reference fluorescent porphyrin dye," *Sensors and Actuators B: Chemical*, vol. 100, no. 3, pp. 347–351, 2004. 56

[177] R. Ali, S. M. Saleh, R. J. Meier, H. A. Azab, I. I. Abdelgawad, and O. S. Wolfbeis, "Upconverting nanoparticle based optical sensor for carbon dioxide," *Sensors and Actuators B Chemical*, vol. 150, no. 1, pp. 126–131, 2010. 56, 58

[178] Y. Shimizu and N. Yamashita, "Solid electrolyte co_2 sensor using nasicon and perovskite-type oxide electrode," *Sensors and Actuators B: Chemical*, vol. 64, no. 1-3, pp. 102–106, 2000. 56

[179] T.-W. Kim, J.-W. Kim, S.-M. Lee, and C.-O. Park, "Humidity effects on the initial stabilization behavior of a solid electrochemical co_2 sensor," *Sensors and Actuators B: Chemical*, vol. 295, pp. 65–69, 2019. 56

[180] J. W. Severinghaus, "First electrodes for blood po_2 and pco_2 determination," *Journal of Applied Physiology*, vol. 97, no. 5, pp. 1599–1600, 2004. 56

[181] J. Boudaden, A. Klumpp, I. Eisele, and C. Kutter, "Smart capacitive co_2 sensor," in *2016 IEEE SENSORS*, IEEE, 2016, pp. 1–3. 56

[182] M. Struzik, I. Garbayo, R. Pfenninger, and J. L. Rupp, "A simple and fast electrochemical co_2 sensor based on $li_7la_3zr_2o_12$ for environmental monitoring," *Advanced Materials*, vol. 30, no. 44, p. 1 804 098, 2018. 56

[183] J. D. Suter, I. M. White, H. Zhu, and X. Fan, "Thermal characterization of liquid core optical ring resonator sensors," *Applied optics*, vol. 46, no. 3, pp. 389–396, 2007. 56

[184] J. Fernández-Sánchez, R. Cannas, S. Spichiger, R. Steiger, and U. E. Spichiger-Keller, "Optical co_2-sensing layers for clinical application based on ph-sensitive indicators incorporated into nanoscopic metal-oxide supports," *Sensors Actuators B Chemical*, vol. 128, no. 1, pp. 145–153, 2007. 57, 58

[185] Y. Ma, M. Cametti, Z. Džolić, and S. Jiang, "Aie-active bis-cyanostilbene-based organogels for quantitative fluorescence sensing of co_2 based on molecular recognition principles," *Journal of Materials Chemistry C*, vol. 6, no. 34, pp. 9232–9237, 2018. 57

[186] C. J. T. Robidillo, S. Wandelt, R. Dalangin, L. Zhang, H. Yu, A. Meldrum, R. E. Campbell, and J. G. Veinot, "Ratiometric detection of nerve agents by coupling complementary properties of silicon-based quantum dots and green fluorescent protein," *ACS applied materials & interfaces*, vol. 11, no. 36, pp. 33 478–33 488, 2019. 57

[187] D. D. Liana, B. Raguse, J. J. Gooding, and E. Chow, "Recent advances in paper-based sensors," *Sensors*, vol. 12, no. 9, pp. 11 505–11 526, 2012. 57

[188] M. Sher, R. Zhuang, U. Demirci, and W. Asghar, "Based analytical devices for clinical diagnosis: Recent advances in the fabrication techniques and sensing mechanisms," *Expert review of molecular diagnostics*, vol. 17, no. 4, pp. 351–366, 2017. 57

[189] Y. Chen, Y. Zilberman, P. Mostafalu, and S. R. Sonkusale, "Paper based platform for colorimetric sensing of dissolved nh_3 and co_2," *Biosensors Bioelectronics*, vol. 67, pp. 477–484, 2015. 57

[190] S. S. Razi, R. C. Gupta, R. Ali, S. K. Dwivedi, P. Srivastava, and A. Misra, "A new d–π–a type intramolecular charge transfer dyad system to detect f-: Anion induced co2 sensing," *Sensors and Actuators B: Chemical*, vol. 236, pp. 520–528, 2016. 57

[191] T. Tian, X. Chen, H. Li, Y. Wang, L. Guo, and L. Jiang, "Amidine-based fluorescent chemosensor with high applicability for detection of co_2: A facile way to "see" co_2," *Analyst*, vol. 138, no. 4, pp. 991–994, 2013. 57

[192] J. Sun, B. Ye, G. Xia, X. Zhao, and H. Wang, "A colorimetric and fluorescent chemosensor for the highly sensitive detection of co_2 gas: Experiment and dft calculation," *Sensors and Actuators B: Chemical*, vol. 233, pp. 76–82, 2016. 57, 58

[193] X. Zhang, H. Mu, H. Li, Y. Zhang, M. An, X. Zhang, J. Yoon, and H. Yu, "Dual-channel sensing of co_2: Reversible solution-gel transition and gelation-induced fluorescence enhancement," *Sensors and Actuators B: Chemical*, vol. 255, pp. 2764–2778, 2018. 57

[194] H.-J. Li, S. K. Mellerup, X. Wang, and S. Wang, "D- π–a triarylboranes as reversible fluorescent probes for co2 and temperature," *Organic letters*, vol. 21, no. 8, pp. 2838–2842, 2019. 58

[195] M. Jang, S. Kang, and M. S. Han, "A simple turn-on fluorescent chemosensor for co_2 based on aggregation-induced emission: Application as a co2 absorbent screening method," *Dyes and Pigments*, vol. 162, pp. 978–983, 2019. 58

[196] Q. Xu, S. Lee, Y. Cho, M. H. Kim, J. Bouffard, and J. Yoon, "Polydiacetylene-based colorimetric and fluorescent chemosensor for the detection of carbon dioxide," *Journal of the American Chemical Society*, vol. 135, no. 47, pp. 17 751–17 754, 2013. 58

[197] R. K. Mishra, S. Vijayakumar, A. Mal, V. Karunakaran, J. C. Janardhanan, K. K. Maiti, V. K. Praveen, and A. Ajayaghosh, "Bimodal detection of carbon dioxide using fluorescent molecular aggregates," *Chemical Communications*, vol. 55, no. 43, pp. 6046–6049, 2019. 58

[198] X. Zhang, Y. Song, M. Liu, H. Li, H. Sun, M. Sun, and H. Yu, "Visual sensing of co_2 in air with a 3-position modified naphthalimide-derived organogelator based on a fluoride ion-induced strategy - sciencedirect," *Dyes and Pigments*, vol. 160, pp. 799–805, 2019. 58

[199] M.-H. Xie, W. Cai, X. Chen, R.-F. Guan, L.-M. Wang, G.-H. Hou, X.-G. Xi, Q.-F. Zhang, X.-L. Yang, and R. Shao, "Novel co_2 fluorescence turn-on quantification based on a dynamic aie-active metal–organic framework," *ACS applied materials & interfaces*, vol. 10, no. 3, pp. 2868–2873, 2018. 58

[200] P. K. Contreras-Gutierrez, S. Medina-Rodrıguez, A. L. Medina-Castillo, J. F. Fernandez-Sanchez, and A. Fernandez-Gutierrez, "A new highly sensitive and versatile optical sensing film for controlling co_2 in gaseous and aqueous media," *Sensors and Actuators B: Chemical*, vol. 184, pp. 281–287, 2013. 58

[201] M. P. Zhuo, X. Y. Fei, Y. C. Tao, J. Fan, X. D. Wang, W. Xie, and L. S. Liao, "In-situ construction of 1d component-interchange organic core/shell microrods for multi-color continuous-variable optical waveguide," *ACS Applied Materials Interfaces*, 2019. 58

[202] K. Shen, L. Qin, and H.-G. Zheng, "Diverse structures of metal–organic frameworks via a side chain adjustment: Interpenetration and gas adsorption," *Dalton Transactions*, vol. 45, no. 41, pp. 16 205–16 210, 2016. 58

[203] M.-J. Chang, Y. Ai, L. Zhang, F. Gao, and H.-L. Zhang, "Hierarchical patterning of organic molecules for self-referenced vapor sensing," *Journal of Materials Chemistry*, vol. 22, no. 16, pp. 7704–7707, 2012. 58

[204] H. Wang, S. I. Vagin, S. Lane, W. Lin, V. Shyta, W. R. Heinz, C. Van Dyck, A. J. Bergren, K. Gardner, B. Rieger, *et al.*, "Metal–organic framework with color-switching and strongly polarized emission," *Chemistry of Materials*, vol. 31, no. 15, pp. 5816–5823, 2019. 58, 64, 79

[205] Y. Iwase, K. Kamada, K. Ohta, and K. Kondo, "Synthesis and photophysical properties of new two-photon absorption chromophores containing a diacetylene moiety as the central π-bridge," *Journal of Materials Chemistry*, vol. 13, no. 7, pp. 1575–1581, 2003. 60

[206] "Global monitoring laboratory," Accessed: 2022-06-06. 68

[207] G. Marinenko and W. Koch, "A critical review of measurement practices for the determination of ph and acidity of atmospheric precipitation," *Environment international*, vol. 10, no. 4, pp. 315–319, 1984. 71

[208] J. Bourilkov, M. Belz, W. J. Boyle, and K. T. Grattan, "Electrical ph control in aqueous solutions," vol. 3538, pp. 268–277, 1999. 71

[209] L. S. Evans, G. R. Hendrey, G. J. Stensland, D. W. Johnson, and A. Francis, "Acidic precipitation: Considerations for an air quality standard," *Water, Air, and Soil Pollution*, vol. 16, no. 4, pp. 469–509, 1981. 71

[210] R. Badugu, Y. Kostov, G. Rao, and L. Tolosa, "Development and application of an excitation ratiometric optical ph sensor for bioprocess monitoring.," *Biotechnology Progress*, vol. 24, no. 6, pp. 1393–1401, 2010. 71

[211] X. Lian and B. Yan, "Phosphonate mofs composite as off–on fluorescent sensor for detecting purine metabolite uric acid and diagnosing hyperuricuria," *Inorganic Chemistry*, vol. 56, no. 12, pp. 6802–6808, 2017. 71, 73

[212] O. S. Andersen, K. Engel, K. Jörgensen, and P. Astrup, "A micro method for determination of ph, carbon dioxide tension, base excess and standard bicarbonate in capillary blood," *Scandinavian journal of clinical and laboratory investigation*, vol. 12, no. 2, pp. 172–176, 1960. 71

[213] C. Toumazou, L. M. Shepherd, S. C. Reed, G. I. Chen, A. Patel, D. M. Garner, C.-J. A. Wang, C.-P. Ou, K. Amin-Desai, P. Athanasiou, *et al.*, "Simultaneous dna amplification and detection using a ph-sensing semiconductor system," *Nature methods*, vol. 10, no. 7, pp. 641–646, 2013. 71

[214] S. G. Liu, D. Luo, N. Li, W. Zhang, J. L. Lei, N. B. Li, and H. Q. Luo, "Water-soluble nonconjugated polymer nanoparticles with strong fluorescence emission for selective and sensitive detection of nitro-explosive picric acid in aqueous medium," *ACS Applied Materials & Interfaces*, vol. 8, no. 33, pp. 21 700–21 709, 2016. 71

[215] Y. Lei, N. Luo, X. Yan, Y. Zhao, G. Zhang, and Y. Zhang, "A highly sensitive electrochemical biosensor based on zinc oxide nanotetrapods for l-lactic acid detection.," *Nanoscale*, vol. 4, no. 11, pp. 3438–3443, 2012. 71

[216] Y. Chen, C. Zhu, Z. Yang, J. Chen, and Z. Guo, "A ratiometric fluorescent probe for rapid detection of hydrogen sulfide in mitochondria," *Angewandte Chemie International Edition*, vol. 52, no. 6, pp. 1688–1691, 2013. 71

[217] F. Tahernejad-Javazmi, M. Shabani-Nooshabadi, and H. Karimi-Maleh, "3d reduced graphene oxide/feni3-ionic liquid nanocomposite modified sensor; an electrical synergic effect for development of tert-butylhydroquinone and folic acid sensor," *Composites Part B: Engineering*, vol. 172, pp. 666–670, 2019. 71, 73

[218] B. Dinesh, R. Saraswathi, and A. S. Kumar, "Water based homogenous carbon ink modified electrode as an efficient sensor system for simultaneous detection of ascorbic acid, dopamine and uric acid," *Electrochimica Acta*, vol. 233, pp. 92–104, 2017. 71, 73

[219] A. Castanheira, M. B. Dos Santos, L. Rodriguez-Lorenzo, R. Queirós, and B. Espiña, "A novel microfluidic system for the sensitive and cost-effective detection of okadaic acid in mussels," *Analyst*, vol. 146, no. 8, pp. 2638–2645, 2021. 72, 73, 86

[220] L.-L. Yang, S.-Y. Zou, Y.-H. Fu, W. Li, X.-P. Wen, P.-Y. Wang, Z.-C. Wang, G.-P. Ouyang, Z. Li, and S. Yang, "Highly selective and sensitive detection of biogenic defense phytohormone salicylic acid in living cells and plants using a novel and viable rhodamine-functionalized fluorescent probe," *Journal of Agricultural and Food Chemistry*, vol. 68, no. 15, pp. 4285–4291, 2020. 72, 73, 86

[221] S. Kumar, R. Singh, Q. Yang, S. Cheng, B. Zhang, and B. K. Kaushik, "Highly sensitive, selective and portable sensor probe using germanium-doped photosensitive optical fiber for ascorbic acid detection," *IEEE Sensors Journal*, vol. 21, no. 1, pp. 62–70, 2020. 72, 73

[222] S. Amin, A. Tahira, A. Solangi, R. Mazzaro, Z. H. Ibupoto, and A. Vomiero, "A sensitive enzyme-free lactic acid sensor based on nio nanoparticles for practical applications," *Analytical Methods*, vol. 11, no. 28, pp. 3578–3583, 2019. 73, 86

[223] Z. Wei, M. Li, H. Zeng, and X. Zhang, "Integrated nanoextraction and colorimetric reactions in surface nanodroplets for combinative analysis," *Analytical Chemistry*, vol. 92, no. 18, pp. 12 442–12 450, 2020. 72, 73, 80, 82

[224] P. Li, Y. Hong, H. Feng, and S. F. Li, "An efficient "off–on" carbon nanoparticle-based fluorescent sensor for recognition of chromium (vi) and ascorbic acid based on the inner filter effect," *Journal of Materials Chemistry B*, vol. 5, no. 16, pp. 2979–2988, 2017. 73

[225] K. Bauri, B. Saha, J. Mahanti, and P. De, "A nonconjugated macromolecular luminogen for speedy, selective and sensitive detection of picric acid in water," *Polymer Chemistry*, vol. 8, no. 46, pp. 7180–7187, 2017. 73

[226] T. Bera and J. Fang, "Optical detection of lithocholic acid with liquid crystal emulsions," *Langmuir*, vol. 29, no. 1, pp. 387–392, 2013. 73

[227] S. K. Tammina and Y. Yang, "Highly sensitive and selective detection of 4-nitrophenol, and on-off-on fluorescence sensor for cr (vi) and ascorbic acid detection by glucosamine derived n-doped carbon dots," *Journal of Photochemistry and Photobiology A: Chemistry*, vol. 387, p. 112 134, 2020. 73

[228] L. Kong, Y. Gan, T. Liang, L. Zhong, Y. Pan, D. Kirsanov, A. Legin, H. Wan, and P. Wang, "A novel smartphone-based cd-spectrometer for high sensitive and cost-effective colorimetric detection of ascorbic acid," *Analytica Chimica Acta*, vol. 1093, pp. 150–159, 2020. 73

[229] Y. Q. Sun, Y. Cheng, and X. B. Yin, "Dual-ligand lanthanide metal-organic framework for sensitive ratiometric fluorescence detection of hypochlorous acid," *Analytical Chemistry*, vol. 93, no. 7, pp. 3559–3566, 2021. 73

[230] X. Huo, X. Wang, R. Yang, Z. Li, Y. Sun, L. Qu, and H. Zeng, "A novel fluorescent probe for highly selective and sensitive detection of hypobromous acid in arthritis model mice," *Sensors and Actuators B: Chemical*, vol. 315, p. 128 125, 2020. 73

[231] X. Chen, C. Sun, Y. Liu, L. Yu, K. Zhang, A. M. Asiri, H. M. Marwani, H. Tan, Y. Ai, X. Wang, *et al.*, "All-inorganic perovskite quantum dots $cspbx_3$ (br/i) for highly sensitive and selective detection of explosive picric acid," *Chemical Engineering Journal*, vol. 379, p. 122 360, 2020. 73

[232] S. Kadian and G. Manik, "A highly sensitive and selective detection of picric acid using fluorescent sulfur-doped graphene quantum dots," *Luminescence*, vol. 35, no. 5, pp. 763–772, 2020. 73

[233] Q.-b. Wang, C.-j. Zhang, H. Yu, X. Zhang, Q. Lu, J.-s. Yao, and H. Zhao, "The sensitive "turn-on" fluorescence platform of ascorbic acid based on conjugated polymer nanoparticles," *Analytica Chimica Acta*, vol. 1097, pp. 153–160, 2020. 73

[234] W. A. Adeosun, A. M. Asiri, H. M. Marwani, and M. M. Rahman, "Enzymeless electrocatalytic detection of uric acid using polydopamine/polypyrrole copolymeric film," *ChemistrySelect*, vol. 5, no. 1, pp. 156–164, 2020. 73

[235] X. Li, J. Qiao, Y. Sun, Z. Li, and L. Qi, "Ligand-modulated synthesis of gold nanoclusters for sensitive and selective detection of folic acid," *Journal of Analytical Science and Technology*, vol. 12, no. 1, pp. 1–8, 2021. 73

[236] X.-T. Liu, T. Lin, C.-X. Zhang, and Q.-L. Wang, "A phosphonate coordination polymer with highly sensitive detection of ascorbic acid and the proton conductivity of its polymer composites," *Polyhedron*, vol. 178, p. 114 347, 2020. 73

[237] J. Comer and K. Tam, *Lipophilicity profiles: theory and measurement*. Wiley Online Library, 2001, pp. 275–304. 72

[238] J. B. You, D. Lohse, and X. Zhang, "Surface nanodroplet-based nanoextraction from sub-milliliter volumes of dense suspensions," *Lab on a Chip*, vol. 21, no. 13, pp. 2574–2585, 2021. 72

[239] A. Kalantarifard, A. Saateh, and C. Elbuken, "Label-free sensing in microdroplet-based microfluidic systems," *Chemosensors*, vol. 6, no. 2, p. 23, 2018. 72

[240] M. Li, B. Dyett, H. Yu, V. Bansal, and X. Zhang, "Functional femtoliter droplets for ultrafast nanoextraction and supersensitive online microanalysis," *Small*, vol. 15, no. 1, p. 1 804 683, 2019. 72, 86

[241] J. Qian, D. Yamada, Z. Wei, R. Yukisada, Y. Tagawa, J. M. Shaw, and X. Zhang, "One-step nanoextraction and ultrafast microanalysis based on nanodroplet formation in an evaporating ternary liquid microfilm," *Advanced Materials Technologies*, vol. 5, no. 2, p. 1 900 740, 2020. 74

[242] J. Meng, J. B. You, and X. Zhang, "Viscosity-mediated growth and coalescence of surface nanodroplets," *The Journal of Physical Chemistry C*, vol. 124, no. 23, pp. 12 476–12 484, 2020. 74

[243] M. Li, L. Bao, H. Yu, and X. Zhang, "Formation of multicomponent surface nanodroplets by solvent exchange," *The Journal of Physical Chemistry C*, vol. 122, no. 15, pp. 8647–8654, 2018. 74

[244] *Imagej*, `https://imagej.nih.gov/ij/`, Accessed: 2022-06-06. 75

[245] M. Dołowy and A. Pyka, "Lipophilicity study of salicylic and acetylsalicylic acids using both experimental and calculations methods," *Journal of Liquid Chromatography & Related Technologies*, vol. 38, no. 4, pp. 485–491, 2015. 80, 83, 84

[246] Y. Xiang, Z. Yuan, S. Wang, and A. Fan, "Effects of flow rate and fuel/air ratio on propagation behaviors of diffusion h2/air flames in a micro-combustor," *Energy*, vol. 179, pp. 315–322, 2019. 81

[247] V. Kumar, M. Paraschivoiu, and K. Nigam, "Single-phase fluid flow and mixing in microchannels," *Chemical Engineering Science*, vol. 66, no. 7, pp. 1329–1373, 2011. 81

[248] M. Polakovic, T. Gorner, F. Villiéras, P. de Donato, and J. L. Bersillon, "Kinetics of salicylic acid adsorption on activated carbon," *Langmuir*, vol. 21, no. 7, pp. 2988–2996, 2005. 83

[249] J. M. Delgado, "Experimental values of diffusion coefficients of organic compounds in water," vol. 273, pp. 132–137, 2008. 83

[250] F. Ye, H. Jensen, S. W. Larsen, A. Yaghmur, C. Larsen, and J. Østergaard, "Measurement of drug diffusivities in pharmaceutical solvents using taylor dispersion analysis," *Journal of pharmaceutical and biomedical analysis*, vol. 61, pp. 176–183, 2012. 83

[251] W. N. Charman, C. Lai, B. C. Finnin, and B. L. Reed, "Self-association of nicotinamide in aqueous solution: Mass transport, freezing-point depression, and partition coefficient studies," *Pharmaceutical Research*, vol. 8, no. 9, pp. 1144–1150, 1991. 87

[252] K. B. Lodge and E. J. Egyepong, "Evidence for self-association of non-ionic and other organic solutes in liquid phases comprising 1-octanol and water," *The Journal of Physical Chemistry A*, vol. 114, no. 15, pp. 5132–5140, 2010. 87

[253] M. C. Sicilia, A. Niño, and C. Muñoz-Caro, "Mechanism of pyridine protonation in water clusters of increasing size," *The Journal of Physical Chemistry A*, vol. 109, no. 37, pp. 8341–8347, 2005. 87

[254] A. P. Kalra, B. B. Eakins, S. I. Vagin, H. Wang, S. D. Patel, P. Winter, M. Aminpour, J. D. Lewis, V. Rezania, K. Shankar, *et al.*, "A nanometric probe of the local proton concentration in microtubule-based biophysical systems," *Nano letters*, 2021. 90

Appendix A

A metal-organic framework with color-switching and strongly polarized emission: Supplemental information

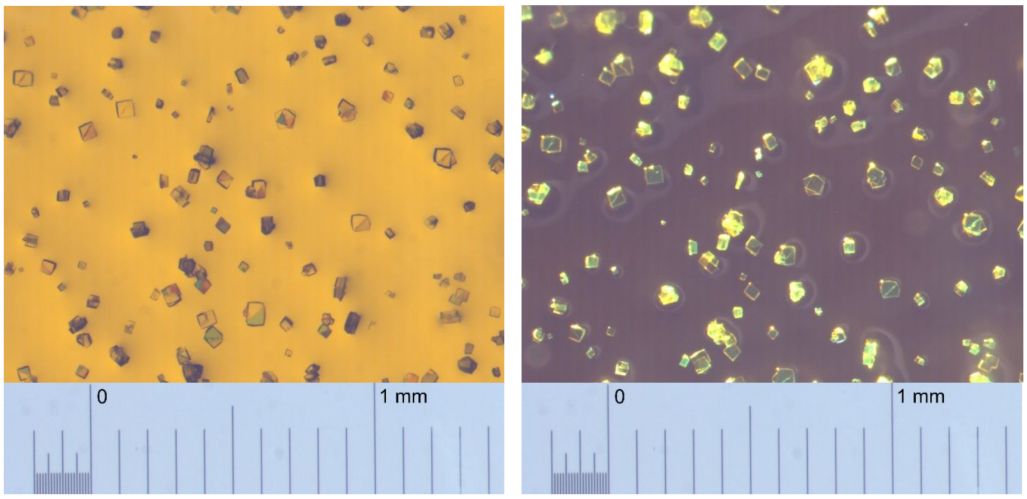

Figure A.1: Crystals of TDC-MOF-8 formed in reaction of 4 mM solution of $Zn(NO_3)_2$ in DMF with equimolar amounts of H_2TDC and np-P4VB in presence of 3% (w/w) acetic acid at 70^{o}C. Left - in transmitted polarized light mode; right – under incident non-polarized illumination. The right picture is slightly shifted down about 1/5 from the left picture. Reprinted with permission from Chem. Mater. 2019, 31, 15, 5816–5823. Copyright 2019 American Chemical Society.

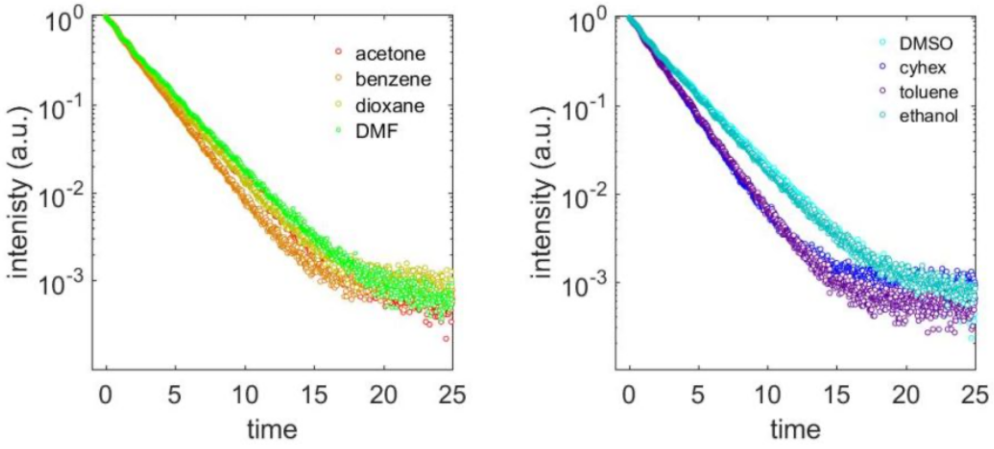

Figure A.2: Decay dynamics for np-P4VB in various solvents (listed in the legends). The x-axis unit is nanoseconds. Reprinted with permission from Chem. Mater. 2019, 31, 15, 5816–5823. Copyright 2019 American Chemical Society.

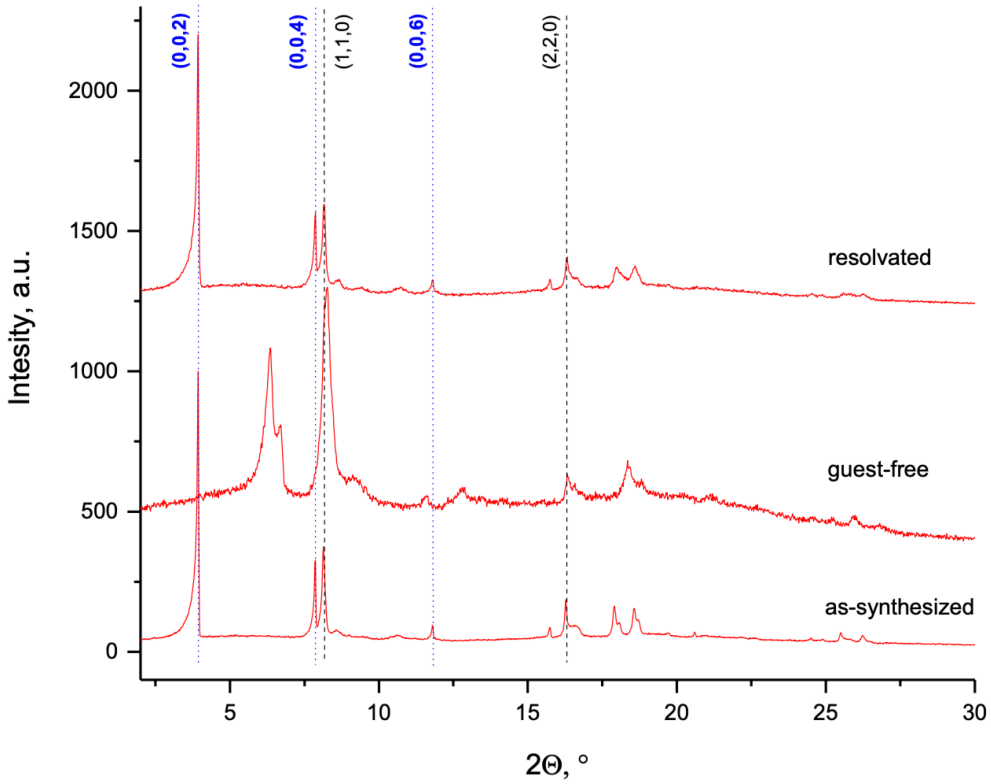

Figure A.3: PXRD-patterns of as-made TDC-MOF-8, guest-free TDC-MOF-8 before and after re-solvation with DEF. Reprinted with permission from Chem. Mater. 2019, 31, 15, 5816–5823. Copyright 2019 American Chemical Society.

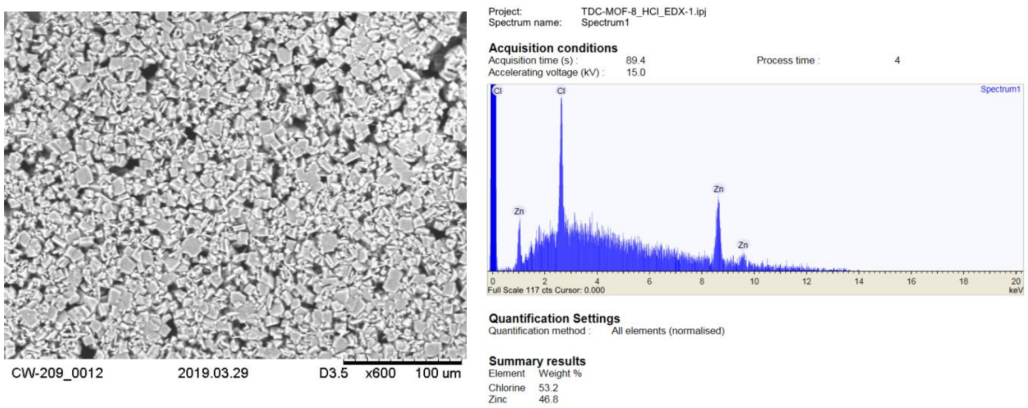

Figure A.4: SEM image of fine-crystalline sample of TDC-MOF-8 after treatment with HCl vapors and the results of EDX analysis. Reprinted with permission from Chem. Mater. 2019, 31, 15, 5816–5823. Copyright 2019 American Chemical Society.

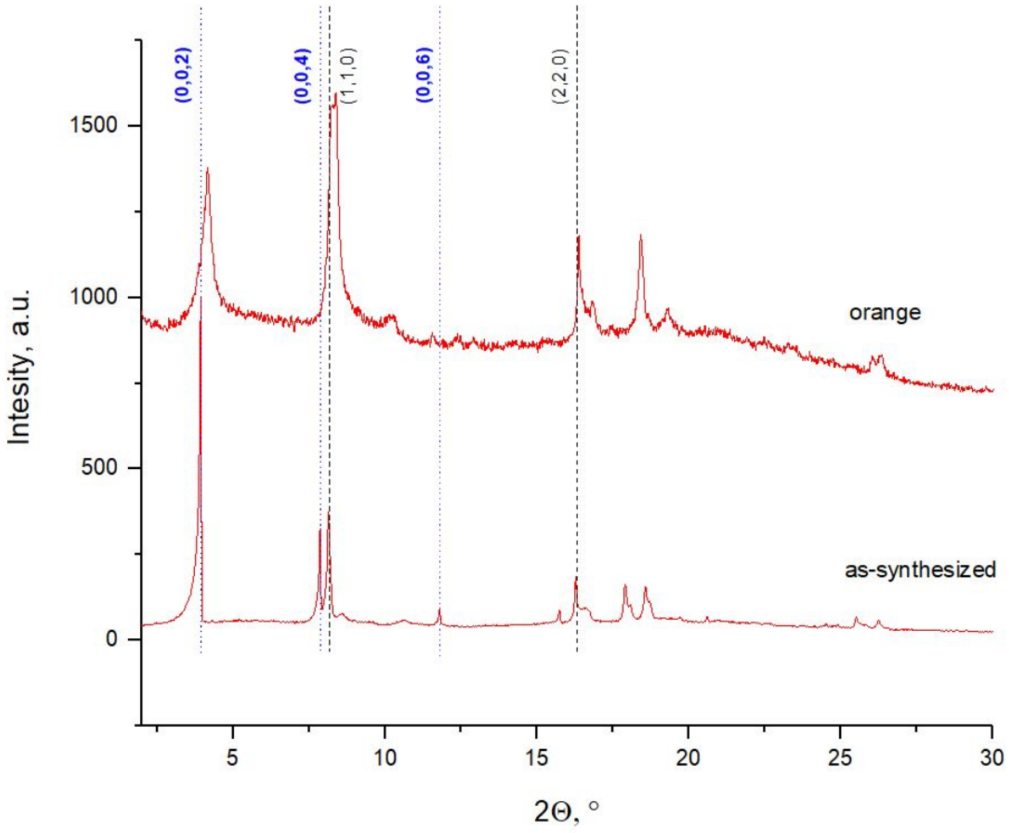

Figure A.5: PXRD patterns of the as-made TDC-MOF-8 before and after treatment with HCl vapors. Reprinted with permission from Chem. Mater. 2019, 31, 15, 5816–5823. Copyright 2019 American Chemical Society.

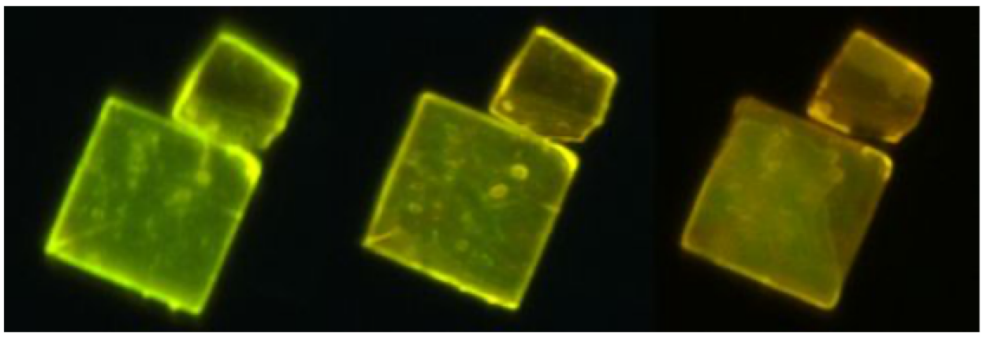

Figure A.6: Fluorescence image of two mof plates during fuming in HCl. The smaller one shows a larger color change in the same time frame. The larger square platelet has a side length of 33 μm. Reprinted with permission from Chem. Mater. 2019, 31, 15, 5816–5823. Copyright 2019 American Chemical Society.

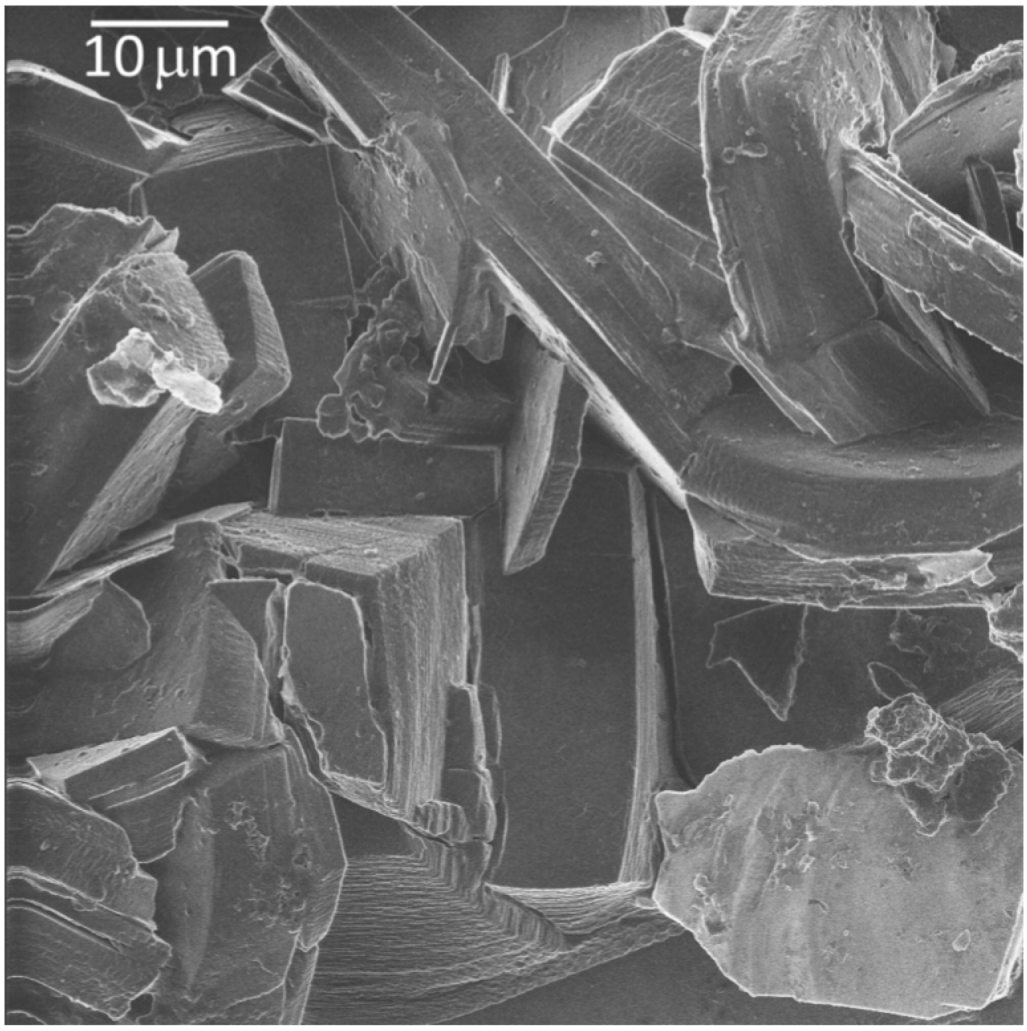

Figure A.7: HIM image of a cluster of MOFs. The layered wafer-like structure within the platelets can be observed. Reprinted with permission from Chem. Mater. 2019, 31, 15, 5816–5823. Copyright 2019 American Chemical Society.

Appendix B

An Ultra-Sensitive Fluorescent Paper-Based CO_2 Sensor: Supplemental information

Synthesis of 2,5-dimethoxy-1,4-bis[2-(4-pyridyl)ethenyl]benzene (me-P4VB) was performed according to literature procedure [Y. Iwase, K. Kamada, K. Ohta, K. Kondo, J. Mater. Chem. 2003, 13, 1575 – 1581]. The precipitate formed in the reaction was filtered off using Büchner funnel followed by washing with small portions of methanol. Re-crystallization was carried out by dissolving the crude material in DMSO at 100°C to get a saturated solution followed by cooling to room temperature.

Relative shifts (Δ, ppm) of different ^{1}H groups upon protonation of np-P4VB: α-Py-H (0.238), β-Py-H (0.594), -CH2=CH2- (0.364 and 0.340), Ar-H (0.165), O-CH2-(0.074), t-Bu(0.013).

Protonation of np-P4VB is an equilibrium reaction but it is driven to completeness upon addition of excess strong acid such as trifluoroacetic (TFA). The blue trace in Fig.B.5 corresponds to a twofold protonated form of np-P4VB and is characterized by a noticeable low-field shift of the signals in the aromatic region. Further addition of TFA does not cause any further shift of the signals.

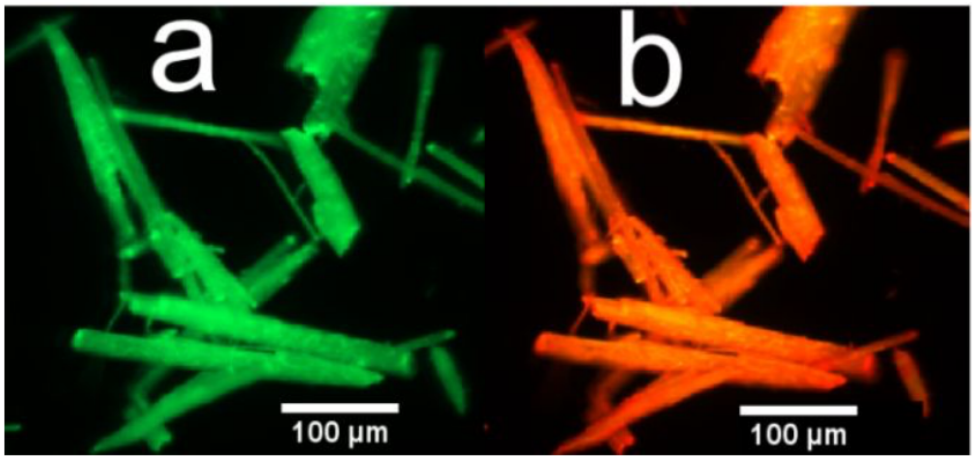

Figure B.1: (a) Fluorescence image of np-P4VB crystals under a violet LED. (b) When exposed to 12M HCl vapor, the color shifted from green to orange. Reprinted with permission from ACS Appl. Mater. Interfaces 2020, 12, 18, 20507–20513. Copyright 2020 American Chemical Society.

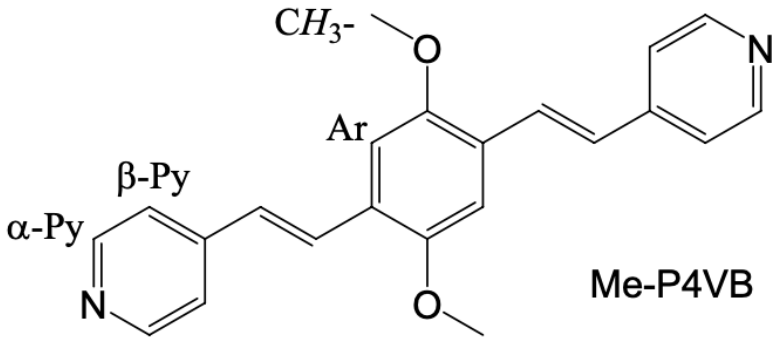

Figure B.2: Structure of Me-P4VB and the signals assignment in its NMR spectra. Reprinted with permission from ACS Appl. Mater. Interfaces 2020, 12, 18, 20507–20513. Copyright 2020 American Chemical Society.

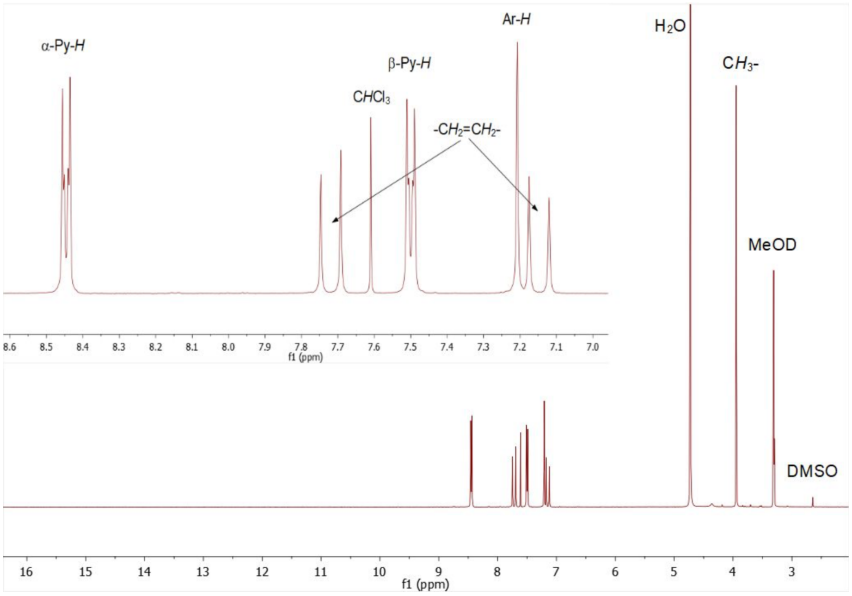

Figure B.3: ^{1}H NMR (300 MHz) spectrum of me-P4VB in $CDCl_3$/methanol-d4 mixture after recrystallization from DMSO. Reprinted with permission from ACS Appl. Mater. Interfaces 2020, 12, 18, 20507–20513. Copyright 2020 American Chemical Society.

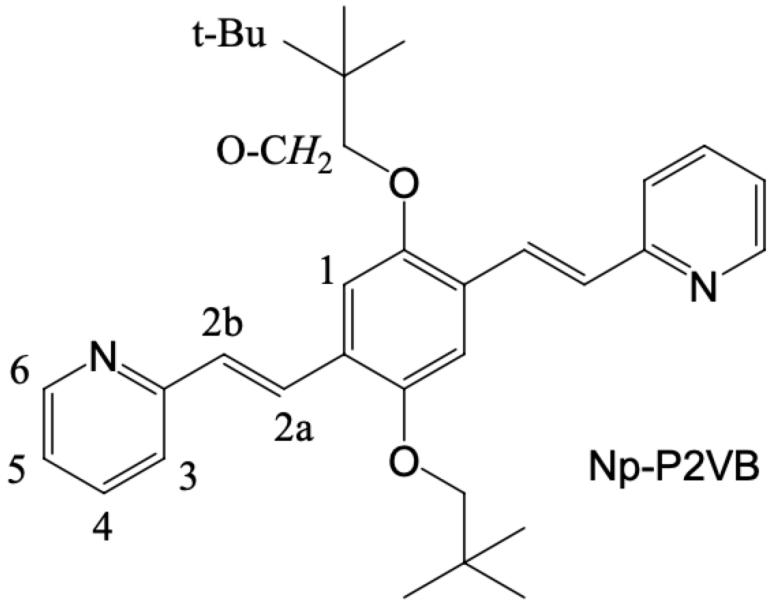

Figure B.4: Structure of np-P2VB and the signals assignment in its NMR spectra.

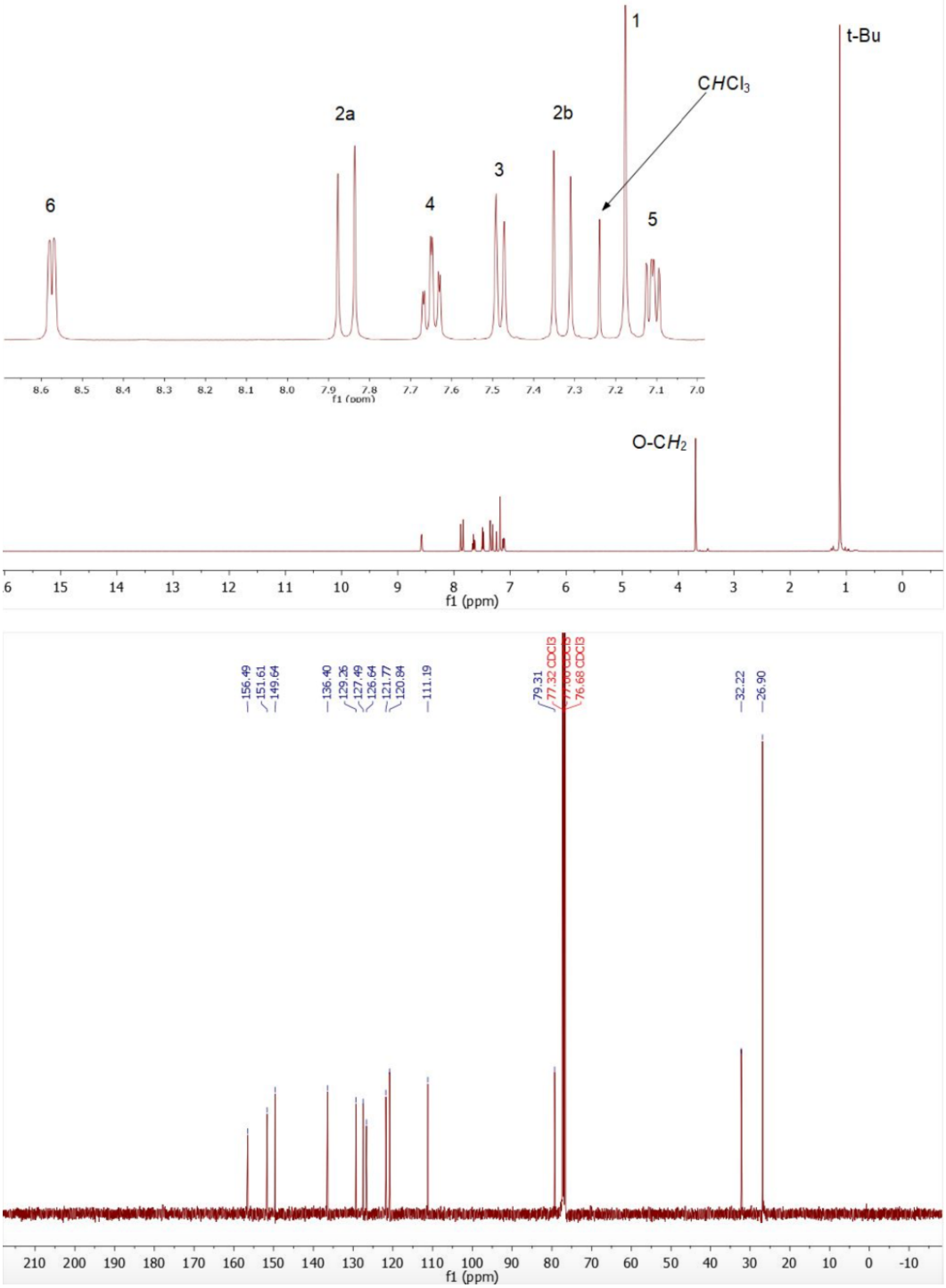

Figure B.5: ^{1}H NMR (400 MHz) /top/ and 13C NMR (100 MHz) /bottom/ spectra of np-P2VB in $CDCl_3$. Reprinted with permission from ACS Appl. Mater. Interfaces 2020, 12, 18, 20507–20513. Copyright 2020 American Chemical Society.

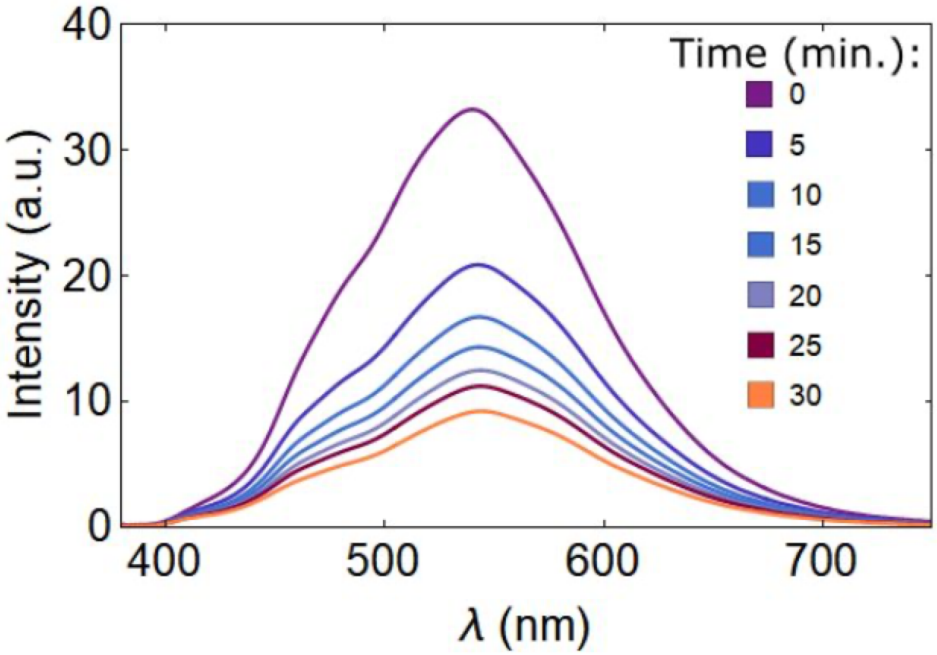

Figure B.6: Non-normalized Fluorescence spectra showing bleaching over 30 minutes 365-nm light exposure of np-P4VB-infused filter paper. Reprinted with permission from ACS Appl. Mater. Interfaces 2020, 12, 18, 20507–20513. Copyright 2020 American Chemical Society.

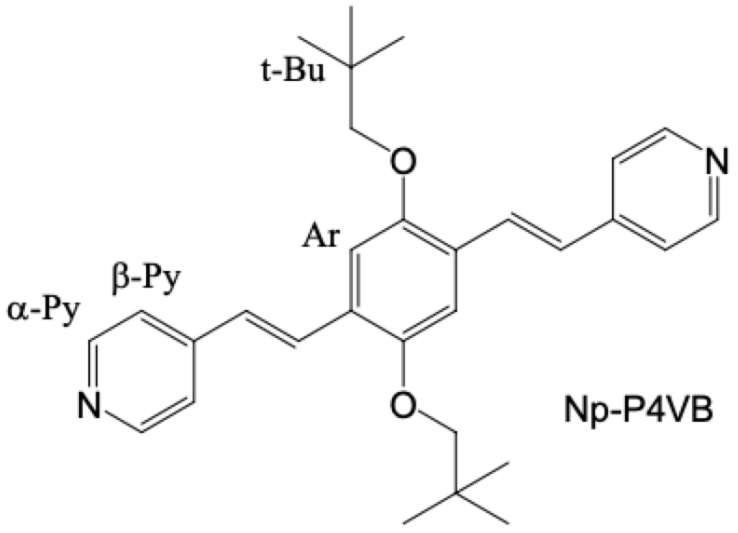

Figure B.7: Structure of np-P4VB and the signals assignment in its NMR spectra

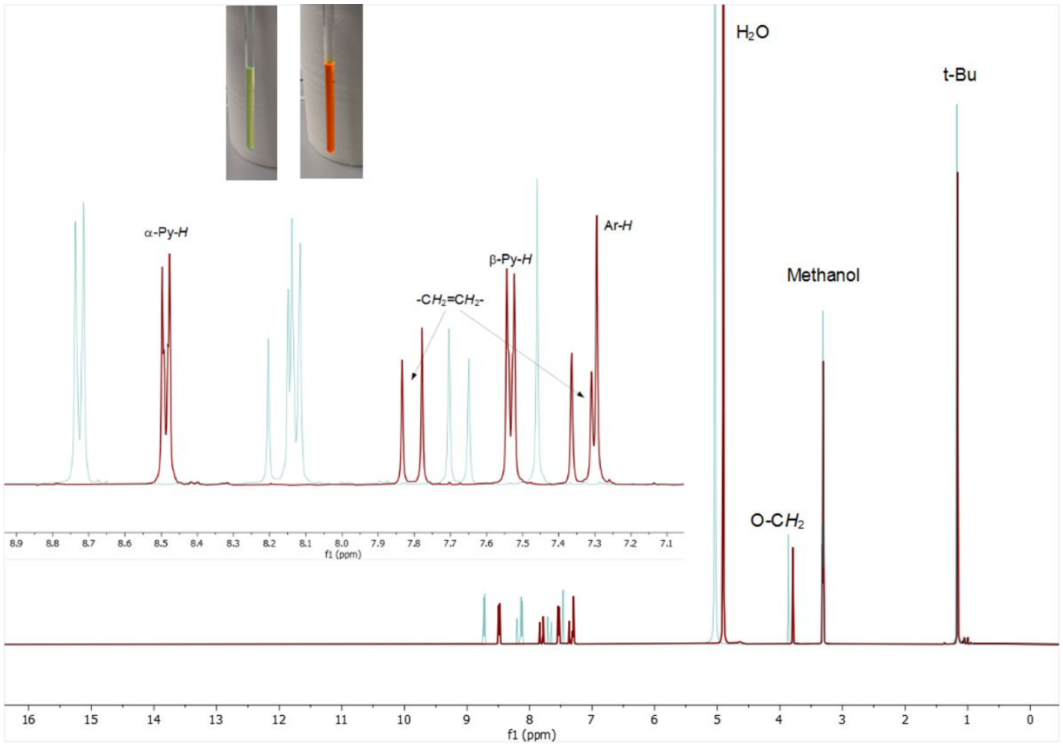

Figure B.8: ^{1}H NMR (300 MHz) spectra of np-P4VB in methanol-d4 before (red) and after addition of trifluoroacetic acid (blue) and the corresponding photographs (left to right) representing the colour of the solutions. Reprinted with permission from ACS Appl. Mater. Interfaces 2020, 12, 18, 20507–20513. Copyright 2020 American Chemical Society.

Table B.1: Sensing properties of the paper-based sensor. Reprinted with permission from ACS Appl. Mater. Interfaces 2020, 12, 18, 20507–20513. Copyright 2020 American Chemical Society.

Method	Sensing signal	LoD (%)	Response time (s)	Recovery time (s)	Ref.
Carbonic acid	Intensity	0.0006(calc), 0.01(means.)	<100	<100	This work

The low-field shift can be explained by a strong delocalization of the positive charge throughout the entire π-conjugated system as well as by an enhanced conjugation upon protonation. This is in line with our earlier quantum-chemical investigations [H. Wang, S. I. Vagin, S. Lane, W. Lin, V. Shyta, W. R. Heinz, C. Van Dyck, A. J. Bergren, K. Gardner, B. Rieger, A. Meldrum, Chem. Mater. 2019, 31, 5816-5823]. The strongest influence is observed for the vinylene doublets and β-Py multiplet. For weak acids, one can expect an incomplete protonation of np-P4VB also with excess acid. Protonated and non-protonated forms of np-P4VB are in equilibrium, and a fast proton exchange between molecules (relative to the NMR time scale) leads to the averaged chemical shifts from several species. This is the case for interaction of np-P4VB with CO_2-H_2O (certain amount of water is present in the deuterated solvent) shown below. Only the signals of protons that are outmost influenced by the protonation of pyridine end-groups indicate some detectable shift toward low field. This allows to conclude that most of the np-P4VB material remains non- protonated under the applied conditions. However, a higher degree of protonation by CO_2 can be achieved in diluted solutions and can be monitored by UV-Vis or PL spectroscopy.

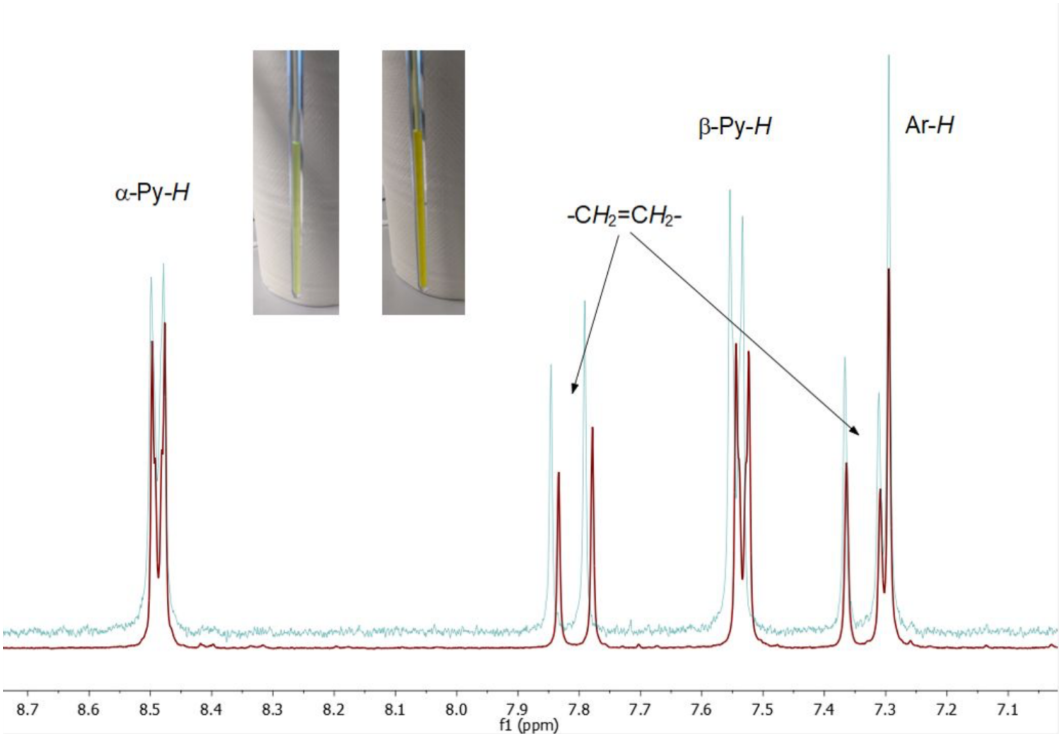

Figure B.9: ^{1}H NMR (300 MHz) spectra of ca. 10 mM np-P4VB (aromatic region) in methanol-d4 before (red) and after pressurizing with 9 bar CO_2 (blue) and the corresponding photographs (left to right) representing the colour of the solutions. Reprinted with permission from ACS Appl. Mater. Interfaces 2020, 12, 18, 20507–20513. Copyright 2020 American Chemical Society.

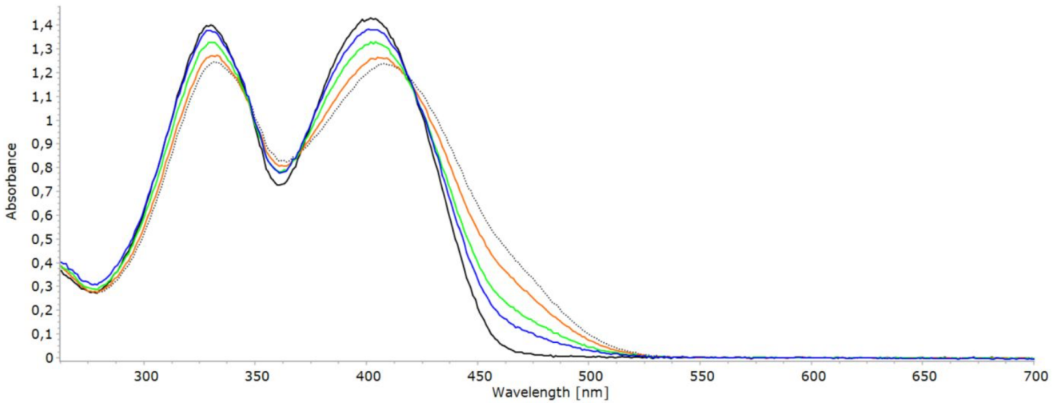

Figure B.10: UV-Vis spectra of ca. 5×10^{-5} M np-P4VB solution in MeOH-20%H_2O (black solid line), after bubbling CO_2 for a few seconds (black dotted line, atmospheric pressure), leaving the cuvette open for 5 min (red line), 15 min (green line) and 30 min (blue line). Upon release of CO_2 from solution, its concentration decreases and the equilibrium shifts towards non-protonated np-P4VB. Notice that the spectral changes here feature isobestic points, in contrast to PL spectra shown in the manuscript. It is thus indicative that the spectral changes occurring to the np-P4VB-infused paper sensor upon interaction with CO_2 have solvatochromic origin. Reprinted with permission from ACS Appl. Mater. Interfaces 2020, 12, 18, 20507–20513. Copyright 2020 American Chemical Society.

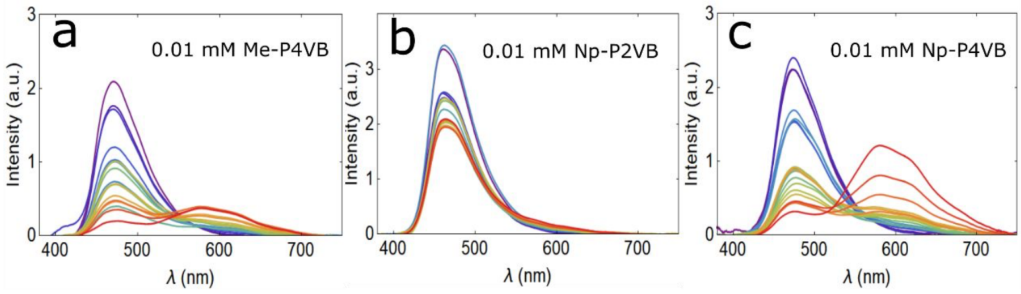

Figure B.11: PL spectra of 0.01 mM P4VB solutions in ethanol (1 mL) with an increasing number of 10 μL droplets of nominally 12 mM HCl (on going from violet to red) for (a) np-P4VB, (b) np-P2VB, and (c) me-P4VB. The acid sensing performance, as shown by the decrease of the blue peak and increase of the red one, is clearly superior for np-P4VB and it is the worst for Np-P2VB. Note that photobleaching and protonation happen concomitantly, so sensing must be performed ratiometrically as shown in the main paper. Reprinted with permission from ACS Appl. Mater. Interfaces 2020, 12, 18, 20507–20513. Copyright 2020 American Chemical Society.

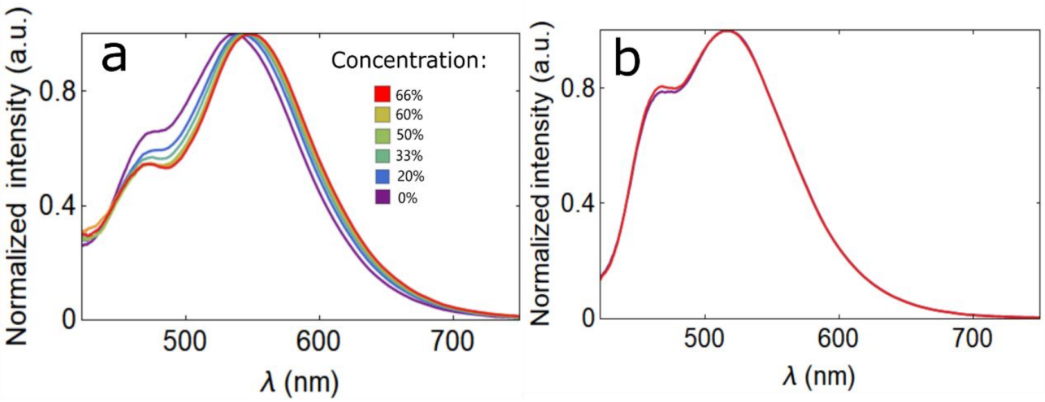

Figure B.12: PL spectra from me-P4VB-infused paper with different CO_2 concentrations from 0% to 66% for (a) me-P4VB and (b) np-P2VB, respectively. Reprinted with permission from ACS Appl. Mater. Interfaces 2020, 12, 18, 20507–20513. Copyright 2020 American Chemical Society.

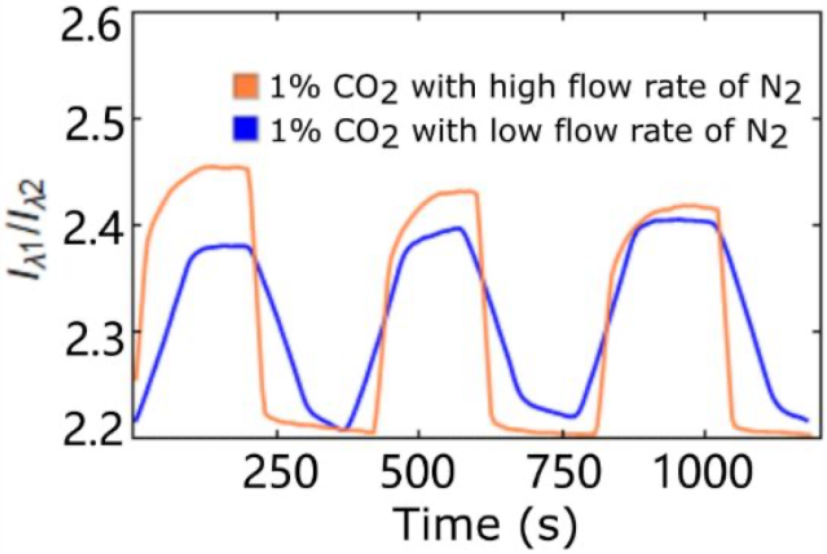

Figure B.13: Sensorgrams for of 1% CO_2. The orange line is the same as that shown in Fig. 6a of the main manuscript. Sensor regeneration with N_2 using a high flow rate (4.5 NL/h) yielded a shorter recovery time than for the lower flow rate of 2 NL/h. Reprinted with permission from ACS Appl. Mater. Interfaces 2020, 12, 18, 20507–20513. Copyright 2020 American Chemical Society.

Appendix C

Ultrasensitive picomolar detection of aqueous acids in microscale fluorescent droplets: Supplemental information

C.1 Errors and uncertainties

The errors and uncertainties from all figures represent the standard deviation of the sensing signals from four droplets with similar sizes. We chose four fluorescent octanol droplets with similar sizes in the fluorescence microscope image. The microscope image was split into the red, green, and blue channels by using Image J software. Then we chose one or a group of about 100 pixels on the center of one octanol droplet to get the pixel intensity in red, green, and blue channel. The signal S will be defined as R/(R+G+B). The error bars in the graphs represent the standard deviation of four independent measurements on different droplets. In the concentration measurements (i.e., Fig. 5 in main text) the errors represent the standard deviation from four measurements of the concentration (obtained by measuring S and concerting to Co via the calibration curves). The error in the partition coefficients were found by calculating Po/w four times from the four concentration measurements) and finding the standard deviation. We further note that the calibration curves are based on equations that were selected to fit closely to the known data points in order to extract concentrations at signal levels between the calibra-

tion values. Because the protonation goes through at least two equilibria and is likely accompanied by associate formation, the chemical system was judged too complicated to permit a physically-derived model that could completely describe the system. The error (and thus the LoD also) could be decreased by averaging over a greater number of image pixels from the droplet images. To be somewhat conservative, we tried initially taking only a single pixel near the center of the droplet, but if instead we average over 100 pixels the error decreased by approximately one order of magnitude.

C.2 Repeating the LoD calculation

The LoD for acid sensing when using a higher np-P4VB concentration (1.46 mM) can be estimated in the same way as described in the main text. Here, however, we took the lowest measured concentration at $C_w = 10^{-8}$ M in order to extrapolate the LoD. The sensitivity S was estimated from the difference in the sensing signals between 10^{-8} M salicylic acid and the blank, both after 25 minutes. The calculated LoD was 1.5 x 10^{-9} M, which is somewhat worse than that from lower np-P4VB concentration.

C.3 Droplet size distribution

The droplet size distribution was obtained by manually measuring the droplet diameters with ImageJ and calibrating the pixel counts using the image scale bars. The resulting size distribution with a lognormal fit is shown in Fig. C.2. The mean is 10.0 micrometers with a standard deviation of 3.8 micrometers.

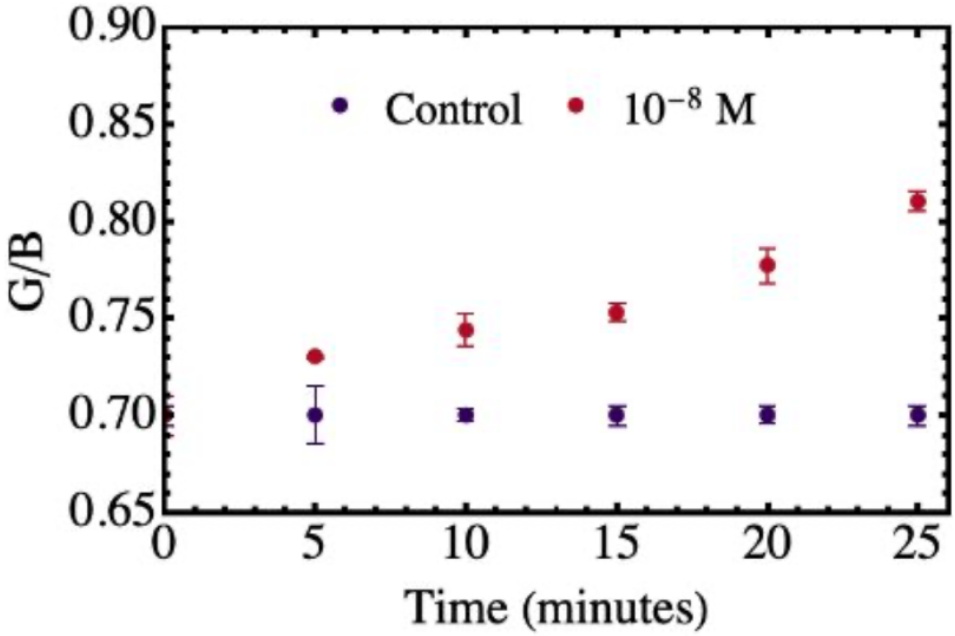

Figure C.1: The relationship between the sensing signal (G/B) and time for a sample of C_{P4VB} = 1.46 mM with C_w = 10 nM and a blank. The diameter of the droplets was about 15 μm. Reprinted with permission from ACS Sens. 2022, 7, 1, 245–252. Copyright 2021 American Chemical Society.

Table C.1: Model fitting parameters for droplets of various diameters, for two concentrations of salicylic acid in water (C_w). Reprinted with permission from ACS Sens. 2022, 7, 1, 245–252. Copyright 2021 American Chemical Society.

Diameter	Scaling B	K (m/s)	t_0 (s)	D (m^2/s)
(C_w=10^{-4}M)				
4.1 μm	0.192	6.15×10^{-7}	377	3.24×10^{-5}
5.6 μm	0.193	5.51×10^{-7}	464	1.02×10^{-5}
7.2 μm	0.193	7.91×10^{-7}	587	1.07×10^{-5}
8.4 μm	0.193	7.41×10^{-7}	763	1.04×10^{-5}
13.1 μm	0.198	9.50×10^{-7}	763	1.04×10^{-5}
(C_w=10^{-6}M)				
5.3 μm	0.090	6.97×10^{-7}	341	1.26×10^{-5}
6.3 μm	0.091	7.47×10^{-7}	422	1.59×10^{-5}
7.2 μm	0.091	6.94×10^{-7}	529	1.15×10^{-5}
9.4 μm	0.091	7.62×10^{-7}	621	1.19×10^{-5}
11.2 μm	0.093	8.31×10^{-7}	762	1.04×10^{-5}

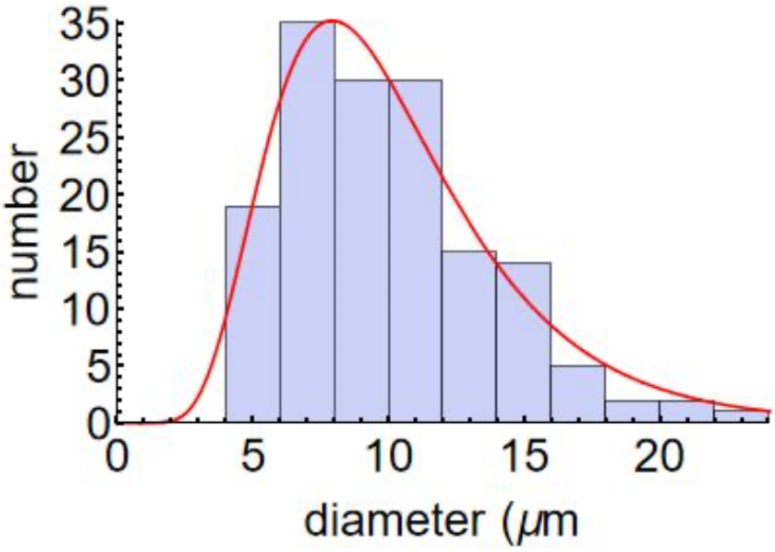

Figure C.2: The histogram of the size distribution obtained from 150 droplets. Reprinted with permission from ACS Sens. 2022, 7, 1, 245–252. Copyright 2021 American Chemical Society.